MSc Sustainable Energy Technology - SET3901 Masters Thesis
Delft, June 21, 2023

Comparative analysis of Grid forming and Grid following controls for Type-3 and Type-4 Wind Turbines

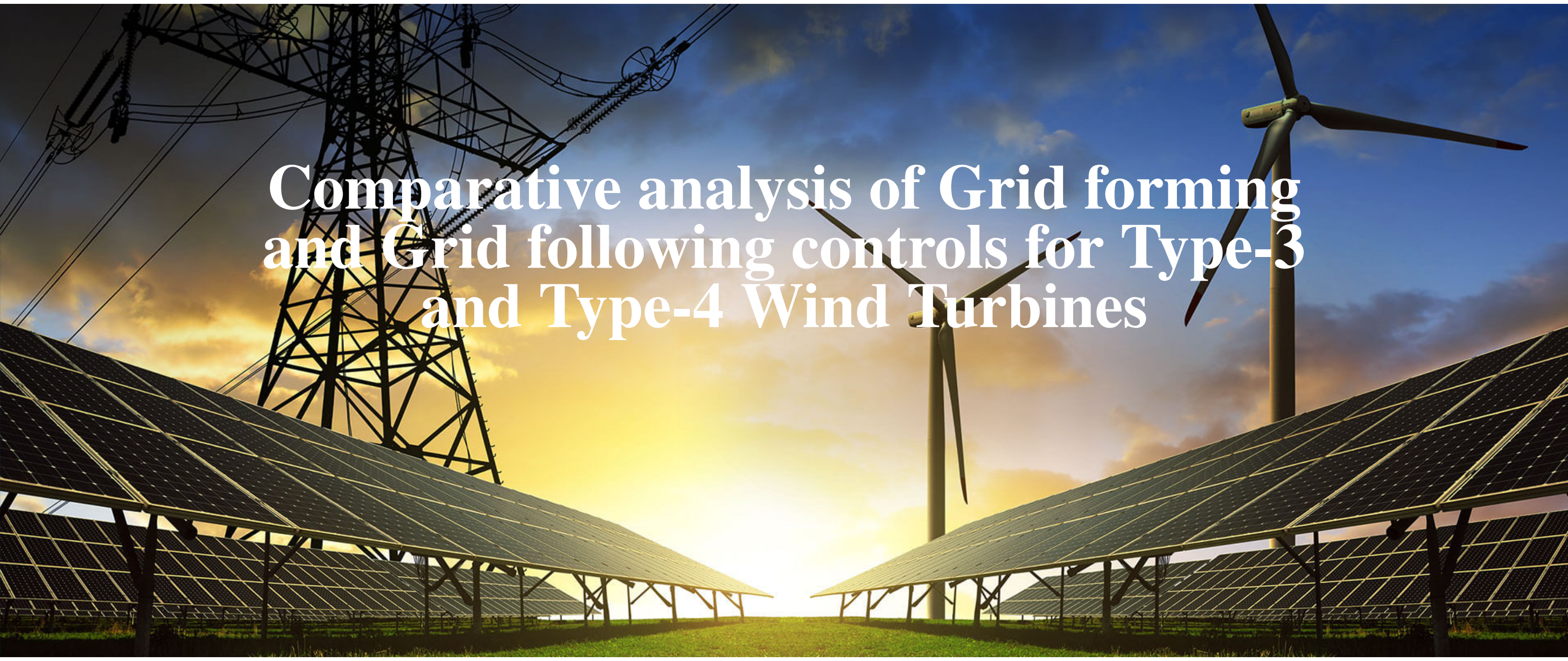

Author

UTKARSH SINGH
Student No. - 5464374

Supervisors

Assistant Professor Dr. Aleksandra Lekić
Professor Dr. Marjan Popov
Dr. Ravi Singh, Senior Researcher, R&D, DNV

Preface

This thesis is motivated by the ongoing transition from conventional power generation to renewable sources. The area of grid forming controls is one of many new technological advancements that are needed for the proper inclusion of renewable generators into the existing power systems. The thesis work is carried out with the help of Delft University of Technology (TU Delft) and DNV. The state-of-the-art infrastructure present in both organizations made it possible to achieve the intended goals of this thesis. I would like to thank my supervisors from the Delft University of Technology, Dr. ir. Aleksandra Lekić and Professor Dr. ir. Marjan Popov for introducing me to DNV, constantly helping me throughout the project and believing in me. I would especially like to express my gratitude to my company supervisor, Dr. Ravi Singh, for constantly providing me with guidance and support throughout the project, and Zameer Ahmed, Shiyi Liu from DNV for being supportive and providing necessary inputs throughout. I am grateful to Theo Bosma, head of Group R&D at DNV, for having faith in me during the entire thesis period. An immense amount of appreciation goes to Remko Koorneef, for helping me from time to time with my modeling and simulations and for helping me in the laboratory during making physical connections between the Remote PC and RTDS. And, a vote of thanks to Sumek Elibman and Chamara Devanarayan from RTDS for constantly helping me out during the coding phase. Furthermore, I would like to thank Dr. ir. Mohamad Ghaffarian Niasar for agreeing to be part of the thesis committee and evaluating my work and report. At last, I would like to thank all DNV colleagues from the Group R&D department. They were always eager to help me and accepted me as their colleague in the previous months.

Abstract

With an accelerated inclusion of renewable energy generators in the power system, the inertia support traditionally provided by conventionally powered synchronous generators is lagging, and power system stability is reducing. This grid-supporting behavior will now have to be provided by the power converters of renewable energy sources with the help of power electronics. Grid forming control refers to the idea of the converter's ability to set its frequency and voltage by means of emulating similar characteristics as that of conventional synchronous generators. Most of the protection and control studies on grid forming control for wind turbines have been done using a simple power system model containing the generator and an infinite AC bus and very less insight is available for grid forming generators in a realistic power system. This study aimed to apply the grid forming control strategy on DFIG (Type-3) and full converter wind turbines (Type-4). For this, the MIGRATE benchmark models in RSCAD/RTDS were used for the comparison of the key power indicators for both grid forming and grid following controlled modes. This was followed by the development and validation of the grid forming controller as a blackbox model (RTDLL and RTSS file) using IntervalZero and RTDS software in the loop setup (SIL). The communication between the black box file and the real-time simulator was built using the UDP protocol.

Contents

List of Figures

List of Tables

List of Abbreviations

DFIG	Doubly Fed Induction Generator
WT	Wind Turbine
FC	Full Converver
FCWT	Full converter wind turbine
VSC	Voltage Source Converter
VSM	Full Virtual Synchronous Machine
GFM	Grid Forming
GFL	Grid Following
RSC	Rotor Side Converter
GSC	Grid Side Converter
MSC	Machine Side Converter
UDP	User Datagram Protocol
PLL	Phase Locked Loop
VC	Vector Control
SCR	Short Circuit Ratio
AC	Alternate Current
DC	Direct Current
HVDC	High Voltage Direct Current
PMSG	Permanent Magnet Synchronous Generator
MPPT	Maximum Power Point Tracking
PWM	Pulse Width Modulation
SISO	Single Input Single Output
IP	Intellectual Property
PCC	Point of common coupling
SIL	Software in the loop
SG	synchronous generator

List of Symbols

s	Slip of the doubly fed machine / Laplace operator
X_L	Coupling reactance
E	Voltage magnitude
V_g	Stator internal voltage
V_s	Generator terminal voltage
ω	Angular velocity
ω_r	Rotor angular velocity
ω_0	Reference angular velocity
ω_{opt}	Optimum turbine angular velocity
P	Active power
P_g	Airgap power
P_{Cu}	Rotor copper loss
P_r	Power fed to converter of DFIG
P_m	Mechanical power
Q	Reactive power
δ	Phase angle difference
T_e	Electrical torque
t_m	Mechanical torque
J	Inertia constant
ψ_r	Rotor flux
L_m, L_r, L_s, L_0	machine per phase inductances
L_{ms}	Magnetizing stator inductance
ω_{slip}	Slip frquency
σ	Leakage factor
K_{opt}	Optimum power coefficient
T_j	Virtual inertial time constant
R_v	Virtual resistance
U_t	Generator terminal voltage
U_r	Rotor Excitation voltage
D	Damping coefficient
P_D	Damping power
β	Angle between Stator Internal voltage and Rotor excitation voltage
ϕ_r	Angle between Stator internal voltage and Rotor current
P_{ref}	Reference active power
Q_{ref}	Reference reactive power
K_p	Proportional constant of controller
K_i	Integral constant of controller
v_{dr}	Rotor direct axis voltage
v_{qr}	Rotor quadrature axis voltage
i_{dr}	Rotor direct axis current
i_{qr}	Rotor quadrature axis current
i_{ms}	magnetizing stator current
ψ_r	Rotor Flux
X_{ls}	Stator leakage reactance
X_{lr}	Rotor leakage reactance
R_r	Rotor resistance
R_s	Stator resistance
T	Torque
p	No. of pole pairs
λ_s	Stator flux
λ_{dr}	Rotor direct axis flux
λ_{qr}	Rotor quadrature axis flux

1 Introduction

This section presents the fundamental background and introduces the problem statement and research questions that will be dealt with in the later sections. First, the concept of grid forming and grid following controls will be introduced at the fundamental level and keeping in mind their functionality with Wind Turbines (WTs). Then the DFIG machine and its vector control method (grid following) is explained in detail followed by an explanation of the virtual synchronous machine (VSM) grid forming control strategy applied on a Doubly Fed Induction Generator (DFIG) driven wind turbine. Finally, the problem statement and the research questions are pointed out. For the rest of the document, DFIG based WT will be referred to as Type-3 WT and PMSG based WT will be referred to as Type-4 WT.

1.1 Introduction of Grid Forming and Grid Following Control Strategies

With the rapid development of wind power worldwide, the unique characteristics of wind power's static and dynamic responses have issued new major challenges to the adequacy and stability of the modern power system. One of the prominent concerns regarding the increasing penetration of wind power is its impact on power system frequency stability due to the lack of positive response from the installed WTs to frequency disturbances, i.e., large load fluctuations or generating unit losses, occurring in the power grid (S. Wang, Hu, Yuan, & Sun, 2015). Therefore, the dynamic frequency support capability of wind power is much needed in the near future to ensure that frequency stability is not compromised.

It is known that almost all of the installed WTs currently are adopting the typical vector control (VC) method based on the phase-locked-loop (PLL) synchronizing technique. The PLL works fine with a strong grid where the grid is dictating voltage angle and magnitudes to the controls of the WT's converter. Such an arrangement where controls of the converter follow the voltage angle and voltage magnitude inputs from a strong grid and themselves behave as a current source is known as a **grid-following (GFL) control strategy**.

On the other hand, when large-scale WTs are located in the weak grid, power fluctuations may lead to an increase in magnitude and frequency variations in the grid voltage, which may adversely affect the performance of PLL and the control system thereof. As the short circuit ratio (SCR) of the connected AC system is reduced, the resonances and nonlinearity due to the PLL become more prominent and potentially make the Voltage Source Converter (VSC) more difficult to control. A modern power grid with a high penetration of renewable generators resembles a weak grid with low SCR value intermittently due to the lower reliability of renewable sources and hence, the relatively novel concept of **grid forming control** evolved.

A **grid forming (GFM) converter** fundamentally behaves as a voltage source behind a coupling reactance X_L, which controls both the voltage magnitude E and angular frequency ω, as shown in Figure 1 (Kikusato et al., 2023). The coupling reactance X_L plays a critical role in controller design. By properly sizing the coupling reactance X_L , the active power P and reactive power Q are decoupled (Du et al., 2020). As shown in equations (1b) and (1c) below, P is nearly linear with the phase angle difference δ_p, and Q is almost linear with the internal voltage magnitude E. This decoupling reduces the controller design complexity and is known as the power-frequency ($P-f$) droop relationship and the reactive power-voltage magnitude ($Q-V$) droop relationship respectively.

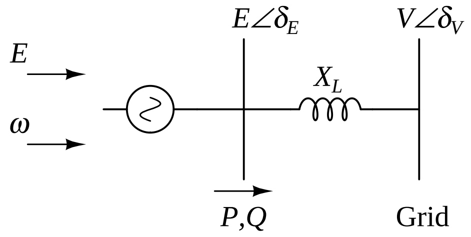

Figure 1: Basic concept of Grid forming, (Du et al., 2020)

$$\delta_p = \delta_E - \delta_V \tag{1a}$$

$$P = \frac{EV}{X_L}\sin\delta_P = \frac{EV}{X_L}\delta_p \tag{1b}$$

$$Q = \frac{E^2 - EV\cos\delta_p}{X_L} = \frac{E\,(E-V)}{X_L} \tag{1c}$$

The grid forming control strategy used for both Type-3 and Type-4 WTs also satisfies the above discussed fundamentals and is known as the virtual synchronous machine (VSM) strategy. The VSM control strategy will be extensively discussed in section 1.3. Now we discuss the fundamentals of a doubly fed induction machine and vector control method (grid following control) of which is commonly deployed in Type-3 WT models.

1.2 Doubly Fed Induction Machines and Vector Control

1.2.1 Fundamentals of Doubly Fed Induction Machines

The concept of doubly fed machines originates from the wound rotor induction machine in which, unlike a traditional induction machine, the rotor also contains three-phase windings along with slip rings and an adjustable resistance (Figure 2).

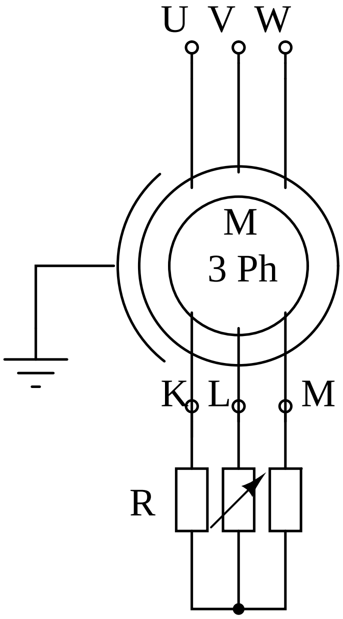

Figure 2: Wound Rotor machine, (“Wound rotor motor”, 2022)

Such a construction makes limited speed control possible which makes it attractive for WT control applications. Increasing the resistance brings down the phase lag and the condition for maximum torque is met.

Doubly fed means that you can put in/take out power through both the stator and rotor. An AC voltage at slip frequency is applied to the rotor. Hence, a doubly fed construction can work as a motor or generator, and can also work super-synchronous/sub-synchronous. Typical induction generator characteristics can be seen in Figure 3 below.

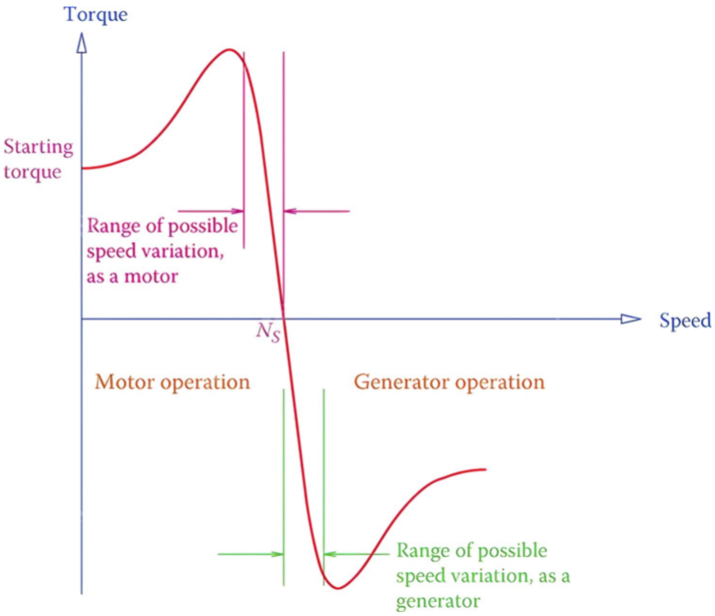

Figure 3: Induction machine characteristics (“Three-phase induction motor torque-speed characteristics”, 2018))

The aim is to match WT characteristics with generator characteristics but because of a low rotor resistance, the induction generator operates at a near-fixed speed. For a generator, a low rotor resistance is preferred, but the WT requires a wider speed range. This amalgamation is achieved with the help of doubly fed machine construction and back to back converter-inverter technology (AC-DC-AC) which carries out $f-sf-f$ conversion, where sf is the slip frequency. Such type of construction of a WT is referred to as Type-3 WT.

This type of WT provides variable speed generator range of up to 30 % above and below the nominal speed with a minimum slip loss, individual control for real and reactive power, and losses limited to one-third in comparison with the Type-4 WT, improved fault ride-through performance, maximized aerodynamic power extraction, and reduction of mechanical stress (Wu & Sun, 2018).

1.2.2 Equivalent Circuit of DFIG

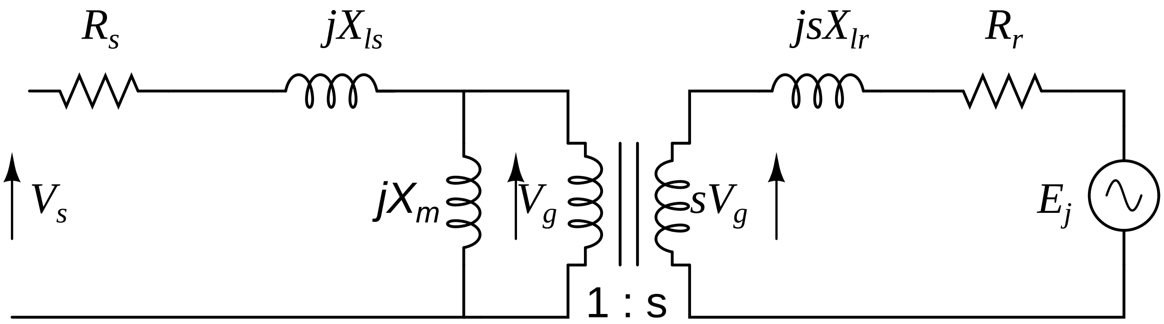

Figure 4: DFIG Equivalent circuit

Figure 4 represents the equivalent circuit of a DFIG referred to stator side. In the figure 4, V_g is the stator's internal voltage, V_s is terminal voltage and E_j is rotor excitation voltage. X_{ls} and X_{lr} stand for the stator's and rotor's leakage reactances, respectively. R_r and R_s are stator's and rotor's resistances, respectively. For the phasors shown in Figure 5, β is the angle arbitrarily chosen between vectors V_g and E_j, and ϕ_r is the angle between vectors V_g and I_r. Slip is denoted with s here. In the above circuit, the rotor side parameters are written as referred to as stator turns.

By Kirchoff's Voltage Law:

$$sV_g - I_r(R_r + jsX_{lr}) - E_j = 0, \tag{2a}$$

$$sV_g - E_j = I_r(R_r + jsX_{lr}). \tag{2b}$$

Phasor diagram with injected EMF:

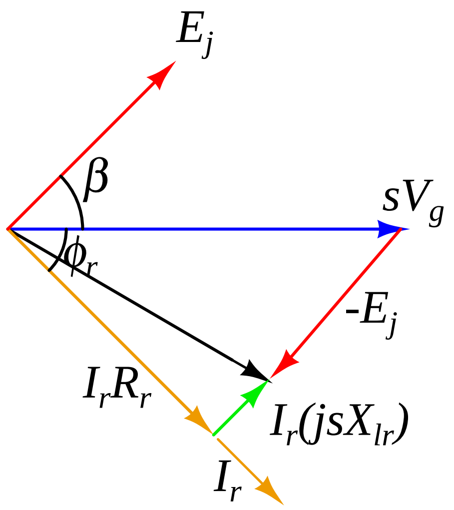

Figure 5: DFIG Phasor diagram with injected EMF

resolving along the I_r axis we get:

$$sV_g \cos\phi_r = I_rR_r + E_j \cos(\phi_r + \beta). \tag{3}$$

multiplying with I_r on both sides we get an equation:

$$sV_gI_r \cos\phi_r = I_r^2R_r + E_jI_r \cos(\phi_r + \beta). \tag{4}$$

for three-phase, airgap power (P_g), rotor copper loss (P_{Cu}) and power fed to converter (P_r) are:

$$P_g = 3V_gI_r \cos\phi_r, \tag{5a}$$

$$P_{Cu} = 3I_r^2R_r, \tag{5b}$$

$$P_r = 3I_rE_j \cos(\phi_r + \beta). \tag{5c}$$

By energy conservation, the airgap power should be equal to the summation of rotor copper loss, power fed to the converter, and mechanical power (P_m). Hence P_m can be defined as :

$$P_m = (1 - s)P_g. \tag{6}$$

Two modes of DIFG's operation:

Table 1: DFIG generation modes

SUB-SYNCHRONOUS GENERATING:-	SUPER-SYNCHRONOUS GENERATING:-
$0 < s < 1$, s is $+v_e$	$-1 < s < 0$, s is $-v_e$
P_g, P_e and P_r are negative	P_g, P_e are negative, P_r is positive
$P_m = (1-s)P_g$ is negative	$P_m = (1-s)P_g$ is negative
P_m is less than P_g	P_m is less than P_g

Schematic of a DFIG generating in a super-synchronous state can be seen in Figure 6 below.

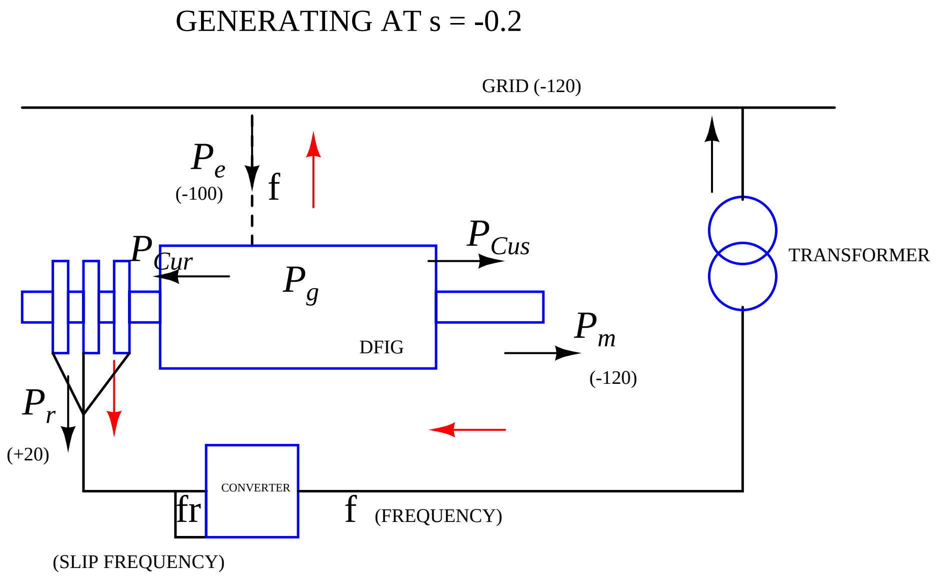

Figure 6: DFIG operation in super-synchronous state, (Wu & Sun, 2018).

1.2.3 Grid Following Control

The induction machine is controlled in a synchronously rotating dq-axis frame, with the d-axis oriented along the stator-flux vector position. In this way, a decoupled control between the electrical torque and the rotor excitation current is obtained (Pena et al., 1996).

Under stator-flux orientation, the relationship between the torque and the dq-axis voltages, currents, and fluxes (all scaled to be numerically equal to the AC per-phase values) may be written as equations (7).

$$\lambda_s = \lambda_{ds} = L_o i_{ms} = L_s i_{ds} + L_o i_{dr}, \tag{7a}$$

$$\lambda_{dr} = \frac{L_o^2}{L_s} i_{ms} + \sigma * L_r i_{dr}, \tag{7b}$$

$$\lambda_{qr} = \sigma L_r i_{qr}, \tag{7c}$$

$$i_{qs} = \frac{-L_o}{L_s} i_{qr}, \tag{7d}$$

$$v_{dr} = R_r i_{dr} + \sigma L_r \frac{di_{dr}}{dt} - \omega_{slip} \sigma L_r i_{qr}, \tag{7e}$$

$$v_{qr} = R_r i_{qr} + \sigma L_r \frac{di_{qr}}{dt} + \omega_{slip}(L_{ms} i_{ms} + \sigma L_r i_{dr}), \tag{7f}$$

$$T_e = -3\frac{p}{2} L_m i_{ms} i_{qr}, \tag{7g}$$

$$\omega_{slip} = \omega_e - \omega_r, \tag{7h}$$

$$\sigma = 1 - \frac{L_o^2}{L_s L_r}, \tag{7i}$$

$$L_m = \frac{L_o^2}{L_s}. \tag{7j}$$

From the above equations (7), the torque is proportional to i_{qr}. and can be regulated using v_{qr}. The rotor excitation current i_{dr} is controlled using v_{dr}. The reference q-axis rotor current can be obtained either from an outer speed-control loop or from a reference torque imposed on the machine. These two options may be termed a speed-control mode or torque-control mode for the generator (Pena et al., 1996). The torque control mode is implemented in the MIGRATE model where the reference torque is given by the formula:

$$T_e^* = K_{opt} \omega_r^2, \tag{8}$$

and the reference quadrature current as:

$$i_{qr}^{*} = \frac{-2T_e^{*}}{3pL_m i_{ms}}. \tag{9}$$

From the rotor-voltage equation we have:

$$v'_{dr} = R_r i_{dr} + \sigma L_r \frac{di_{dr}}{dt}, \tag{10a}$$

$$v'_{qr} = R_r i_{qr} + \sigma L_r \frac{di_{qr}}{dt}. \tag{10b}$$

The i_{dr} and i_{qr} errors are processed by the PI controller to give references v_{dr}, and v_{qr}, respectively. From equations (10a) and (10b), the plant for the current control loops is given by (s is Laplace operator):

$$F(s) = \frac{i_d(s)}{v'_d(s)} = \frac{i_q(s)}{v'_q(s)} = \frac{1}{Ls+R}. \tag{11}$$

The above plant can be controlled using PI controllers with compensation terms added as in equations (10a) and (10b) (Erlich et al., 2007).

1.3 Virtual Synchronous Machine Control

In a Synchronous Generator (SG), the inner potential vector V_g, is tightly connected to the rotor position. Furthermore, the rotor dynamics are mainly determined by the interactions between mechanical and electromagnetic torques, which can be described by the well-known swing equation in generator mode:

$$T_m - T_e = \frac{J}{p}\frac{d\omega}{dt}, \tag{12}$$

where p represents the pole pairs, ω is the electrical angular velocity, and also the angular frequency of the inner potential, T_m and T_e are the mechanical input and electromagnetic output torques, respectively (S. Wang, Hu, & Yuan, 2015). As a result, once SG is out of sync with the grid during the transient, e.g., when large load variations or generating unit losses occur in the grid, the resulting unbalanced torque applied on SG will automatically regulate the inner frequency ω until synchronization is achieved again. The kinetic energy released due to the speed regulation will provide temporary power support during synchronization.

With regard to the WT-driven DFIG, Figure 7 shows the vector diagram in the stator stationary reference frame under super-synchronous conditions. The generator convention is adopted in the stator, while the motor convention is in the rotor. In Figure 7, V_g, which is defined as $V_g = j(Lm/Lr)\psi_r$ (in per unit), represents the inner potential of DFIG's stator and the magnitude of V_g depends on that of the rotor flux ψ_r (S. Wang, Hu, & Yuan, 2015). The d-axis of the defined synchronous rotating reference frame is chosen to be aligned with the stator terminal voltage vector V_s, and δ_{dfig} is defined as power angle, which is the electrical angle separating the two vectors V_g and V_s. Since the inner potential V_g is always orthogonal to ψ_r, the angular frequency of V_g (ω) equals that of ψ_r and this angular velocity can be manipulated by the adjustment of the rotor excitation voltage, E_j, determined by the rotor-side converter control. Hence the rotor side converter control directly affects the angular frequency of Inner potential V_g.

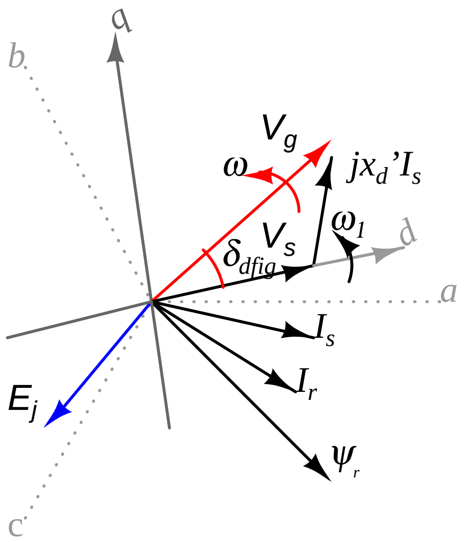

Figure 7: Vector diagram of DFIG in the stator stationary reference frame under super-synchronous condition (S. Wang, Hu, & Yuan, 2015).

As a result, the rotational angular velocity of the rotor excitation voltage E_j can be regulated automatically when unbalanced power applied on DFIG occurs, which can meanwhile achieve the goal of regulating the inner frequency ω of V_g as mentioned above. Therefore, ω can be directly produced by means of a virtual swing equation as:

$$P_e^{ref} - P_e^{meas} = T_j \frac{d\omega}{dt}, \tag{13}$$

where P_e^{ref} is the reference value of active power produced by the outer speed controller and P_e^{meas} represent the total output active power from both DFIG's stator and rotor. In addition, T_j represents the inherent inertia constant, and the role is similar to the inertia constant of SG, represented by H in general. According to the aforementioned idea, the slip frequency ω_{slip} can be obtained by the difference between ω and ω_r, and the phase angle of the rotor excitation voltage, represented by θ_r, is further generated by the integral of the slip frequency as:

$$\theta_r = \int (\omega - \omega_r)dt = \int \omega_{slip} dt, \tag{14}$$

where ω_r is the electrical angular velocity of DFIG's rotor. Hence the phase angle is produced without the use of a PLL, which essentially makes it a grid forming control strategy. Now the problem statement of the thesis can be defined along with research questions that will be addressed.

1.4 Problem Definition

This thesis will directly contribute towards the greater inclusion of renewable generators like wind turbines in the power grid. The main problem with the increasing inclusion of renewable generators in the grid is grid stability due to the lack of grid-supporting generators as the renewable generators do not have inherent inertia and most of the current inverters are grid following. Most of the literature today on the grid following and grid forming control strategies involve simple power system models with one generating source connected to an infinite AC source, which does not represent a realistic power system. There is a lack of standard test systems where grid following and grid forming strategies can be tested and compared with simulated renewable energy sources. Also, there is a lack of knowledge on the development of a controller model into a black box which can be tested with a power system model through co-simulation in real-time. The development of such a test bed in order to perform the comparative analysis will enhance the approval of novel strategies. This thesis presents the development of an accurate wind turbine model for the grid forming/grid following converter application, and an exhaustive comparative analysis between grid forming and grid following strategies. This is followed by the development and validation of the Grid forming controller as a black-box model working in co-simulation with the power system model on RTDS in real-time.

1.5 Research questions addressed

The following research questions are addressed in this thesis:

1. How to design the realistic test-bed for testing novel control strategies for wind turbines?
2. What is the correct application process of grid forming controls for Type-3 and Type-4 wind turbines?
3. Under which grid conditions do the grid forming controls perform better than the grid following controls?
4. What is the process of developing a controller model into a black box file which protects intellectual property (IP) and is capable of running in real-time?

1.6 Thesis Outline

Chapter 1: Introduction - Introduces the fundamental concepts of the grid following and grid forming control strategies along with induction machines. Introduces the problem statement and aim of the thesis work along with the research questions addressed.

Chapter 2: MIGRATE benchmark model - Describes the classical control strategies present in the MIGRATE Benchmark model of both Type-3 and Type-4 WTs.

Chapter 3: Stability Analysis of VSM Control Strategy - Presents basic implementation of VSM control strategy, followed by the derivation of the transfer function for the active power loop. Stability margins were observed from the bode plots using MATLAB.

Chapter 4: Grid Forming Control - Detailed application of the VSM strategy on the original DFIG WT model and Type-4 WT model is presented.

Chapter 5: Tests and Results Discussion - Description of the tests performed and results obtained on both the models and comparative analysis drawn.

Chapter 6: Grid Forming Controller as Black Box Model - Detailed process of developing the Grid forming controller as a black box and co-simulating it in real-time with the power system model is explained. A test will be performed in order to prove validation.

2 MIGRATE Benchmark model

The MIGRATE project ("MIGRATE project Work Package 4", 2020) benchmark model consists of a point-to-point terminal HVDC link connected to a grid with loads, WTs, photovoltaic solar farm, and conventional generation. An infinite grid with the possibility of modifying its strength has also been included (Chavez et al., 2021). A typical network is chosen in a way to look like a benchmark model of the IEEE upgraded with renewable sources (i.e. Type-3 WT, Type-4 WT, Solar), and an HVDC link. The schematic of the model can be seen below in Figure 8.

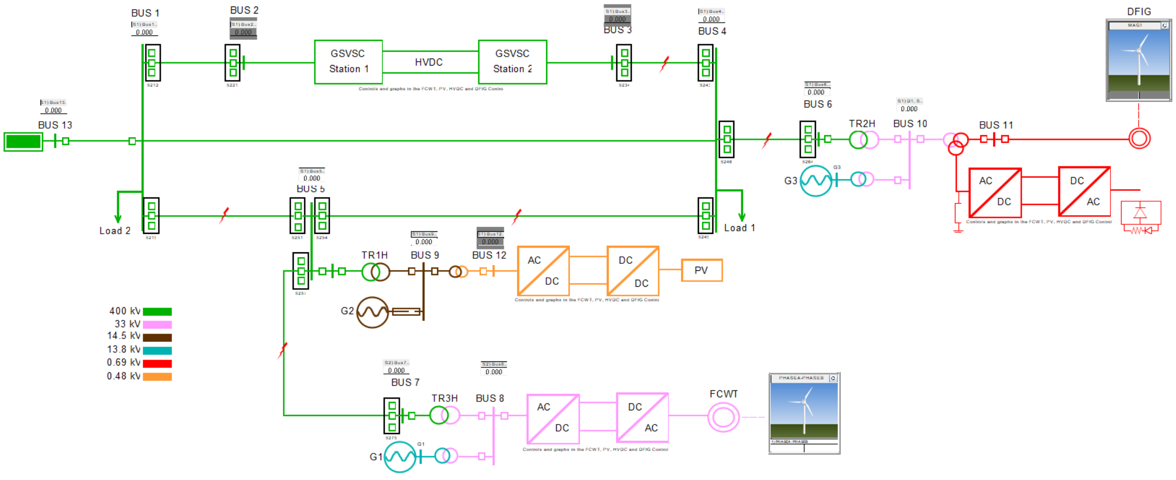

Figure 8: Migrate Benchmark model, ("MIGRATE project Work Package 4", 2020).

2.1 Type-3 WT model

The implemented RSCAD Type-3 WT model in the MIGRATE benchmark is located in the second subsystem of the benchmark. There are five hierarchy boxes containing the applied control in this model. The black box depicted in Figure 9 contains the grid code controls. The blue and red boxes are related to the grid and rotor VSC controls, respectively. The WT with its controls can be found in the green box. Finally, The Type-3 WT generator protection (chopper and rotor crowbar) controls and converter blocking control are located in the last box (purple box). In the application of high power, Scherbius drive (Figure 10) is a standard drive option used in the Type-3 WT. This drive is an AC–DC–AC converter in the rotor circuit where the rotor side converter (RSC) is the AC to DC converter and the grid side converter (GSC) is the DC to AC converter. In this drive, the rotor windings are supplied through slip rings from two inverters (grid VSC and rotor VSC) connected back–to–back. Three single-phase interface transformers are used to connect the Scherbius drive to the rest of MIGRATE benchmark.

In the case of the Type-3 WT system only 2 masses are modeled, the turbine itself and the DFIG. Through the configuration menu for the multi-mass, it is possible to select the high pressure and turbine mass inertia constants such that adding the two must match the value of the total inertia H requested in the mechanical constant (Popov et al., 2020) . Shaft spring constant, self, and mutual damping are other characteristics that can be specified. At the turbine data menu in Table 2, values such as rated turbine power (MW), rated generator power (MVA), and rated wind speed (during m/s) that gives 1 pu power at 1 per unit rotational speed are given. Those parameters are considered constant during the simulation time.

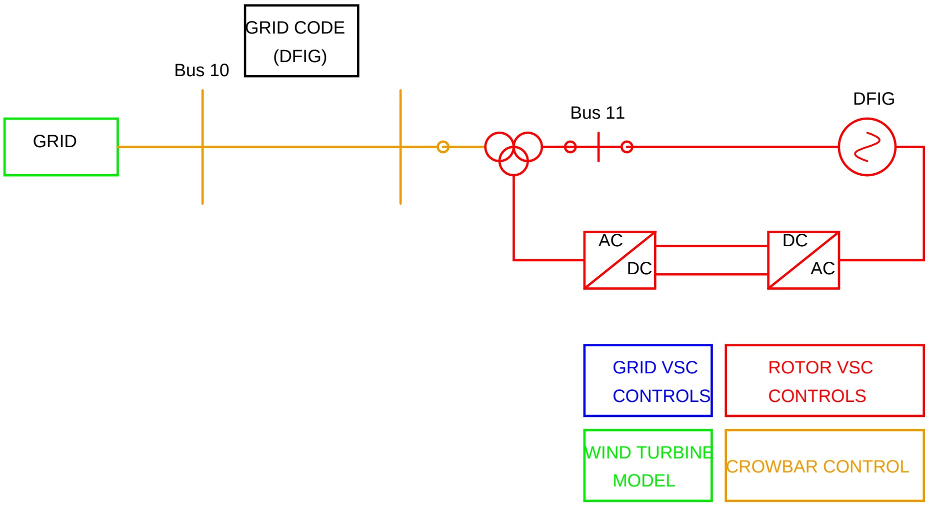

Figure 9: Type3 WT Model, ("MIGRATE project Work Package 4", 2020).

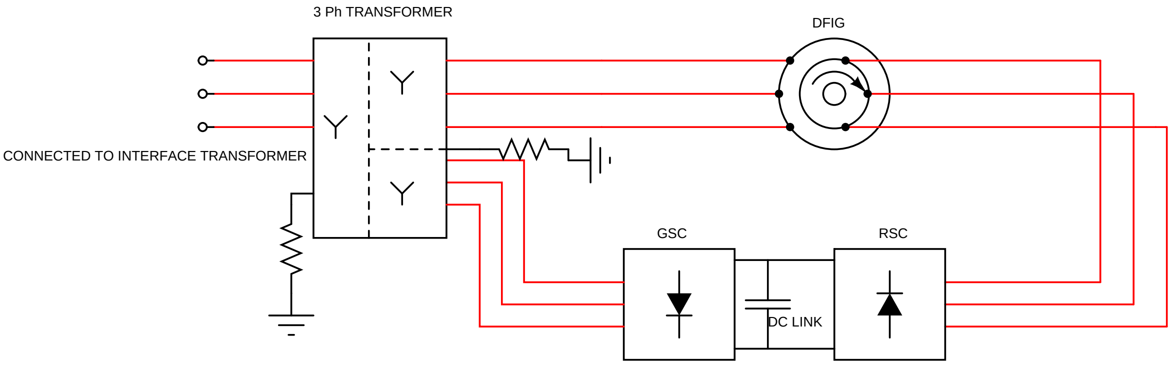

Figure 10: Sherbius Drive.

Table 2: Turbine Data

DESCRIPTION	VALUE
Rated Generator Power (GR)	2.2 MVA
Rated Turbine Power (TR)	2.0 MW
PU Gen Speed at Rated Turbine Speed (WR)	1.2 p.u
Rated wind speed (WSR)	12 m/s
Cut-in wind speed (WSCI)	6 m/s

The model of the WT is based on the steady-state behavior, where the fundamental relationship for the power delivered by the rotor becomes equal to the upstream power in the wind multiplied by the fraction of wind's power that is extracted by the blades (power coefficient of the rotor, C_p):

$$P_b = \frac{1}{2}\rho A v^3 C_p, \tag{15}$$

where ρ is the air density in $\mathrm{kg/m^3}$, A is the swept area ($\mathrm{m^2}$) by the rotor, and v is the wind velocity ($\mathrm{m/s}$). The coefficient of the rotor is generally less than 0.5 and can be calculated using different formulas. In this work, the coefficient of the rotor is defined by:

$$C_p = ((0.47 - 0.0167\beta)\sin(1.5707\frac{\lambda - 3y}{7.5 - 0.15\beta}) - (\lambda - 3y)0.00814\beta) + \frac{0.01}{1+\lambda}, \tag{16a}$$

$$y = 1 - 1e^{-\lambda/3}, \tag{16b}$$

where λ is the tip speed ratio and β is the pitch angle (in degrees).

2.1.1 Type-3 WT converter controls

The current inner regulators are considered the fundamental parts of the control strategies applied in both GSC and RSC. The inner controllers receive their reference signals provided by the outer controllers. Each GSC and RSC contains four inner controllers. Two controllers regulate the positive sequence current components and the other two control the negative sequence ones. The positive sequence outer controllers in GSC are responsible to maintain constant the DC-link voltage and provide the required reactive power at the Type-3 WT generator point of common coupling (PCC) based on the applied grid code. Simultaneously, the RSC positive sequence outer controllers regulate the active and reactive power based on the optimal WT power extraction and the applied grid code, respectively. Similarly to the positive sequence controllers, four regulators are considered to control the negative sequence current components. To provide the reference control signals for negative sequence regulators, double frequency minimization is considered the main target. Figure 11 shows a general overview of the applied converter control schemes.

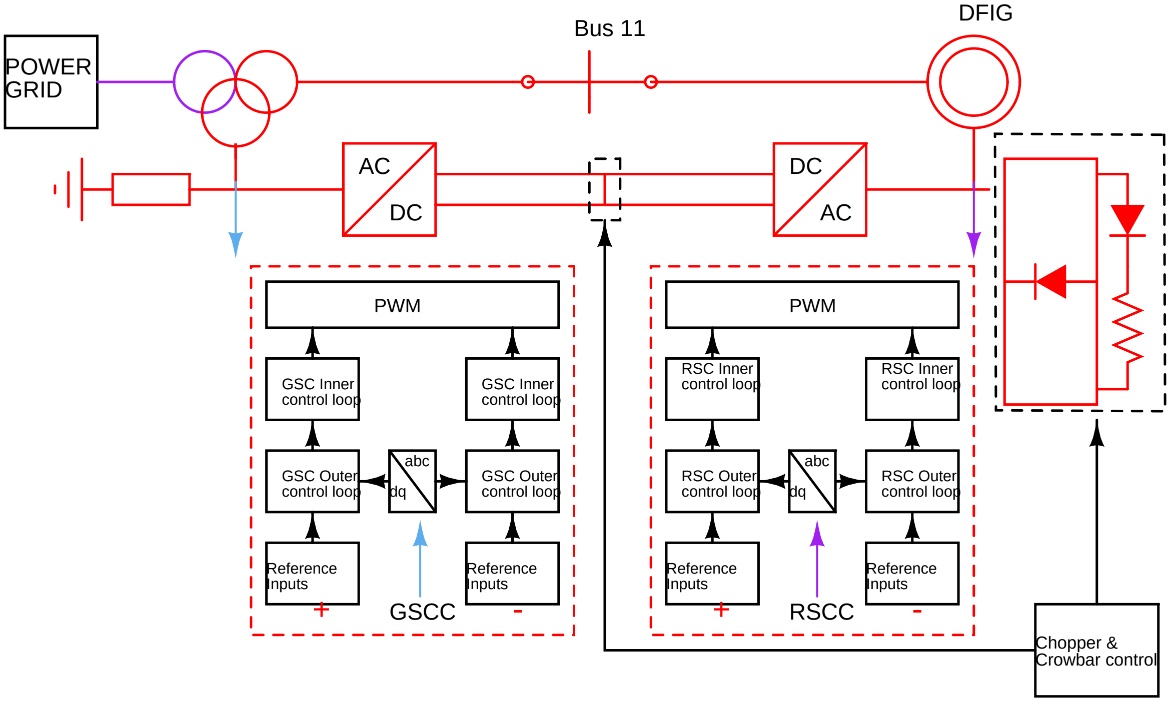

Figure 11: General overview of the applied Type-3 WT converter control schemes, ("MIGRATE project Work Package 4", 2020).

2.1.2 RSC control

The focus is paid to the RSC control strategy since the application of grid forming controls was done on the RSC, while other controls were left unchanged. According to Sub-section 1.2.3, the simple PI controllers can be used in the positive and negative inner controllers as shown in the following Figure 12. The derivation of compensation terms is done based on characteristic equations of the generator. Derivation of compensation terms for a controller is discussed in a later sub-section 4.3. The main objective of the RSC control is to extract the optimal power from the WT. In addition to this, it can inject reactive power (according to the defined grid

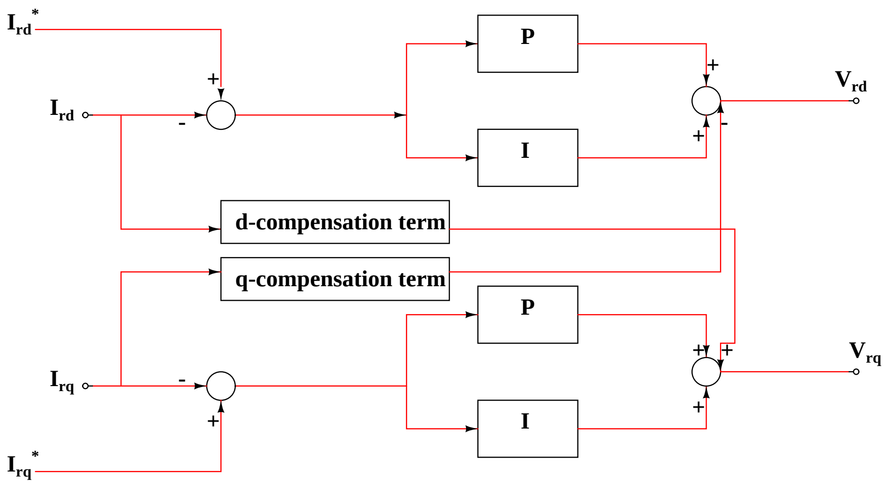

Figure 12: RSC inner current controller scheme.

code) to the grid PCC to boost the voltage under fault conditions. This is achieved by providing reference currents I_{rd}^* and I_{rq}^* which are outputs from outer MPPT control and grid code requirement respectively. We will see later that these reference currents will be generated from an intermediate voltage controller in case of GFM control mode. To minimize the double frequency oscillations under unbalanced conditions, negative sequence outer controllers provide the required set points for the corresponding inner regulators. Figure 13 shows outer control loops and inner control loops, and the required measurements for RSC. The figure shows that the references for inner controllers are produced by the outer controllers for the positive and negative control schemes. The original controls of RSC defined here are altered to make the converter grid forming, the details of changes made are discussed in later section 4.

2.2 Type-4 WT model

For the Type-4 WT a PMSG of 2.0 MW rated power has been modeled. To integrate this WT in the grid an appropriate control system is needed for both the GSC and RSC. The starting point for modeling the real behavior of the WT is the library model found in the RSCAD library. The topology of the converter of the library model is a three-level diode-clamped converter (Figure 14). This model provides a 4 kV-2.0 MVA generator model, connected to a 33 kV power system. The rated power of the full converter model has been scaled to reach the different penetration levels defined for the protection studies.
The physical part of the turbine is similar to that of the Type-3 WT generator. The permanent magnet synchronous generator (PMSG) block in the RSCAD library is used in the electrical part of the turbine. The dynamic model of the surface-mounted permanent-magnet generator in the magnet flux reference system is (Shariatpanah et al., 2013):

$$u_{Sd} = -R_S i_{Sd} - L_S \frac{di_{Sd}}{dt} + L_S \omega i_{Sq}, \tag{17a}$$

$$u_{Sq} = -R_S i_{Sq} - L_S \frac{di_{Sq}}{dt} - L_S \omega i_{Sd} + \omega \psi, \tag{17b}$$

where L_S and R_S are the generator inductance and resistance, respectively, ω is the generator speed, and ψ is the magnet flux (Y. Wang et al., 2015). The above equations (17b), (17a) show how to control current components by means of the applied voltage. From Equations (17a) and (17b), the transfer function of the stator windings is:

$$F(s) = \frac{I_{Sd}(s)}{U'_{Sd}(s)} = \frac{I_{Sq}(s)}{U'_{Sq}(s)} = \frac{1}{R_S + L_s s}, \tag{18}$$

where U'_{Sd} and U'_{Sq} are the voltage components in the dq-axes that control the corresponding current components, and s is the Laplace operator (Chinchilla et al., 2006). Hence this plant can be controlled using PI controllers and compensation terms can be added using equations (17a) and (17b).

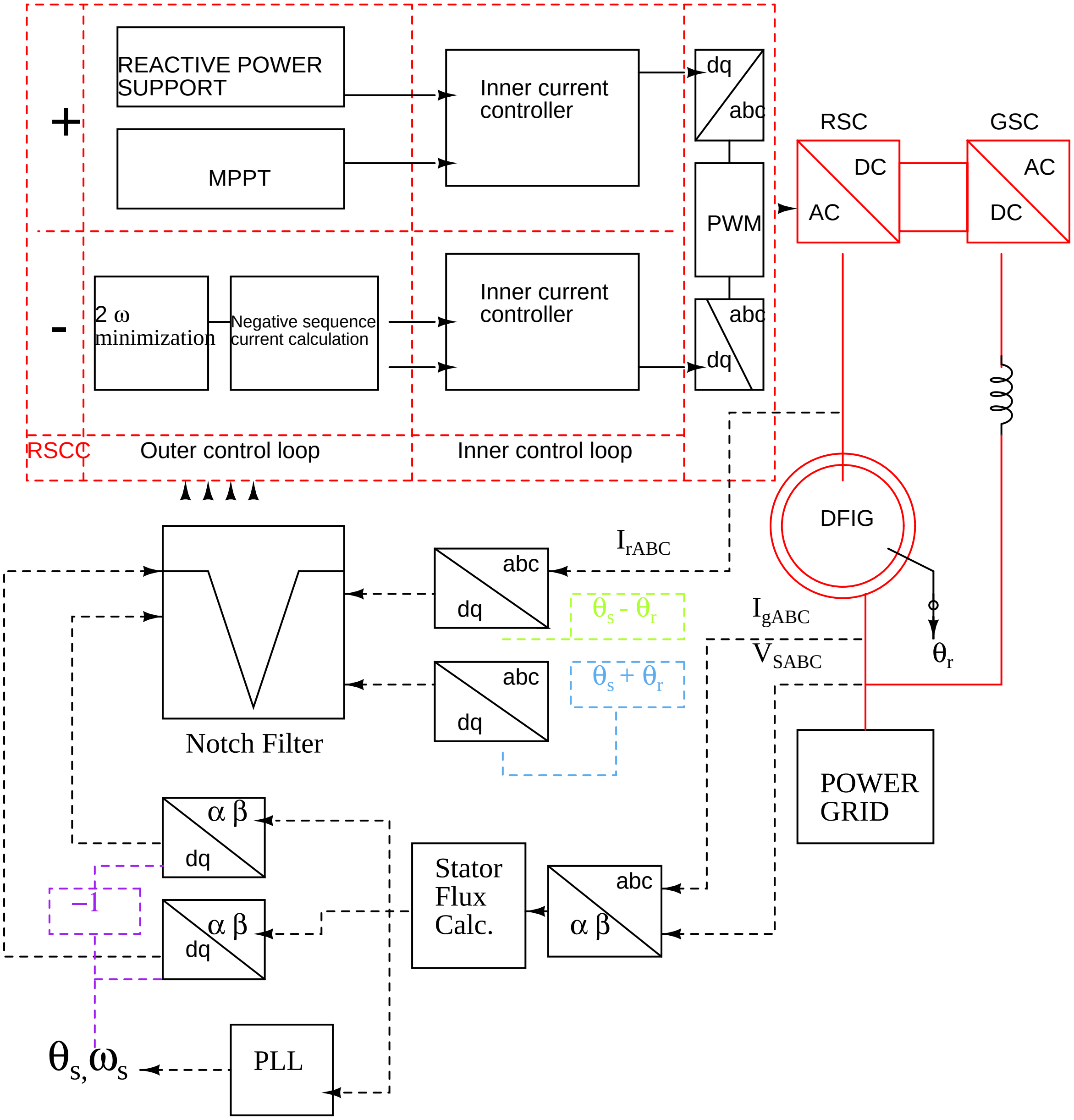

Figure 13: RSC control scheme.

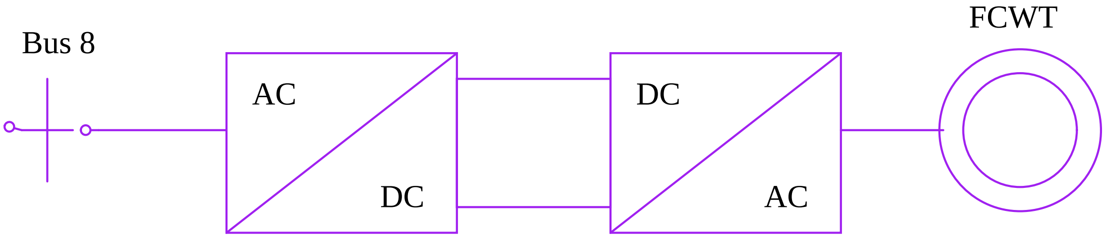

Figure 14: GFM converter concept.

2.2.1 RSC controls

Rotor-side converter manages the control of the operating conditions of the PMSG. Figure 15 shows the control diagram applied to the rotor-side converter. The control loops included in this diagram deal with the tracking of the maximum active power generated by the PMSG and also with the magnetizing current needed (i.e. reactive power or voltage control). So, to control the active and reactive power at the PMSG, the rotating speed and the voltage at generator terminals are used parameters. For the active power control loop (emphasized in red in Figure 15), the generator speed reference is calculated according to the well-known equation (19a) of the optimum rotating speed ω_{opt} based on the active power and the optimum k_{opt} factor (19b):

$$\omega_{opt} = \left(\frac{P}{k_{opt}}\right)^{1/3} \tag{19a}$$

$$k_{opt} = \frac{0.5\rho A r^3 C_{p.max}}{\lambda_{opt}^3} \tag{19b}$$

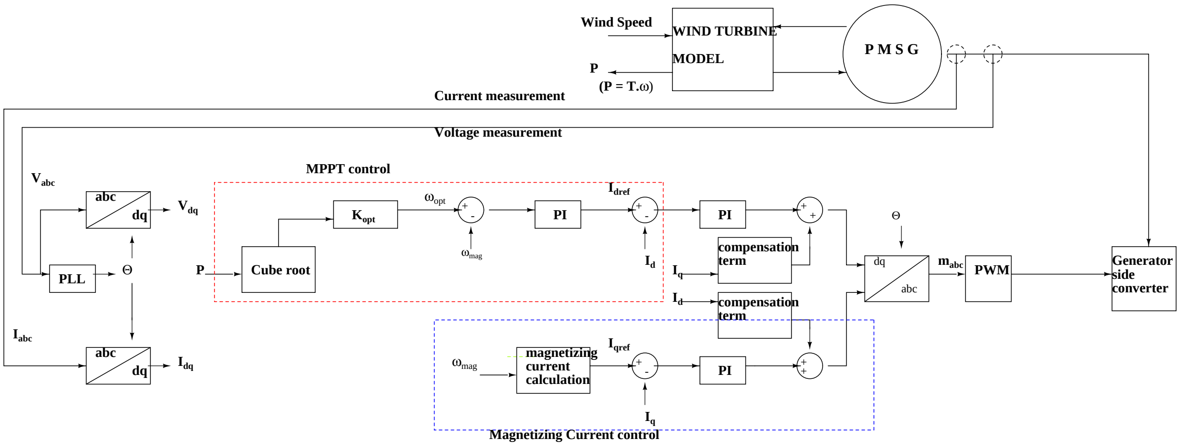

Figure 15: RSC control scheme.

2.2.2 GSC control

At the grid side, for the proper active power exchange between the generator side and the grid, the DC voltage at the DC bus is controlled. A DC Voltage reference is given by the user to keep the active power balance between the incoming active power from the generator side and the outgoing active power to the grid side. Besides, to establish reactive power control, the AC voltage at the PCC of the grid is the variable controlled during the steady-state operation. For the negative sequence control. A strategy where both negative sequence currents are set to zero (to inject only positive sequence during the grid fault, even in the case of an asymmetrical fault) and negative sequence current proportional to the negative sequence voltage, is applied. The scheme can be seen in Figure 16.

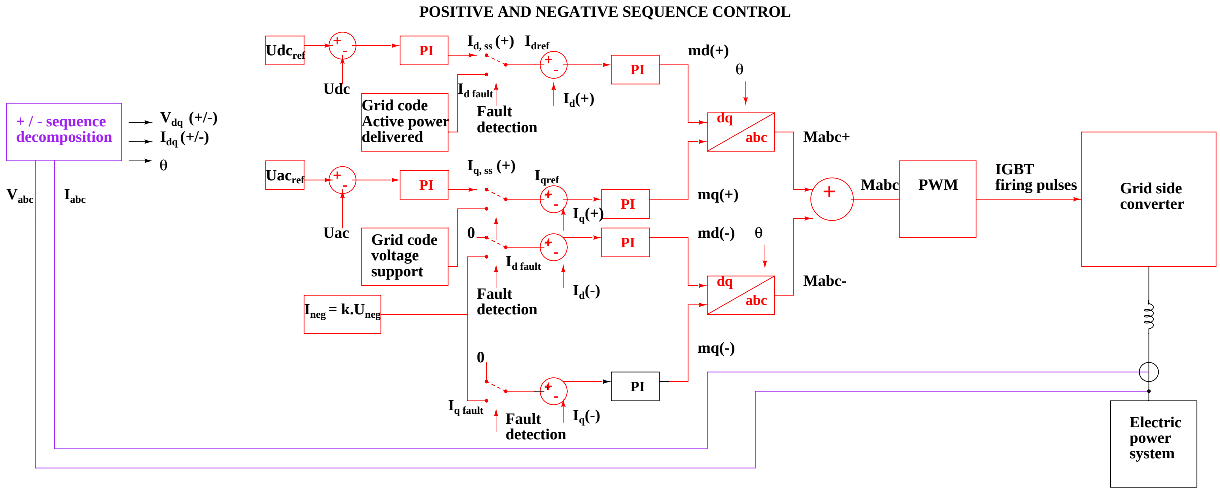

Figure 16: GSC control scheme.

Now the original control schemes of the benchmark WT models have been defined. In the next section, a detailed stability analysis of the VSM GFM control strategy is presented based on its application on a simplified circuit.

3 Stability Analysis of VSM Control Strategy

This section covers stability analysis for the virtual synchronous Machine (VSM) control strategy. Fundamentals of the VSM strategy have been already discussed in the section 1.3. This section covers first the implementation of the VSM strategy in more detail followed by the derivation of the transfer function for the VSM strategy applied to a simplified circuit. This is followed by the observation of stability margins on Bode plots by changing the values of key parameters.

3.1 Implementation of VSM

The basic control structure of VSM includes active Ppwer control, reactive power control, supplementary damping control, and current limitation control. The active power control, as has been already discussed in the previous section embodies the virtual swing equation as can be seen in Figure 25.

3.1.1 Reactive power control

The amplitude of DFIG's rotor excitation voltage can be produced by the reactive power control. The reactive power control is based on the concept of $Q-V$ droop characteristics as discussed in the section 1.1. Hence, the reactive power droop control for VSC's is derived as:

$$\Delta E = \ k_v(Q_{ref} - \ Q). \tag{20}$$

3.1.2 Supplementary damping control

It is known that oscillations will occur in the rotor speed of SG following the disturbances on the electromechanical time scale in the power grid. These rotor oscillations influence the rise of the induced current in the field and damper windings, which produces the damping torque in phase with the rotor speed, especially in the damper windings. The same principle also applies to DFIG when adopting VSM due to the resulting strong electromechanical coupling characteristic of the inner potential, which makes DFIG and PMSG-based WT actively respond to disturbances in the power grid. However, there is no damper winding in DFIG and PMSG, and the resistances involved in both stator and rotor windings are very low. Therefore, supplementary damping control is necessary to provide a damping contribution to stabilizing the DFIG and PMSG-based WT S. Wang, Hu, and Yuan, 2015. The damping power is produced by:

$$P_D = D(\omega - \omega_1), \tag{21}$$

where D is the damping coefficient, and ω_1 is the measured grid frequency. ω_1 can also be the rated grid frequency, represented by ω_o to distinguish it from grid frequency.

3.1.3 Current limitation control

A virtual resistance is suggested to effectively suppress the current transients. The control law is given by:

$$U_{rabc}^{ref} = U_{rabc} - R_v I_{rabc}, \tag{22}$$

where R_v is the virtual resistance, U_{rabc} is the generated rotor excitation voltage, and U_{rabc}^{ref} is the actual excitation voltage fed by RSC in the rotor rotating reference frame.

3.2 Controller design and stability analysis

In the work (S. Wang, Hu, & Yuan, 2015), modeling of Type-3 WT with VSC connected to an infinite-bus ac system, as shown in Figure 17, is built to study the influence of controller parameters and grid conditions on system performance, and to further design the system controllers theoretically. A weak ac system is typically characterized by a high impedance.

Note that the speed and pitch angle controls with relatively slow dynamics are not considered in this section. A reduced-order Type-3 WT model is first developed by considering the following conditions and assumptions:

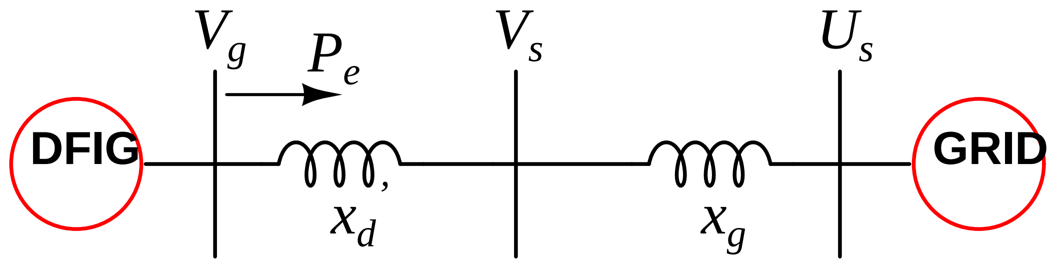

Figure 17: Circuit diagram of Type-3 WT connected to an infinite bus (S. Wang, Hu, & Yuan, 2015).

1. The generator convention is adopted in the stator, while the motor convention is in the rotor.
2. The rate of change of stator flux linkage, ψ_S is neglected.
3. The equations are derived in an ideally synchronous reference frame at constant speed ω_0, the d-axis of which aligns with the terminal voltage vector, U_t, in the initial case.

According to the work presented in (S. Wang, Hu, & Yuan, 2015), the simplified small-signal mathematical model of VSM-based Type-3 WT connected to the AC system can be seen in the Figure 18. The top loop in the figure can be referred to as active power loop and the bottom loop can be referred to as voltage control loop. The two inputs to the model are ΔP_e^{ref} for the active power loop and ΔU_t^{ref} for the voltage control loop. The power reference comes in from the MPPT controller output and the voltage reference comes in from the Reactive power droop control. The output of the model are phase angle $\Delta\theta_t$ for the active power loop and terminal voltage reference ΔU_t for the voltage control loop. With the help of the information given in (S. Wang, Hu, & Yuan, 2015), we will now go through the derivation of active power control closed loop transfer function (i.e the relation $\frac{\Delta\theta_t}{\Delta P_e^{ref}}$) and we will finally observe stability margins on Bode plots.

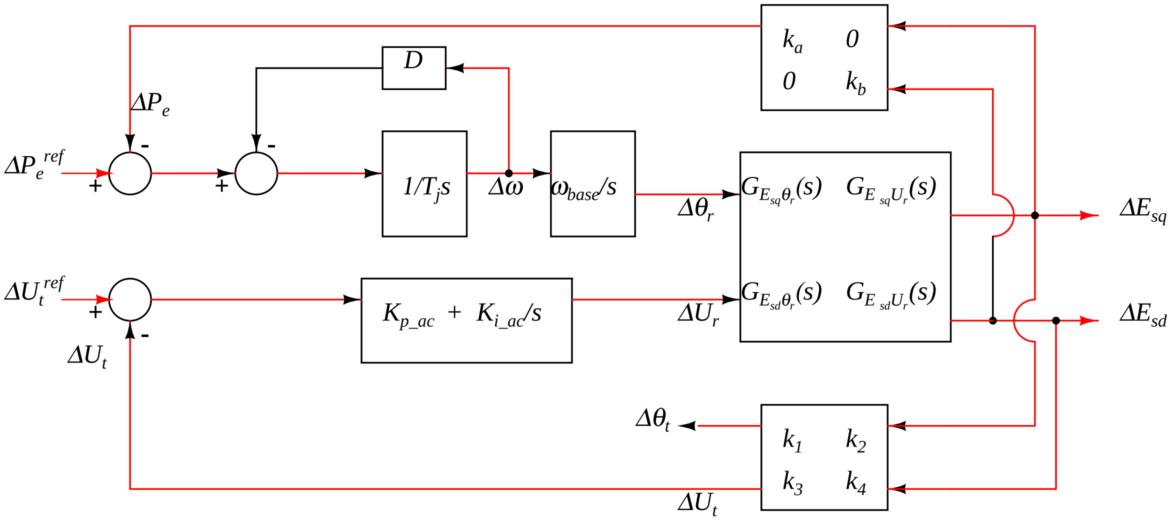

Figure 18: Simplified small-signal mathematical model of VSM-based Type-3 WT connected to ac system(S. Wang, Hu, & Yuan, 2015).

Referring to the Figure 18, the mathematical expressions for all the functions are as follows:

$$\Delta E_{Sd} = G_{Esd\theta_r}(s)\Delta\theta_r + G_{EsdU_r}(s)\Delta U_r, \tag{23a}$$

$$\Delta E_{Sq} = G_{Esq\theta_r}(s)\Delta\theta_r + G_{EsqU_r}(s)\Delta U_r, \tag{23b}$$

$$\Delta P_e = k_a\Delta E_{sq} - k_b\Delta Esd, \tag{24}$$

$$\Delta\theta_t = k_1\Delta E_{Sq} + k_2\Delta E_{Sd}, \tag{25}$$

$$\Delta U_t = k_3\Delta E_{Sq} + k_4\Delta E_{Sd}, \tag{26}$$

where

$$G_{Esd\theta_r}(s) = bU_{r0}\frac{\omega_{slip0}\sin\theta_{r0} - (a-s)\cos\theta_{r0}}{\omega_{slip0}^2 + (a-s)^2}, \tag{27a}$$

$$G_{EsdU_r}(s) = -b\frac{\omega_{slip0}\cos\theta_{r0} + (a-s)\sin\theta_{r0}}{\omega_{slip0}^2 + (a-s)^2}, \tag{27b}$$

$$G_{Esq\theta_r}(s) = -bU_{r0}\frac{\omega_{slip0}\cos\theta_{r0} + (a-s)\sin\theta_{r0}}{\omega_{slip0}^2 + (a-s)^2}, \tag{27c}$$

$$G_{EsqU_r}(s) = b\frac{(a-s)\cos\theta_{r0} - \omega_{slip0}\sin\theta_{r0}}{\omega_{slip0}^2 + (a-s)^2}, \tag{27d}$$

and

$$k_a = \frac{U_{sd0}}{X'}, \tag{28a}$$

$$k_b = \frac{U_{sq0}}{X'}, \tag{28b}$$

$$k_1 = \frac{x_g}{X'}\frac{U_{td0}}{U_{t0}^2}, \tag{28c}$$

$$k_2 = -\frac{x_g}{X'}\frac{U_{tq0}}{U_{t0}^2}, \tag{28d}$$

$$k_3 = \frac{x_g}{X'}\frac{U_{tq0}}{U_{t0}}, \tag{28e}$$

$$k_4 = \frac{x_g}{X'}\frac{U_{td0}}{U_{t0}}, \tag{28f}$$

and a, b and X are defined as follows

$$a = \frac{-1}{T_0'}\frac{X}{X'}, \tag{29}$$

$$b = -\omega_{base}\frac{L_m}{L_r}, \tag{30}$$

$$X = x_d + x_g, \tag{31}$$

$$X' = x_d' + X_g, \tag{32}$$

$$T_0' = \frac{L_r}{(R_r + R_v)\omega_{base}} \tag{33}$$

$$x_d = L_S, \tag{34}$$

$$x_d' = L_S - \frac{L_m^2}{L_r}. \tag{35}$$

Based on Figure 18 and equation (23) to (28), we will be deriving the active power closed-loop transfer function from the above information. Observing the active power loop of figure 18 till the output of small signal rotor voltage angle $\Delta\theta_r$, we can write:

$$(\Delta P_e^{ref} - \Delta P_E - D\Delta\omega)\frac{1}{T_j s} = \Delta\omega \tag{36}$$

re-arranging terms in above gives:

$$\Delta\omega = \frac{(\Delta P_e^{ref} - \Delta P_E)}{T_j s + D}. \tag{37}$$

Going further through the integration we can write:

$$\Delta\omega\frac{\omega_{base}}{s} = \Delta\theta_r = \frac{(\Delta P_e^{ref} - \Delta P_E)}{(T_j s + D)}\frac{\omega_{base}}{s}. \tag{38}$$

From (23) and (26), we can write:

$$\Delta U_t = (k_4 G_{ESd\theta_r}(s) + k_3 G_{ESq\theta_r}(s))\Delta\theta_r + (k_4 G_{ESdU_r}(s) + k_3 G_{ESqU_r}(s))\Delta U_r. \tag{39}$$

Now, from the above equation, let $(k_4 G_{ESd\theta_r}(s) + k_3 G_{ESq\theta_r}(s))$ be denoted by A and let $(k_4 G_{ESdU_r}(s) + k_3 G_{ESqU_r}(s))$ be denoted by B from here onwards. And from the Figure 18, considering $\Delta U_{ref} = 0$ we get:

$$\Delta U_t = -\frac{\Delta U_r}{(K_{pac} + \frac{K_{iac}}{s})} \tag{40}$$

Now, by equating the right-hand side of equations (39) and (40) we get:

$$-\frac{\Delta U_r}{(K_{pac} + \frac{K_{iac}}{s})} = A\Delta\theta_r + B\Delta U_r \tag{41}$$

which gives an expression for ΔU_r as:

$$\Delta U_r = -\frac{A\Delta\theta_r(K_{pac} + \frac{K_{iac}}{s})}{1 + B(K_{pac} + \frac{K_{iac}}{s})} \tag{42}$$

To maintain clarity, we further denote the coefficient of $\Delta\theta_r$ in above equation i.e $-\frac{A(K_{pac}+\frac{K_{iac}}{s})}{1+B(K_{pac}+\frac{K_{iac}}{s})}$ to be denoted by TF. Hence the above expression becomes:

$$\Delta U_r = TF\Delta\theta_r \tag{43}$$

Now using equation (24) in equation 38 and re-arraning we get:

$$\Delta P_e^{ref} = \frac{\Delta\theta_r(T_j s^2 + Ds)}{\omega_{base}} + k_a\Delta E_{Sq} + \Delta E_{Sd} \tag{44}$$

Using equations (23) and 43, we can write:

$$\Delta P_e^{ref} = [\frac{(T_j s^2 + Ds)}{\omega_{base}} + k_a(G_{Esq\theta_r}(s) + TFG_{EsqU_r}(s)) + k_b(G_{Esd\theta_r}(s) + TFG_{EsdU_r}(s))]\Delta\theta_r. \tag{45}$$

Now expanding equation equation (25) using equations (23) and (43), we can write:

$$\Delta\theta_t = (k_1 G_{Esq\theta_r}(s) + k_1 Tf G_{EsqU_r}(s) + k_2 G_{Esd\theta_r}(s) + k_2 TFG_{EsdU_r}(s))\Delta\theta_r. \tag{46}$$

Finally using (46) in (45) we get the Closed loop transfer function of the active power loop as:

$$\frac{\Delta\theta_t}{\Delta P_e^{ref}} = \frac{(k_1 G_{Esq\theta_r}(s) + k_1 TFG_{EsqU_r}(s) + k_2 G_{Esd\theta_r}(s) + k_2 TFG_{EsdU_r}(s))}{[\frac{(T_j s^2+Ds)}{\omega_{base}} + k_a(G_{Esq\theta_r}(s) + TFG_{EsqU_r}(s)) + k_b(G_{Esd\theta_r}(s) + TFG_{EsdU_r}(s))]} \tag{47}$$

The bode plot of the above-derived transfer function in equation (47) was plotted on MATLAB using resistance and impedance values corresponding to the Benchmark model. Multiple plots were obtained for different values of the damping constant. The figures below show the Bode plots with corresponding gain and phase margins (Figure 19) and peak responses (Figure 20).

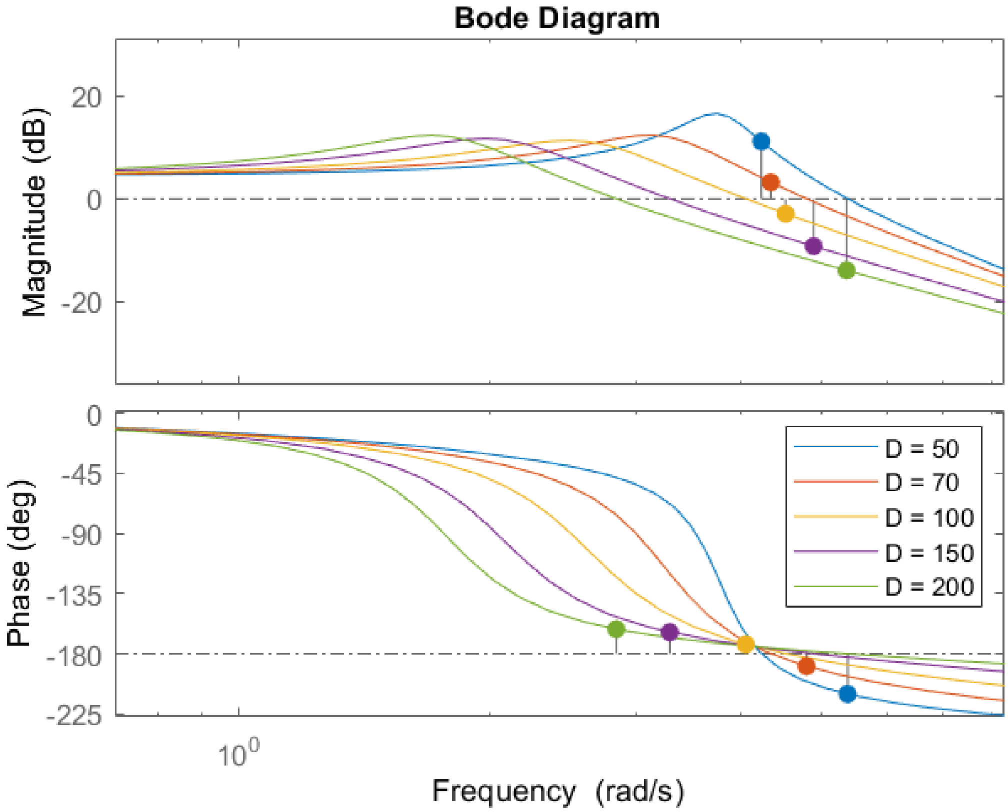

Figure 19: Bode Magnitude Plot showing stability margins.

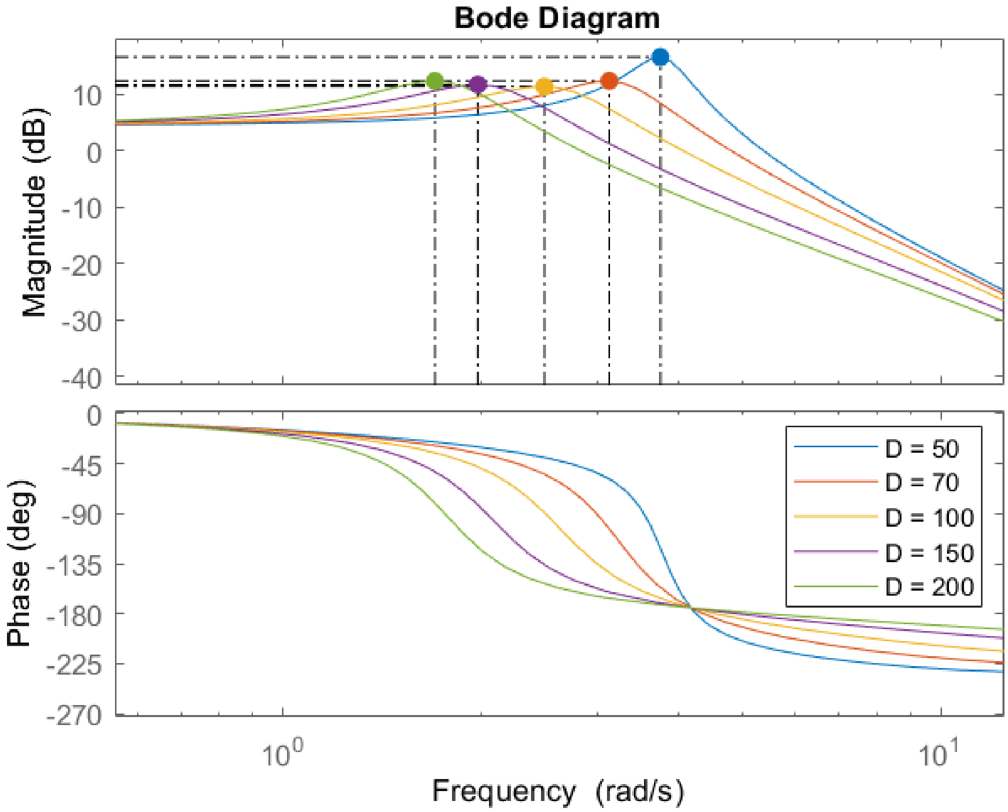

Figure 20: Bode Magnitude Plot showing Peak responses.

From Figure 19 we observed that for D, i.e. damping constant values higher than 100, the gain and phase margins come in the stable range with values of 150 and 200 providing acceptable levels of margins. On observing Figure 20, we noted that the Damping constant value of $D = 150$ provides the lowest peak response, i.e. highest damping effect which is crucial for DFIG stability. The peak response decreases from $D = 50$ till $D = 150$ and again increases for $D = 200$. Hence, the stability analysis yields an optimum value of $D = 150$.

The stability analysis provides us with confidence to move towards the application of the VSM control strategy to the Benchmark Type-3 and Type-4 WT models which will be presented in next section. The model contains a relatively complicated circuit whose grid strength can be varied by varying the impedance values of the infinite ac source connected to one of the buses in the grid.

4 GFM Control implementation

This section summarizes the application of VSM (GFM) control strategy methodology on the existing Type-3 and Type-4 WTs in the MIGRATE benchmark model. For Type-3 WT, initially, the original controls of the RSC will be presented, followed by the changes which were made to convert the original controls to GFM controls. Finally, an intermediate voltage control loop was derived in the application process, which will be discussed in detail. Following this, the original controls and GFM application for Type-4 WT on the GSC will be discussed.

4.1 Type-3 WT control of the RSC

The theoretical aspect of the original RSC controls has been briefly discussed in the second chapter. This subsection will show further details and practical implementation of the schematic shown in figure 13 into the benchmark model. Also, it will briefly discuss the crowbar protection scheme.

4.1.1 Implementation of maximum power point tracking (MPPT) algorithm

Maximum power point tracking control from equation 9 expresses reference quadrature current. The practical implementation of this equation in the benchmark model can be seen in Figure 21.

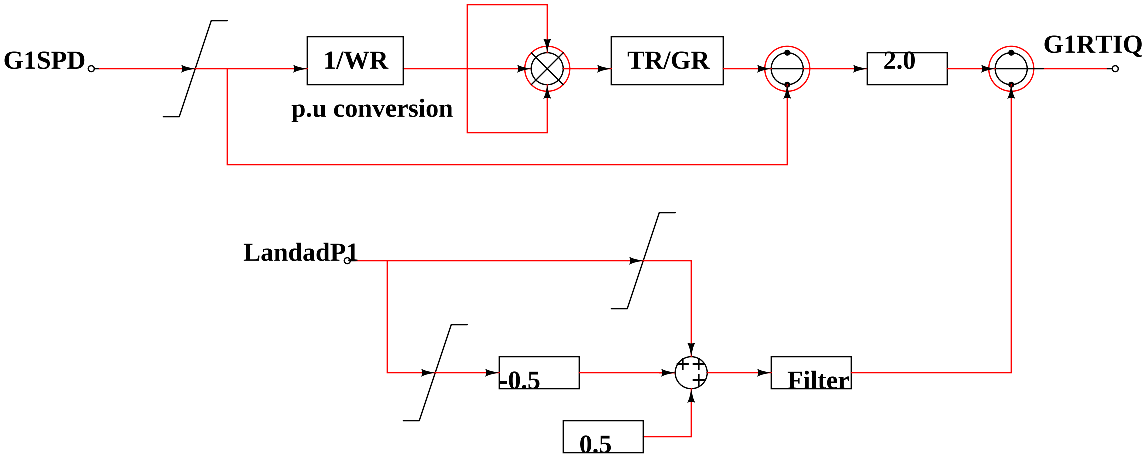

Figure 21: Optimal power point tracking in Benchmark model RSC controls.

In Figure 21, The signal **G1SPD** is the rotor angular frequency which is converted to per unit value by dividing through rated rotor speed **WR** and then cubed to give power reference. Furthermore, the generator power is converted to turbine power by passing through a second gain containing the ratio of turbine-rated power **TR** by generator rater power **GR**. Then it is further divided by the angular speed itself to get the reference torque value. Finally, the formula (9) is realized further to get the output signal **G1RTIQ**, which represents the reference quadrature current. This current goes as an input to the inner current controller in the original control strategy.

4.1.2 Implementation of inner current regulators

The implemented inner controller for the positive sequence can be seen in Figure 22. The reference quadrature current generated from the outer MPPT control discussed above comes in as an input to the inner controller, as it can be seen in the bottom of Figure 22 above in cyan color. The reference current for the direct axis comes from the implementation of grid code regulations, the details of which will not be discussed to limit the scope. The inner controller where the Crowbar protection scheme is actuated. The input signal **CrowR** in the above Figure 22 comes from the crowbar protection control, which controls the reference current inputs and reset value for the integrator.

The crowbar control system is a conventional approach to protect the RSC from DFIG rotor over-current. This system is connected to the rotor windings, as shown in Figure 23. The rotor currents would increase in the case

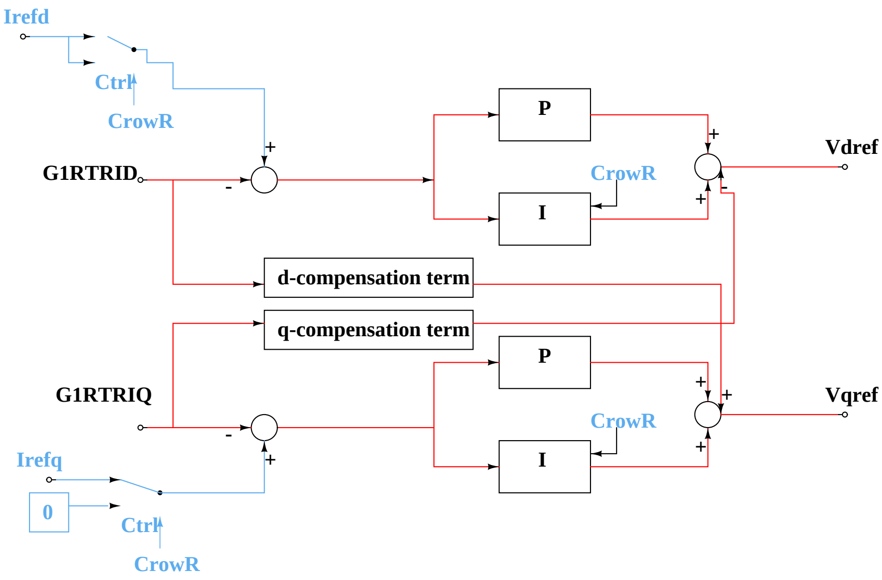

Figure 22: Inner current controllers of RSC control.

of fault. If the currents exceed the surge capability of each IGBT, the crowbar system is activated and diverts the currents through the rectifier to the resistor to dissipate the initial energy outflow from the machine.

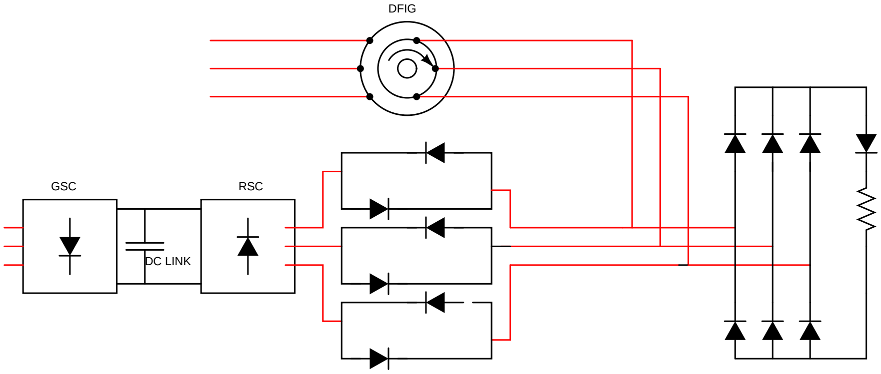

Figure 23: Crowbar protection.

The crowbar control logic is shown in the Figure 24. The rotor current in each phase is compared with a threshold (2 pu in this case). If the current in any phase exceeds the threshold, the crowbar is triggered and remains active till the current goes below the defined threshold.

4.2 Application of GFM control strategy for Type-3 WT model RSC

The basic GFM Type-3 model control mainly includes WT, RSC, and GSC control. The reference value of active power is generated by the control of the wind turbine, which imitates the prime mover system of the traditional synchronous machine, and then the independent control of rotor excitation voltage amplitude and frequency is realized through the virtual synchronous control of the rotor side. The GSC is mainly used to maintain the stability of DC voltage. The Type-3 WT under the GFM control is mainly realized through the control of the RSC, and the vector control mode based on PLL synchronization is adopted to control GSC.

4.2.1 RSC Control

The RSC control of the GFM Type-3 WT model adopts the method of virtual synchronous control. The frequency/phase of rotor excitation voltage is adjusted by unbalanced active power through a virtual rotor motion

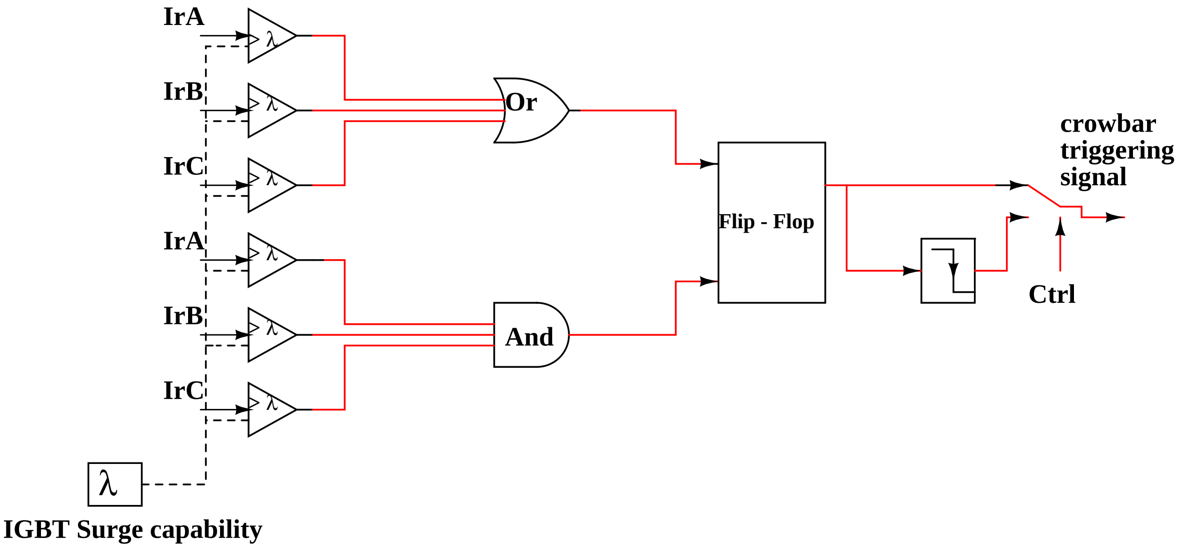

Figure 24: Crowbar control logic.

equation (swing equation), to realize the adjustment of frequency/phase of internal potential. The amplitude of rotor excitation voltage is adjusted by unbalanced reactive power through the PI controller, to adjust the amplitude of internal potential. It mainly includes power synchronization control, reactive power/terminal voltage control, damping control and virtual resistance current limiting control. The overall control diagram is shown in the Figure 25.

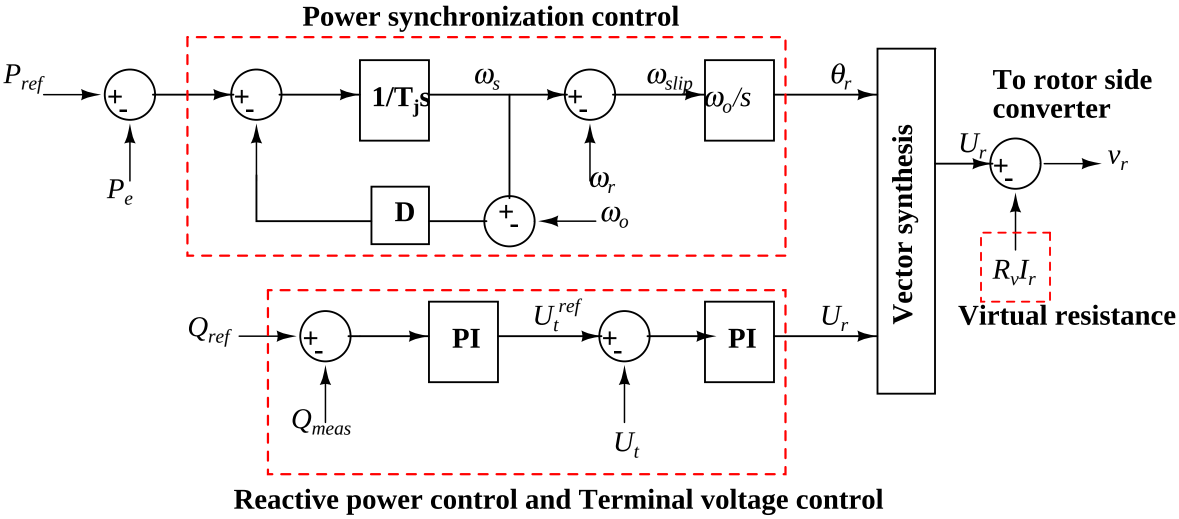

Figure 25: RSC Virtual Synchronous Machine Control, (Hu, Chi, et al., 2022; Hu, Lei, et al., 2022).

4.2.2 GSC control

The GSC control of the GFM Type-3 WT model adopts the traditional vector control, and its main function is to maintain the stability of DC bus voltage. In the case of terminal voltage orientation, the active and reactive power control is decoupled, and the d-axis current controls the active power, and the q-axis current controls the reactive power. To reduce the capacity of the grid-connected converter as much as possible, the reference value of the q-axis component of the current is often set to 0. The control of DC bus voltage is mainly to maintain the stability of DC voltage UDC by adjusting the reference value of the d-axis component of the current.

4.2.3 Change in the MPPT control logic

As we have seen previously, the VSM control strategy takes in the reference power as an input (see Figure 25). The current MPPT logic, as discussed previously, gives the reference quadrature current as an output. Hence, the current MPPT logic must be altered to give the Power reference as its output. The optimal power to be extracted from a wind turbine is a function of turbine shaft speed raised to the third power as:

$$P_{opt} = K_{opt}\omega_r^3, \tag{48}$$

considering the torque expression ($T = \frac{P}{\omega_r}$), the optimal electrical torque is a function of turbine shaft speed raised to the second power. Considering the equation (9) along with the above-explained logic, we can trace back in the current MPPT control logic to the point which represents the power reference. The point denoted by the blue dot in Figure 26 represents the power reference output. Hence, after applying the above logic, the new MPPT control logic looks like in Figure 27.

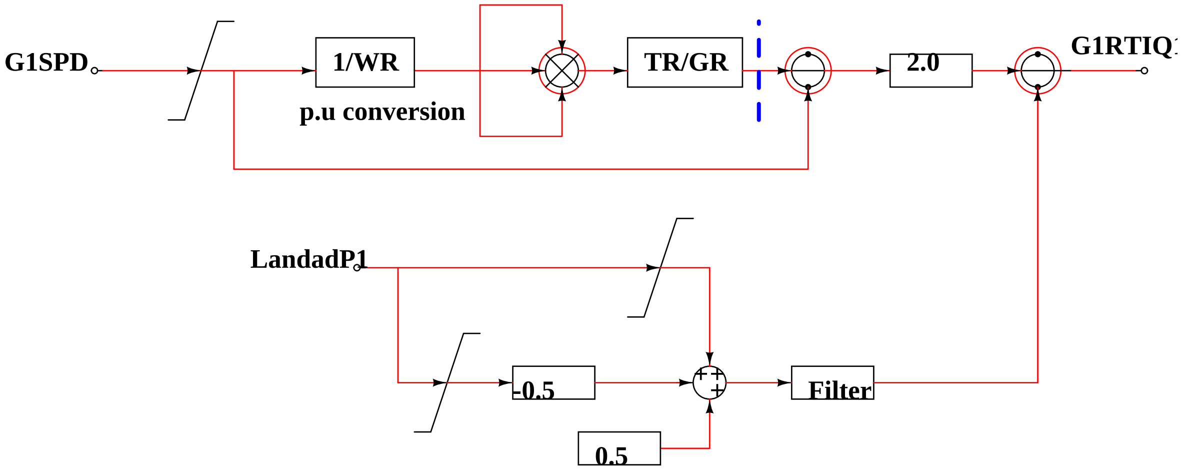

Figure 26: Active power reference point.

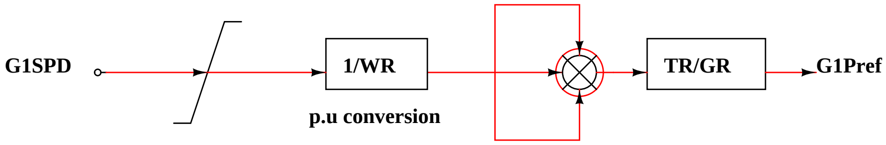

Figure 27: Revised MPPT logic.

4.2.4 Inserting the VSM control

The Active power control loop of the VSM control strategy takes the active power reference as the input and gives the voltage angle as the output. Hence, the position of the VSM control has to be placed after the MPPT control so that the produced voltage angle can be used for Park transformations of the inner controllers.

Also, the reactive power control gives rotor voltage magnitudes as the output, which cannot be used directly as references with the inner current controllers. Hence based on the characteristic equations of the induction generator, an intermediate voltage controller has to be inserted after the reactive power control of the VSM control and before the innermost current controller so that current references for the inner-most controllers can be produced. The new proposed control strategy can be summarized as per Figure 28.

The Figure 28 shows that the VSM control (containing the active power control loop and reactive power control loop) is sandwiched between the modified MPPT control (which gives power reference as output instead of current reference) and the inner current controller.

The applied VSM controller's active power control loop and reactive power control loop can be seen in Figures 29 and 30. The value of the damping constant is taken as 150, as has been extensively discussed in the section on stability analysis. The typical inertia constants for SGs of the large conventional power plants are in the range of 2–9 s, and the physical inertia constant of the modern large WT is more or less equal to the average

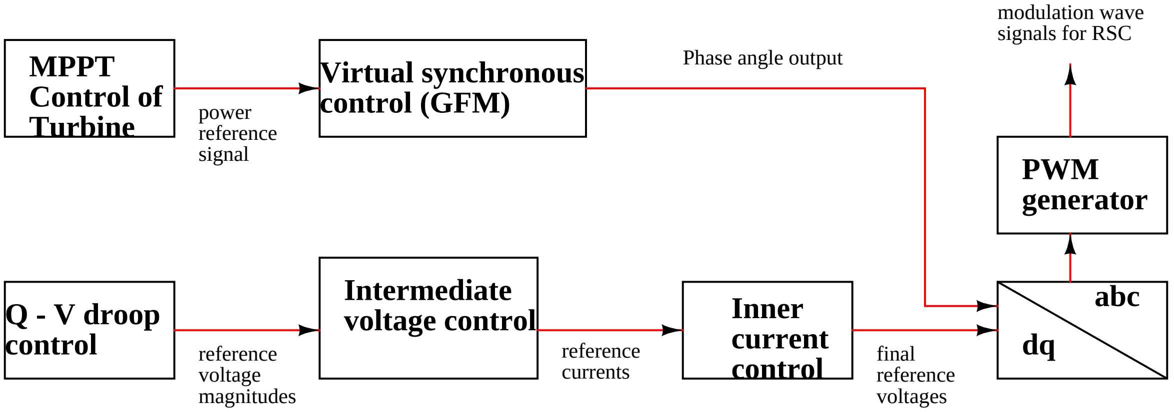

Figure 28: New control strategy for RSC.

of the conventional power plants. In our analysis, the inertia constant $T_j = 10$, mimics SG's inertial response behavior with $H = 5$ s. The reference reactive power is taken as zero.

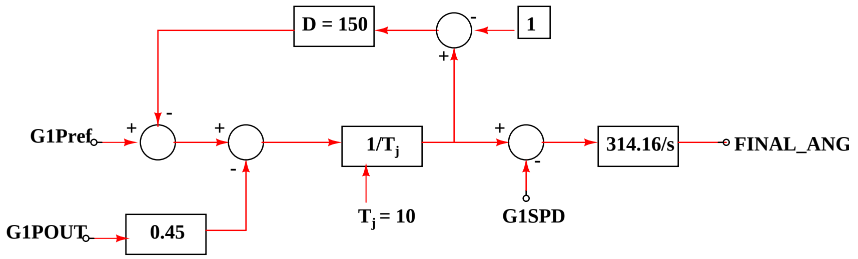

Figure 29: Active power control loop of applied VSM control strategy.

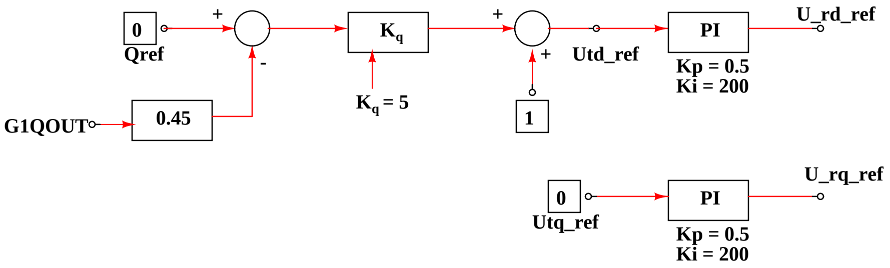

Figure 30: Reactive power control loop.

In the above two figures 29 and 30, the gains in front of the inputs are factors to convert in per unit values. It has to be noted carefully that the signal **FINAL_ANG** represents generated slip voltage angle that a PLL originally generated. This angle is used for Park transformations and reverse Park's Transformation of Input and output rotor voltages and currents for inner controllers. When it is to be used for Park transformations of stator quantities, it must first be added to the rotor angle to generate the full voltage angle. The signals **U_rd_ref** and **U_rq_ref** will be used as references in the intermediate voltage controller.

4.3 Derivation of the intermediate Voltage Controller for Type-3 WT RSC

This sub-section shows the process flow of designing the controller and the derivation of compensation terms. The DFIG rotor voltage equations (7e), (7f) can be written in Laplace domain as:

$$v_{dr}(s) = R_r i_{dr}(s) + \sigma L_r s i_{dr}(s) - \omega_{slip}\sigma L_r i_{qr}(s), \tag{49}$$

$$v_{qr}(s) = R_r i_{qr}(s) + \sigma L_r s i_{qr}(s) + \omega_{slip}(L_{ms} i_{ms}(s) + \sigma L_r i_{dr}(s)), \tag{50}$$

using the principle of superposition, we can derive the transfer function and corresponding compensation terms as:

$$\frac{i_{dr}(s)}{v_{dr}(s)}{}_{i_{qr}=0} = \frac{i_{qr}(s)}{v_{qr}(s)}{}_{i_{dr},i_{ms}=0} = \frac{1}{R_r + s\sigma L_r}, \tag{51}$$

$$\frac{i_{qr}(s)}{v_{dr}(s)}{}_{i_{dr}=0} = \frac{-1}{\omega_{slip}\sigma L_r}, \tag{52}$$

$$\frac{i_{dr}(s)}{v_{qr}(s)}{}_{i_{qr}=0} = \frac{1}{\omega_{slip}\sigma L_r} + \omega_{slip} L_m i_{ms}. \tag{53}$$

The above equations (49), (50) can be represented in the control block form in the figure 31 below. The compensation terms are represented by the right-hand side of equations (52) and (53) and are denoted in the figure by names ’comp1’ and ’comp2’, respectively.

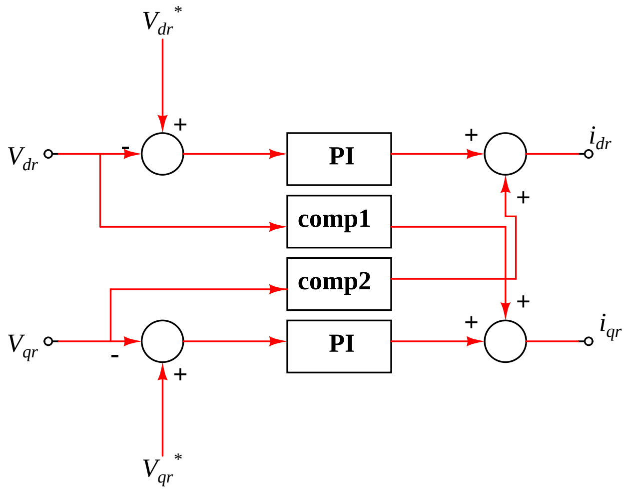

Figure 31: Voltage controller block diagram.

In Figure 31, the dq voltage references denoted by V_{dr}^* and V_{qr}^* are output from the preceding reactive power controller of the VSM control. The PI controllers for the intermediate controller are tuned by the Zeigler-Nichols step response method. The proportional and integral gain values obtained from the Zeigler-Nichols step response tuning method serve as a starting point, and the values are further optimized through multiple iterations and observing the controller behavior. The initially tuned PI controller plots on the SISO-TOOL of MATLAB can be seen in Figure 32 below.

4.4 Type 4 WT control of GSC

This subsection briefly discusses the practical implementation of GSC controls, including DC voltage control and reactive power/AC voltage control. It also briefly discusses the implementation of an inner current controller and its protection scheme.

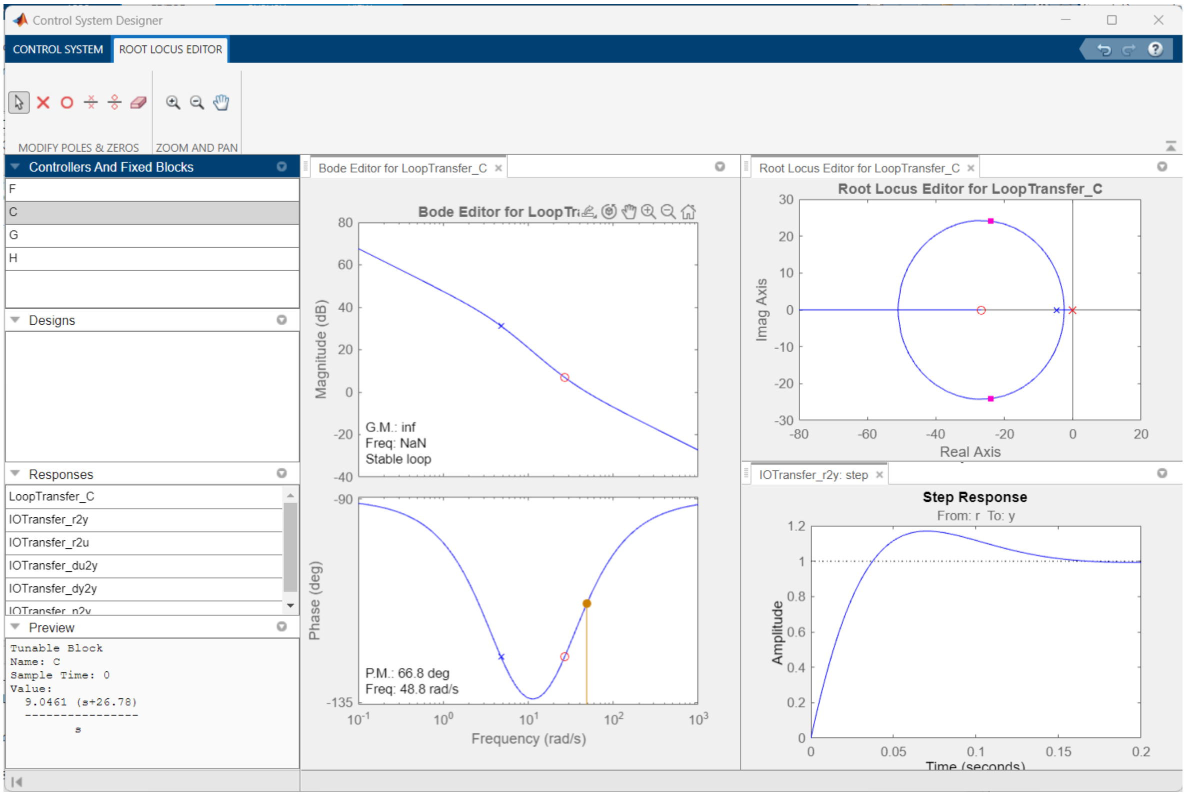

```
Tunable Block
Name: C
Sample Time: 0
Value:
  9.0461 (s+26.78)
  ----------------
         s
```

```
G.M.: inf
Freq: NaN
Stable loop
```

```
P.M.: 66.8 deg
Freq: 48.8 rad/s
```

Figure 32: PI controller tuning.

4.4.1 Implementation of DC link voltage and AC voltage control

As discussed previously (see figure 16, the GSC originally contains the DC voltage control through the direct axis current reference. The quadrature axis current reference is generated through AC voltage control to control the reactive power ultimately. The DC link control and AC voltage control can be seen in Figures 33 and 34 below.

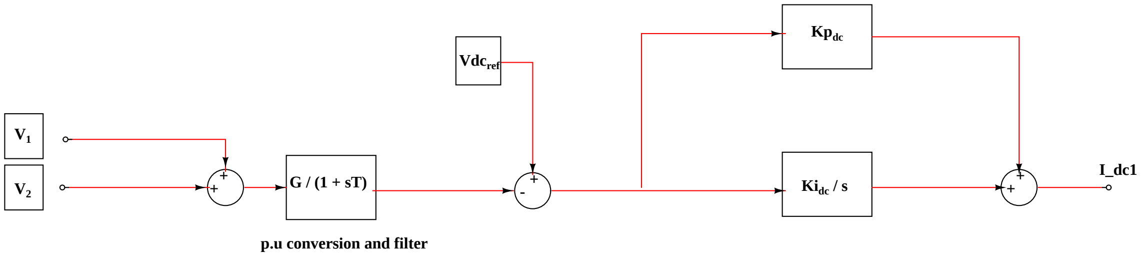

Figure 33: GSC - DC Voltage control.

Referring to the above figure 33, the inputs **V1** and **V2** come in from the PMSG machine, which gets compared with the reference DC voltage value and generates an error to be passed through the PI control. The output signal **I_dc1** goes in as a reference for inner current controllers. Following a similar methodology, the output signal **I_ac1** in Figure 34 acts as a reference for the inner current controller.

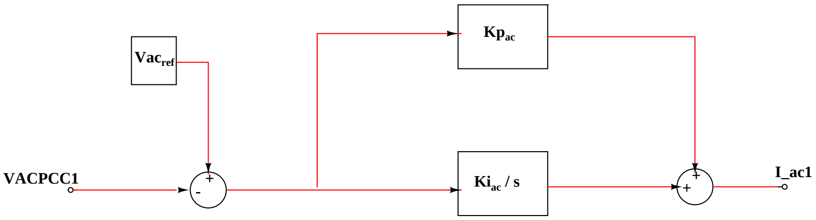

Figure 34: GSC - AC Voltage control.

4.4.2 Implementation of inner current controller

The theoretical aspect of the inner current controller design has been discussed in detail in the first two sections. The direct axis part of the implemented inner controller in the model can be seen in Figure 35.

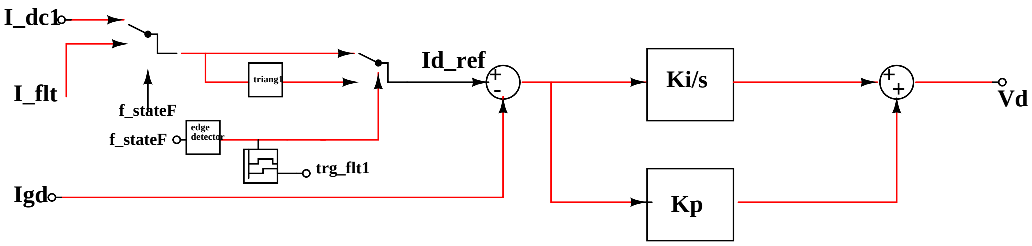

Figure 35: Direct axis side of Inner current controller.

In the above figure 35, one can see that the reference d-axis current is the output signal of DC voltage control. The current error signal gets through a PI controller, as was previously shown in figure 16. On closely observing Figure 35, one can see that the incoming reference signal depends on a signal named **f_stateF**, which controls the signal which comes in as the reference. Through this signal, the positive sequence current controller deals with reactive power support during a fault situation. Once the fault appears, both single phase to ground, double phase to ground, double phase, or three phase faults, if the positive sequence voltage goes below 0.9 p.u., the control system detects the fault situation and enters in the voltage support working mode.

4.5 Application of GFM control strategy

The GFM strategy for the Type-4 WT is achieved by applying VSM control on the GSC, inner voltage, and current controllers down the line. The DC link voltage control is to be achieved with the MSC since it performs better as the MSC is decoupled from the grid's disturbance. This approach will be called M-GFM (MSC controls the DC-link voltage). The active power response of M-GFM types under normal operation relies on the grid's strength. Thus, an optimal design of virtual synchronous machine for the M-GFM types should be considered. The strategy can be seen in Figure 36.

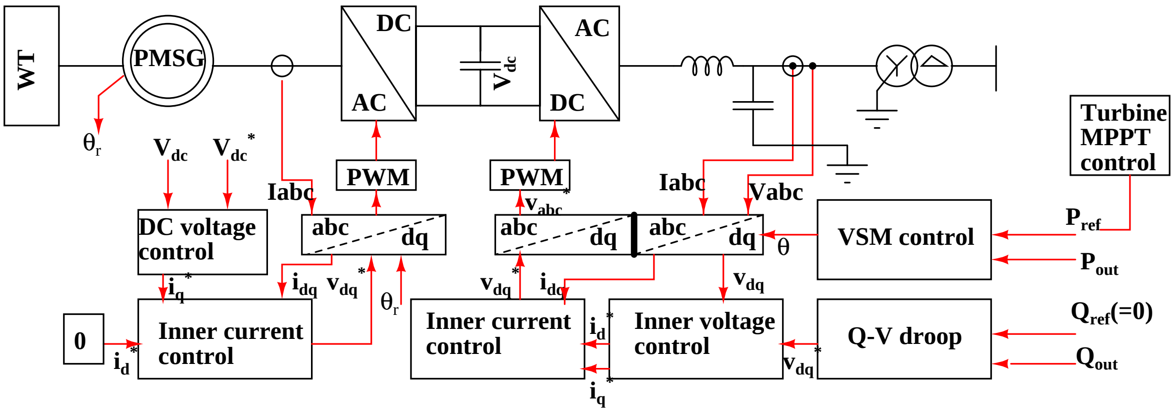

Figure 36: Type-4 WT model GFM Control scheme, (Gao et al., 2021; Ji et al., 2022; Liu et al., 2022; Nguyen & Vu, 2022).

This subsection will discuss implementing the VSM strategy to the original controls of the GSC. This will be followed by the changes that make the entire control strategy work.

4.5.1 Application of VSM control to the GSC

As we discussed, the GSC originally contains the DC link voltage control and AC voltage control at its direct and quadrature axis controls, respectively. As discussed previously, the grid forming control strategy produces voltage angles and magnitudes for both direct and quadrature axes, which proceeds with the MPPT control and precedes an intermediate voltage controller. The difference in the voltage controller is that the controlled voltage is that of the stator rather rotor (as was in Type-3), and the rest of the procedure and the characteristic equation is the same as that of the Type-3.
The main difference lies in implementing the VSM control of the Type-4 WT. The Active power loop of the VSM strategy for the Type-4 turbine generates a full stator angle rather than a slip angle, as was the case with the VSM strategy for the Type-3 turbine; the implemented Active power loop from the model can be seen in the figure 37 below.

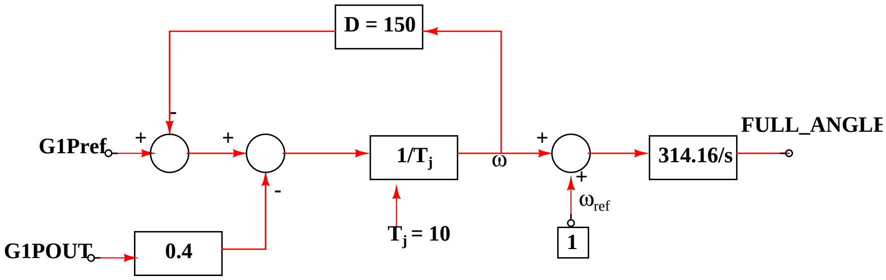

Figure 37: Active power loop of VSM control for Type-4 WT.

If you compare the above figure 37 with figure 29, the output signal from the PI control is an error in the case of figure 37, which then gets added to the reference frequency value. While on the contrary, the output signal from the PI controller in figure 29 is a full frequency and not an error that gets subtracted from the rotor frequency to get the slip frequency. Hence the overall control schematic for the GSC is exactly the same as that of the Type-3 RSC, which was shown in Figure 28, previously.

4.5.2 Changes made to the MSC controls

The MSC originally helped the responsibility of active power control on its direct axis side and magnetic current control on the quadrature axis. (Nguyen & Vu, 2022) mentioned that the grid forming Type-4 turbine dedicates the MSC for DC link voltage control at its quadrature axis side. The direct axis current reference can be taken as zero. The DC link voltage control shown in Figure 33 is shifted to the MSC control, and the output of the DC link control is fed as a reference to the inner current controller. Hence, the implemented strategy for the MSC can be seen in Figure 38.

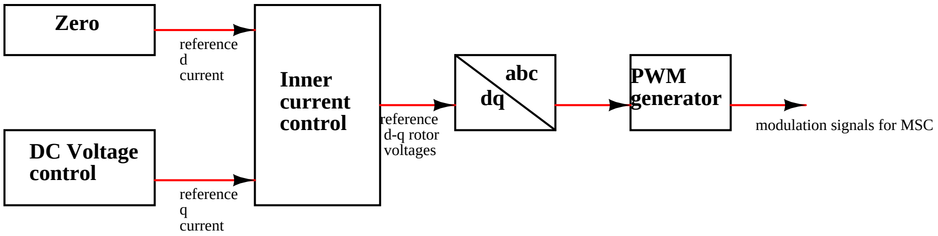

Figure 38: New MSC control scheme for Type-4 WT.

A detailed implementation process of the GFM control on benchmark models is now observed. In the next section, results of various tests performed in order to form a comparative analysis between GFL and GFM control strategies are presented and discussed.

5 Tests and Results Discussion

This section provides information on the tests performed on both Type-3 and Type-4 GFM and GFL WT models separately, which will be followed by a discussion about the results obtained for those tests.

5.1 Tests Performed

To draw out a comparative analysis between GFM and GFL strategies, various tests were performed on both Type-3 and Type-4 turbine models. Active power output, DC-Link voltage, and frequency were observed for the GFM model for different inertia constants and for the GFL model through power step and load step tests at different SCR values. Also, rotor and output currents were observed for single-phase faults. The tests summarized in Table 3 were performed.

Table 3: Tests performed on GFM and GFL models to draw a comparative analysis

TEST No.	Details
1)	Type-3 - Wind speed step up from 9 to 12 m/s at high (> 10) SCR value.
2)	Type-3 - Wind speed step up from 9 to 12 m/s at low SCR value of 9 (SGs off, HVDC link disconnected)
3)	Type-3 - Wind speed step up from 9 to 12 m/s at very low SCR (< 5) (SGs off, HVDC link disconnected)
4)	Type-3 - Load Step from 70 to 370 MW up at $SCR > 10$
5)	Type-3 - Single phase fault generation at $SCR = 9$ (HVDC link connected)
6)	Type-3 - Double phase fault generation at $SCR = 9$ (HVDC link connected)
7)	Type-3 - Three-phase fault generation at $SCR = 9$ (HVDC link connected)
8)	Type-3 WT - double phase fault at $SCR < 5$ (HVDC link connected)
9)	Type-3 WT - Three phase fault at $SCR < 5$ (HVDC link connected)
10)	Type-4 - Load step 70 to 370 MW at $SCR = 9$

5.2 Results and discussion

This subsection shows the results obtained for the tests performed on both turbine models as described in Table 3.

5.2.1 Test 1 - Type-3 WT wind speed step-up for different inertia constants in a strong grid with $SCR > 10$

Figures 39 and 40 below display the active power output and DC-link voltage variation for a wind speed step-up for inertia constant values of 5, 10, 20 for the GFL mode. The SCR for the grid is high (close to 20), and hence the grid is strong.
The Figures 39, 40 show that for a strong grid, the GFL is more stable and settles faster than the GFM. Due to the strong grid, the PLL, which is used to detect the voltage angle from the grid parameters, is stable; hence, the GFL strategy performs better. Figure 41 below shows a zoomed view of the GFM plot for different inertia constants. One can see that the optimal inertial constant value is 10, resulting in the highest minima in the variation of DC link voltage.

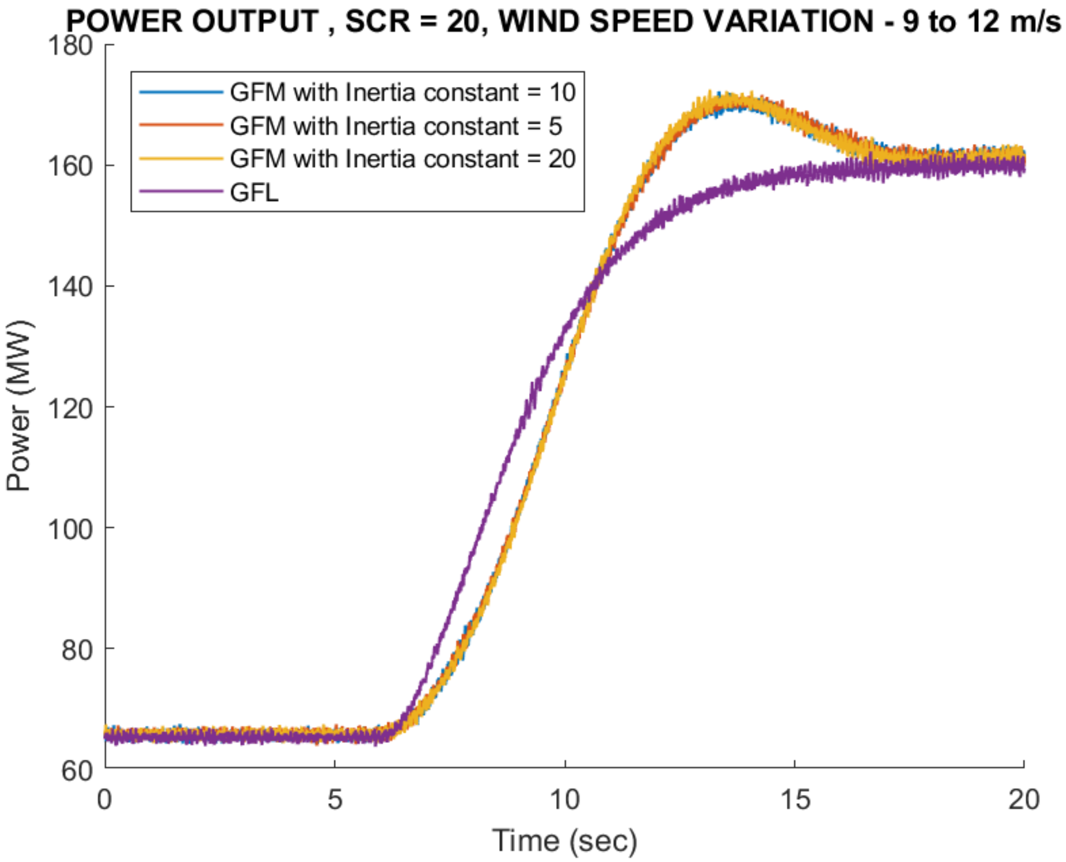

Figure 39: Active Power step up in GFM (Inertia constant values 10, 20 and 5) and GFL Type-3 WT for wind speed step up at $SCR > 10$ (Test no. 1).

5.2.2 Test 2 - Type-3 WT - wind speed step up for different Inertia constants in a weak grid with $SCR = 9$

Figures 42 and 43 below display the active power output and DC-link voltage variation for a wind speed step up for inertia constant values of 10 and for the GFL mode. The grid's SCR is low, so the grid is weak in this case. As one can clearly observe from the Figures 42, 43 below, the GFL strategy shows serious fluctuations and degradation in power quality. The main reason for this is the low SCR value or a weak grid, which results in poor performance of the PLL. Since the GFM strategy uses the active power loop for its voltage angle generation, it does not depend on a PLL, resulting in a very good performance. For the GFM, all the references are tracked without any fluctuations.

5.2.3 Test 3 - Type-3 WT - wind speed step up for different Inertia constants in a weaker grid with $SCR < 5$

This test is similar to Test 2 but with an even lower SCR value close to zero. Here in Figures 44, 45, we see that the fluctuations in active power output and DC link voltage become even higher in the case of the GFL control. The GFM control performs very well even with such a weak grid.

5.2.4 Test 4 - Type-3 WT - sudden load step up for different Inertia constants in a strong grid with $SCR > 10$

Active power and frequency were observed for a sudden load step-up for both GFM and GFL strategies. Figures 46 and 47 show plots for different values of inertia constants.

As shown in Figures 46, 47, The active power response of the GFM strategy clearly shows the inertial support similar to that of conventional synchronous generators. Such an active power-supporting behavior is absent in the case of the GFL. The same inertial behavior can be seen in the frequency plot as well. It is worth noting that the frequency nadir improves with a higher inertia value.

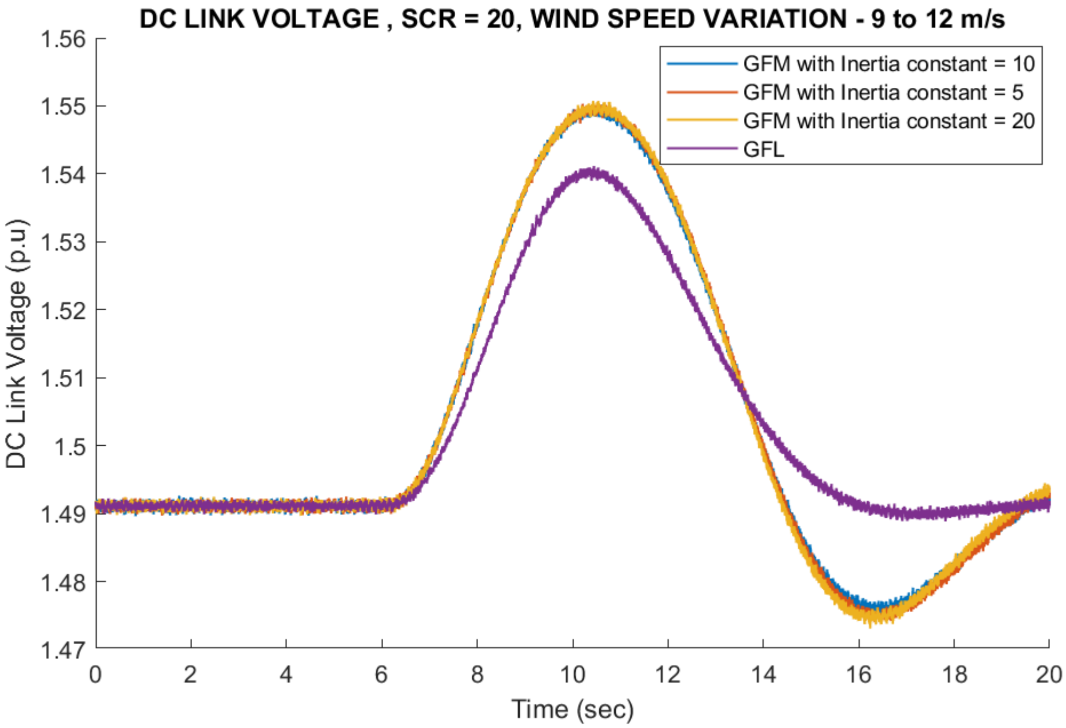

Figure 40: DC-link voltage variation in GFM (Inertia constant values 10, 20 and 5) and GFL Type-3 WT for wind speed step up at $SCR > 10$ (Test no. 1).

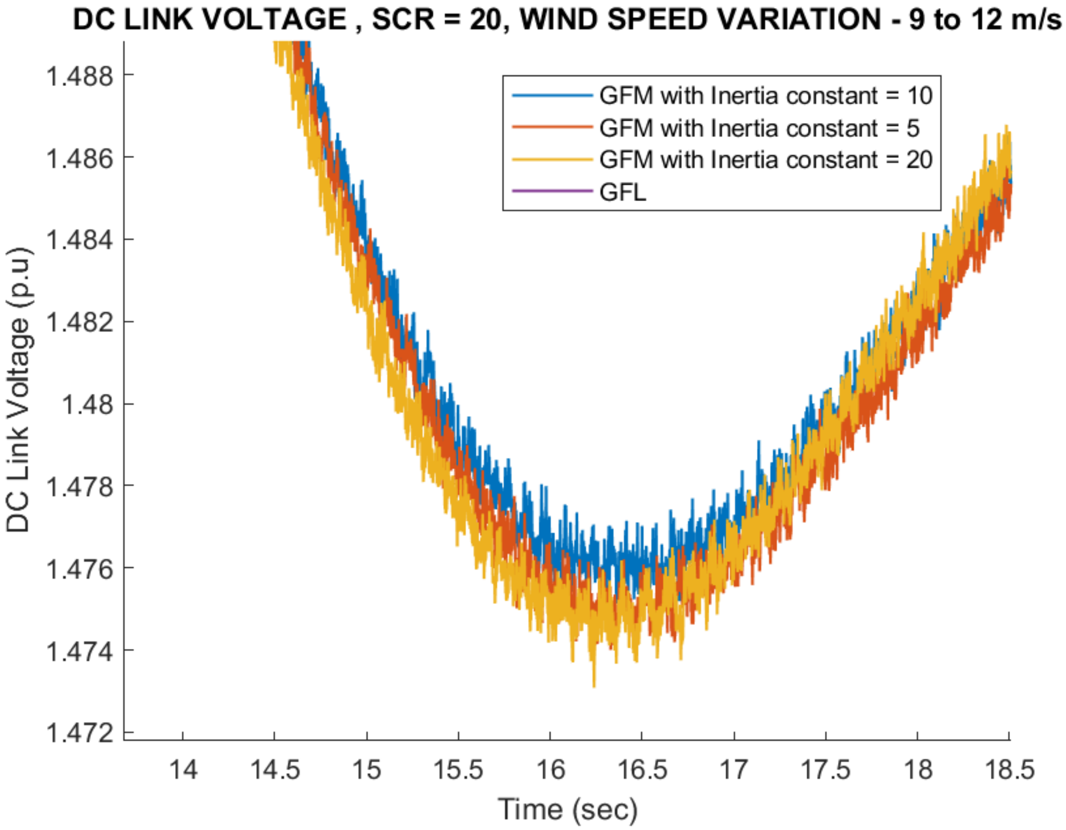

Figure 41: Zoomed DC link voltage minima in GFM (Inertia constant values 10,20 and 5) and GFL Type-3 WT for wind speed step up at $SCR > 10$ (Test no. 1).

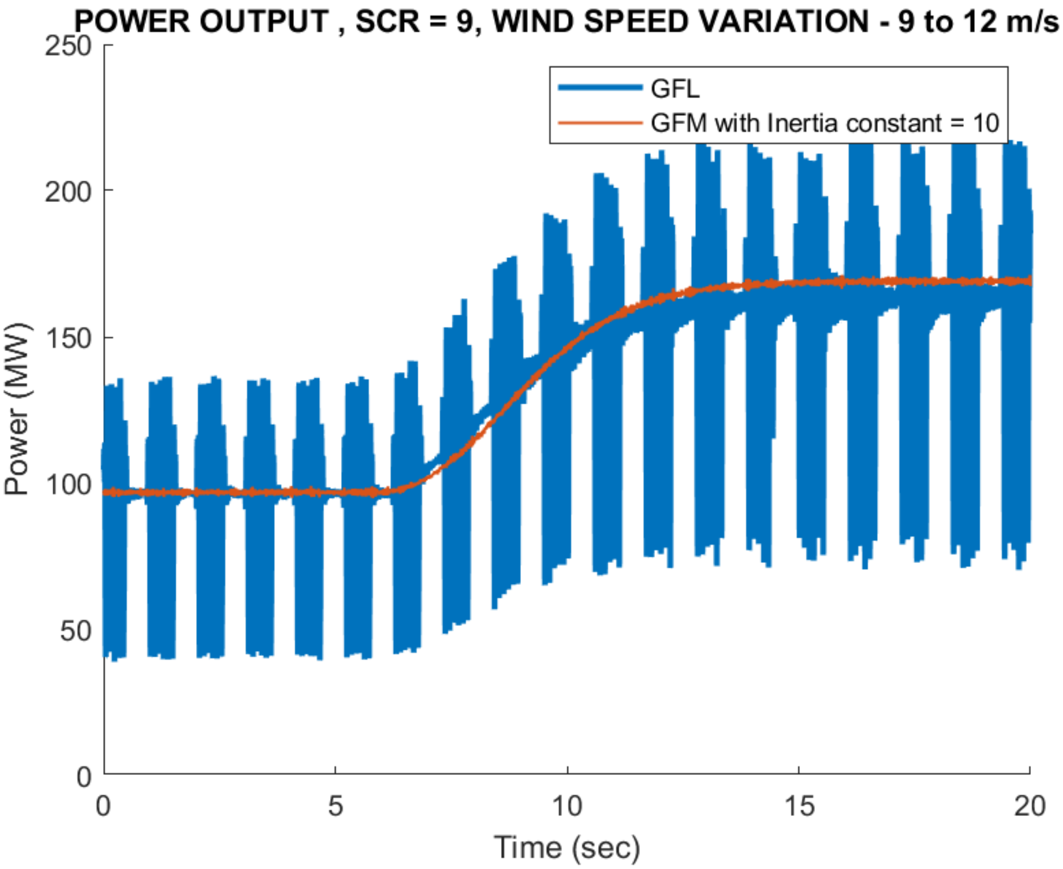

Figure 42: Active power step up in GFM (Inertia constant value 10) and GFL Type-3 WT for wind speed step up at $SCR = 9$ (Test no. 2).

5.2.5 Test 5 - Type-3 WT - single phase fault generation at low SCR grid ($SCR = 9$)

Single phase to ground fault was generated for both GFM and GFL modes of operation to observe the response of rotor currents, crowbar protection action and DC link voltage, and DC chopper protection action response. Also, the frequency response was observed. The plots can be seen in the Figures 48, 49, 50, 51, 52. As shown in Figures 48 and 49, the DC chopper protection action was not observed for both GFM and GFL control operations. The more interesting result is for the rotor currents and the crowbar protection action. We can observe in Figures 50 and 51 below that for the GFL control, the crowbar protection control gets actuated as the rotor currents breach the 2 kA limit. Such is not the case for GFM; in that case, the rotor currents remain below this threshold limit. The frequency response in Figure 52 clearly shows inertial behavior in the case of GFM operation. Since the GFM strategy contains an active power loop which incorporates a Power - frequency droop relationship along with virtual inertia element, the GFM strategy provides grid support by supplying or removing active power whenever the active power falls short or becomes excess respectively. What we see in figure 52 is this droop relationship and virtual inertia in action which ensures an active power support to the grid i.e as active power supply goes up - frequency drops, and as active power supply goes down - frequency shoots up (as in our case of Fig. 52) and due to inertia, it takes more time to trace back to reference and meanwhile ensures active power support.

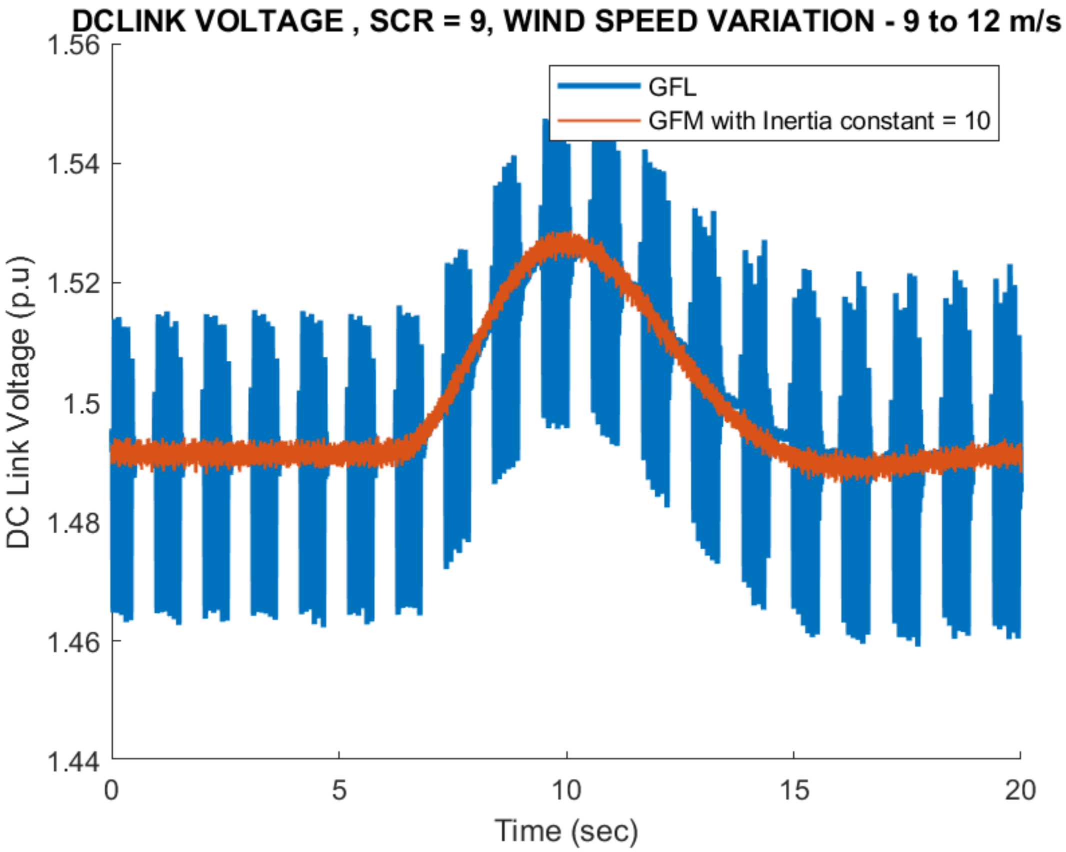

Figure 43: DC-link voltage variation in GFM (Inertia constant value 10) and GFL Type-3 WT for wind speed step up at $SCR = 9$ (Test no. 2).

5.2.6 Test 6 - Type-3 WT - double phase fault generation at low SCR grid ($SCR = 9$)

The two-phase to ground fault is generated, and the rotor currents and crowbar action are observed. Figures 53, 54 below show the observed parameters for GFM and GFL, respectively.
It should be noted that the crowbar action also happens for the GFM, as was not the case for single-phase faults. Also, on close observation, we see that the crowbar action is slightly larger for the GFL strategy. Hence, again the GFM strategy performs better.

5.2.7 Test 7 - Type-3 WT - three-phase fault generation at low SCR (HVDC link connected) ($SCR = 9$)

Here is observed the response of the Type-3 WT for a three-phase fault generated at a low SCR. The rotor currents and crowbar action for GFM and GFL strategies can be observed in Figures 55, 56.
Here, we observe that the 2 kA breach for the GFM strategy is lesser than for GFL, and hence the crowbar action is again more for GFLs. An interesting observation can be made here that the frequency synchronization occurs with a delay. A similar observation is also made in Test no. 9 and the reason will be explained under the heading of that test. With lesser breach observed for the GFM case, it can be said that it is performing better than the GFL control.

5.2.8 Test 8 - Type-3 WT - double phase fault at very low SCR grid (HVDC link connected) ($SCR < 5$)

Here again, we observe the response of the Type-3 WT for double-phase fault generation for a very weak grid with SCR levels below 5. The rotor currents and crowbar action can be observed for both GFM and GFL cases in Figures 57, 58.
Here, contrary to the previous observations, there is no significant difference between the crowbar action for the two control strategies. One can see that the crowbar action for the GFL strategy occurs more rapidly as compared to the GFM case.

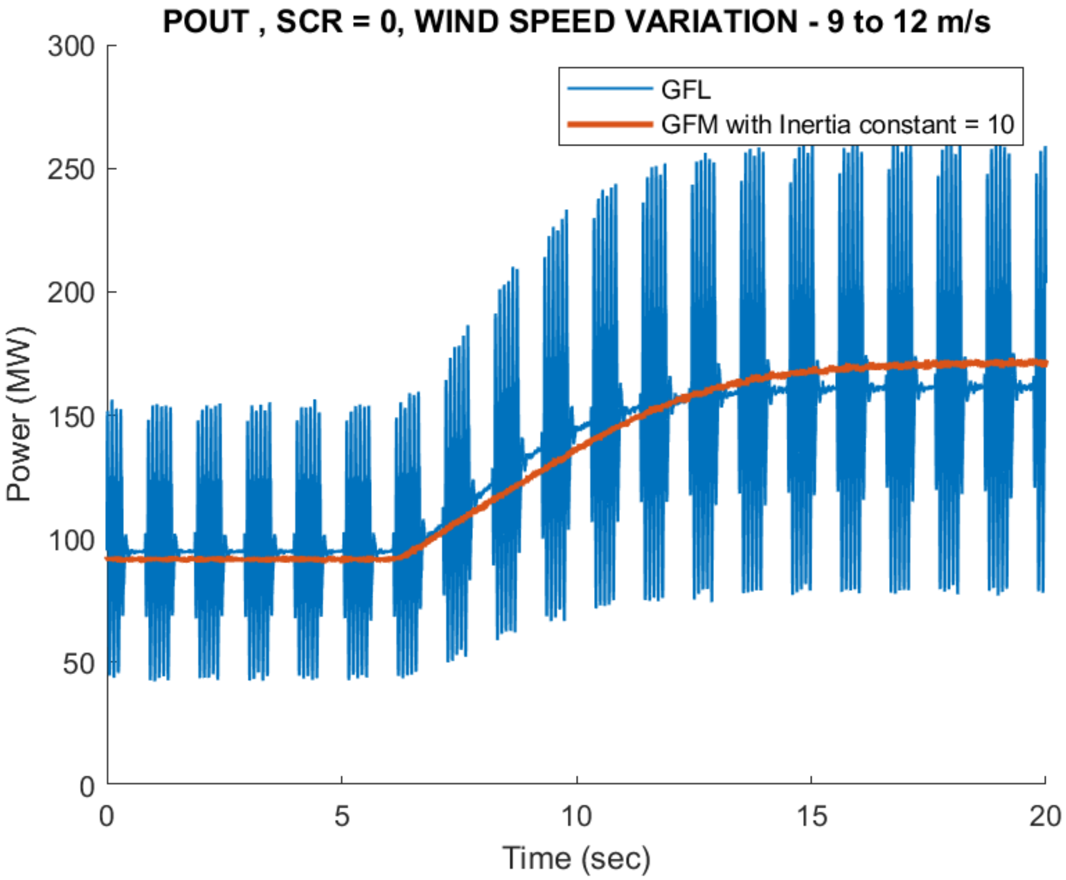

Figure 44: Active Power response in GFM (Inertia constant value 10) and GFL Type-3 WT for wind speed step up at $SCR < 5$ (Test no. 3).

5.2.9 Test 9 - Type-3 WT - three-phase fault generation at very low SCR (HVDC link connected) ($SCR < 5$)

Finally, we observe the response of the Type-3 WT for three-phase fault generation at very weak grid conditions. The rotor currents and crowbar protection action for both GFM and GFL cases can be observed in Figures 59, 60.
A significant difference in the crowbar action between the two control strategies is observed here. The 2 kA breach happens on two instances for the GFL strategy but there is no breach observed for the GFMs. Similar to the results obtained for Test no. 7, we can also see here that the frequency synchronization comes with a delay. The reason for this is again the inertia associated with the active power loop which results in a delayed synchronization. This inertia, as we observed previously in Test no. 4, is responsible for active power support to the grid.

5.2.10 Test 10 - Type-4 WT - sudden load step-up test at $SCR = 9$

As was done for the Type-3 WT, in this test, the active power output and frequency response was observed for both GFM and GFL modes for Type-4 WT of operation for a sudden load step-up. The plots can be seen in Figure 61.
For the GFM strategy plots in Figure 61 where for both the inertia values, the controller traces back the reference value after the load step. We see that for the GFL mode, the controller does not show active power support for the grid and goes out of control after the load step for a weak grid. In the frequency response seen in Figure 62, the inertial behavior can be clearly seen for the GFM mode. The frequency nadir improves with a higher inertia value.
It can be clearly concluded that for a weak grid with a high penetration of renewable energy sources, the GFM strategy is the way to go as it provides better controller performance in terms of power quality and stability.

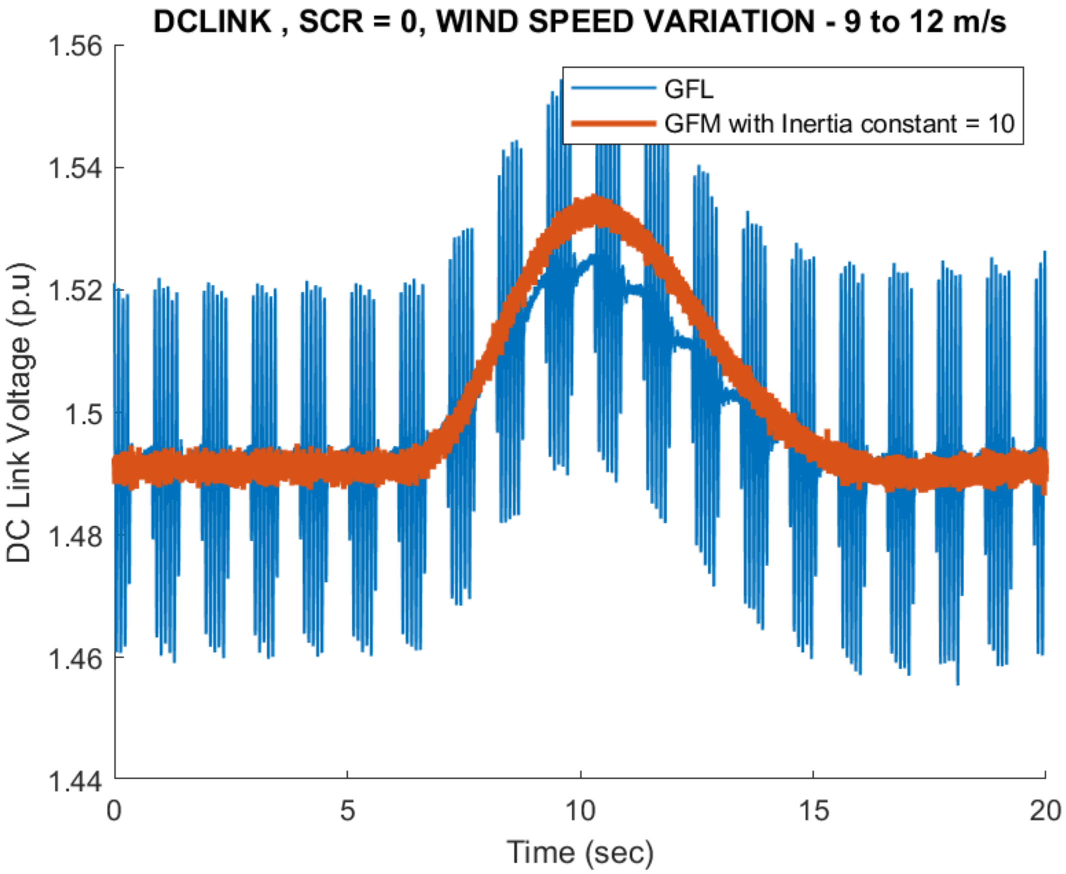

Figure 45: DC-link voltage variation in GFM (Inertia constant value 10) and GFL Type-3 WT for wind speed step up at $SCR < 5$ (Test no. 3).

In the next section, the detailed process of developing the GFM controller as a black-box model which will be capable of running in real-time is presented.

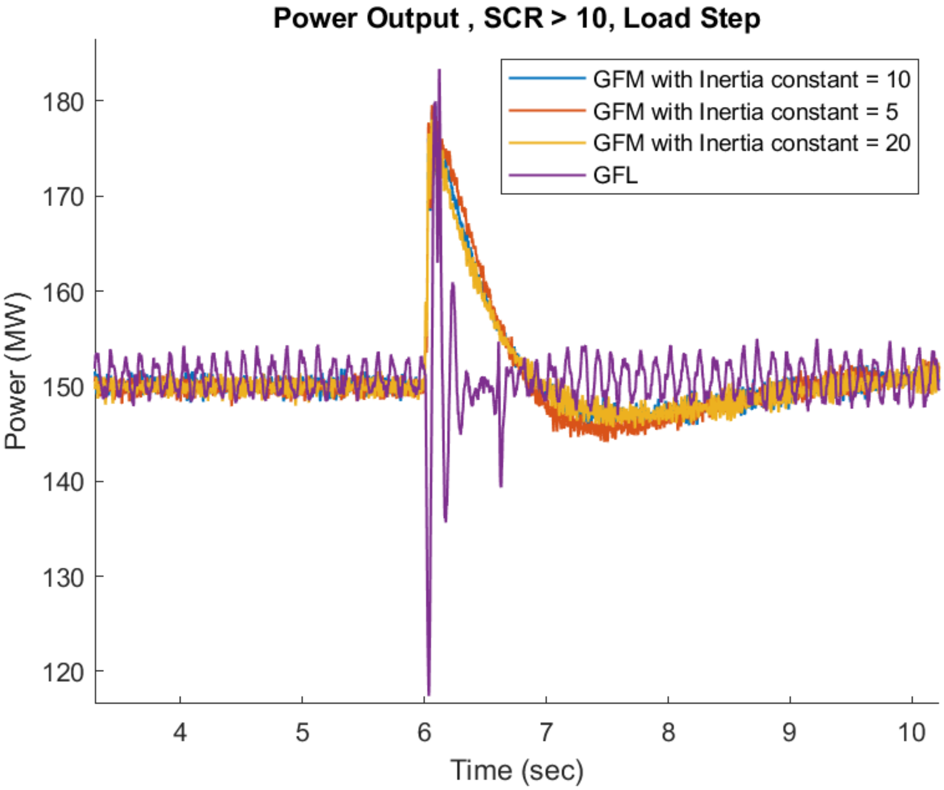

Figure 46: Active power response in GFL and GFM Type-3 WT model for different inertia values for sudden load step up with $SCR > 10$ (Test no. 4).

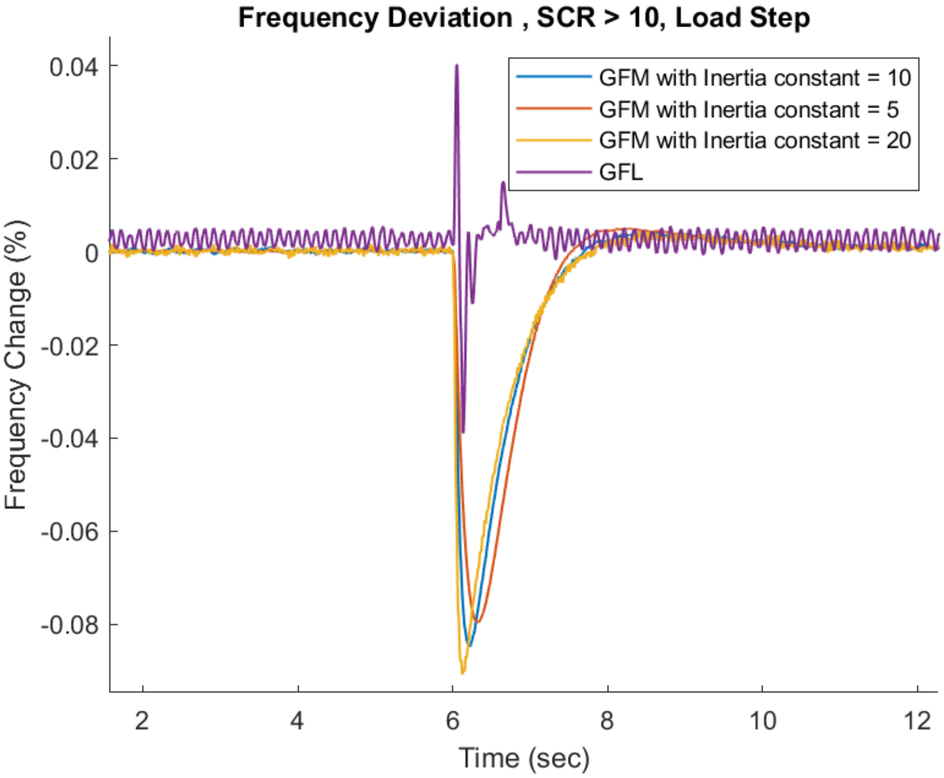

Figure 47: Frequency variation in GFL and GFM Type-3 WT model for different inertia values for sudden load step up with $SCR > 10$ (Test no. 4).

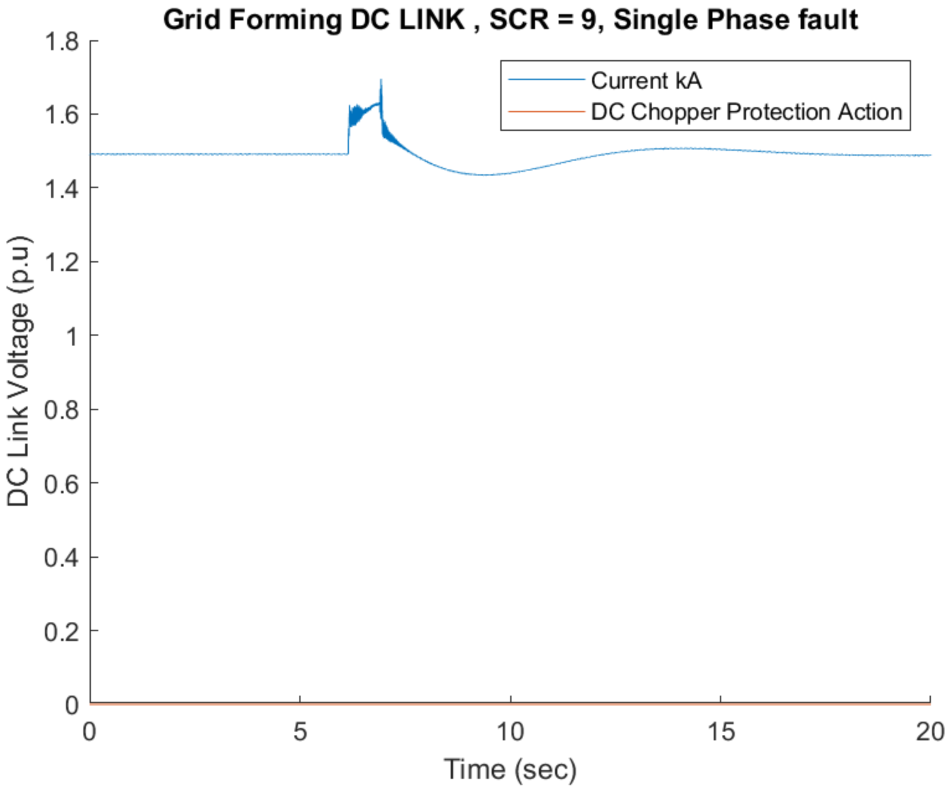

Figure 48: GFM mode - DC link voltage response in Type-3 WT model for single phase to ground fault generation at $SCR = 9$ (Test no. 5).

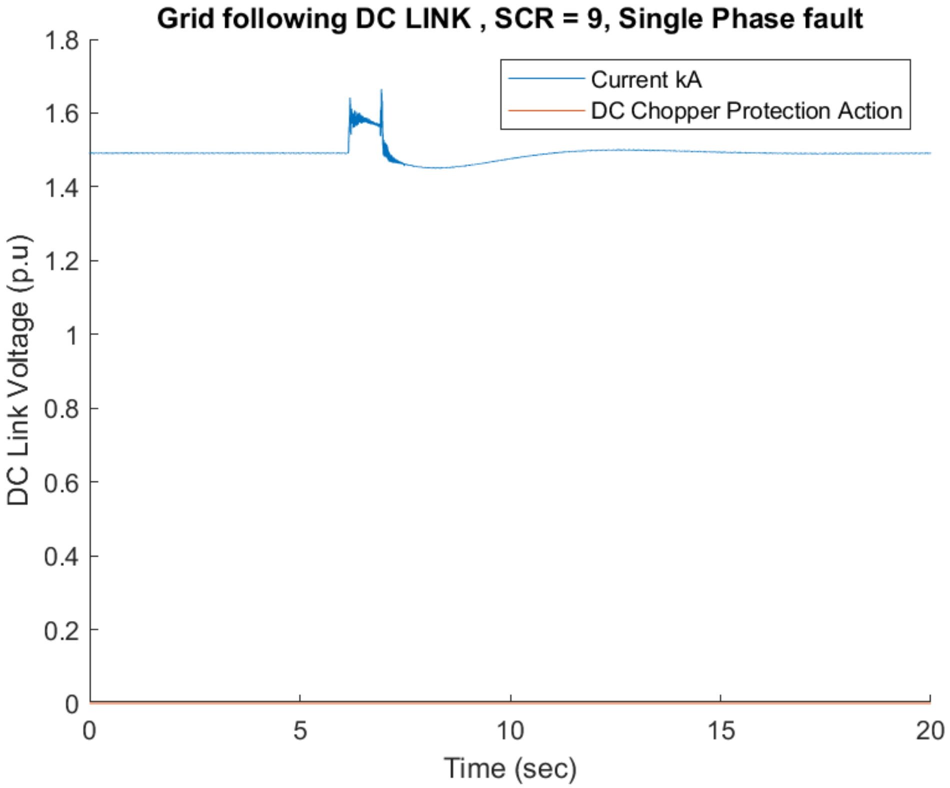

Figure 49: GFL mode - DC link voltage response in Type-3 WT model for single phase to ground fault generation at $SCR = 9$ (Test no. 5).

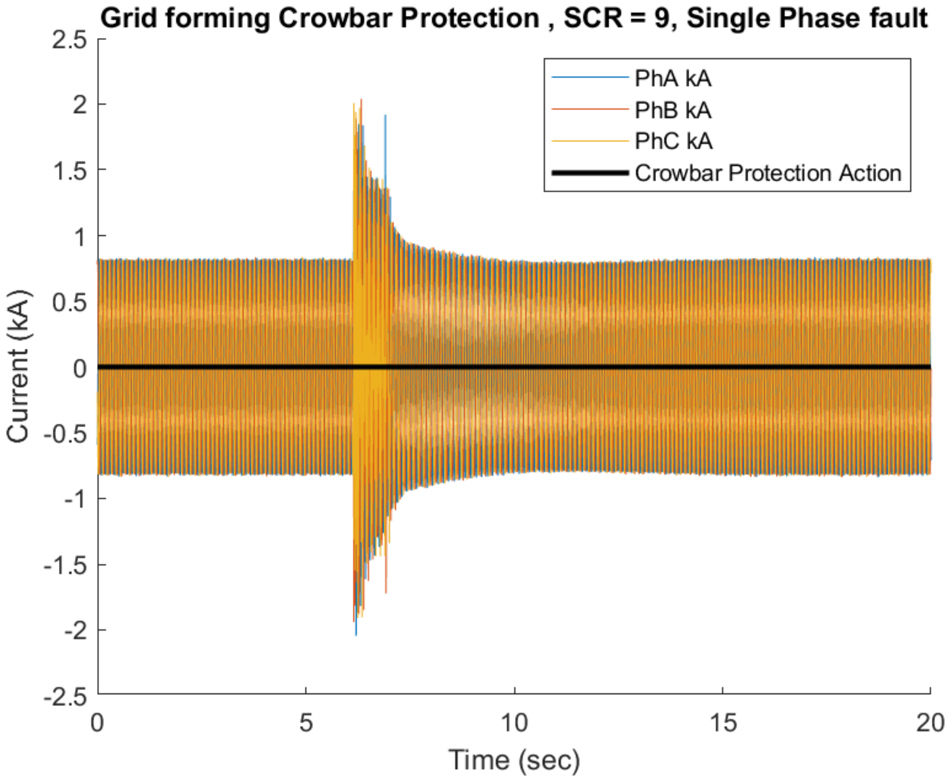

Figure 50: GFM mode - rotor currents and crowbar protection response in Type-3 WT model for single phase to ground fault generation at $SCR = 9$ (Test no. 5).

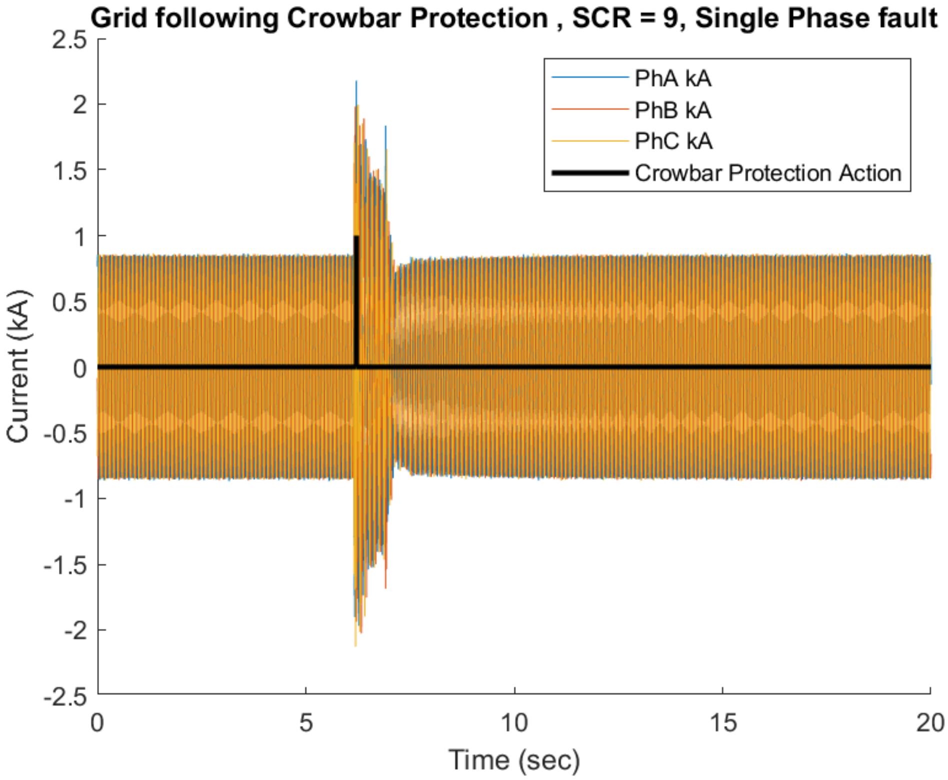

Figure 51: GFL mode - rotor currents and crowbar protection response in Type-3 WT model for single phase to ground fault generation at $SCR = 9$ (Test no. 5).

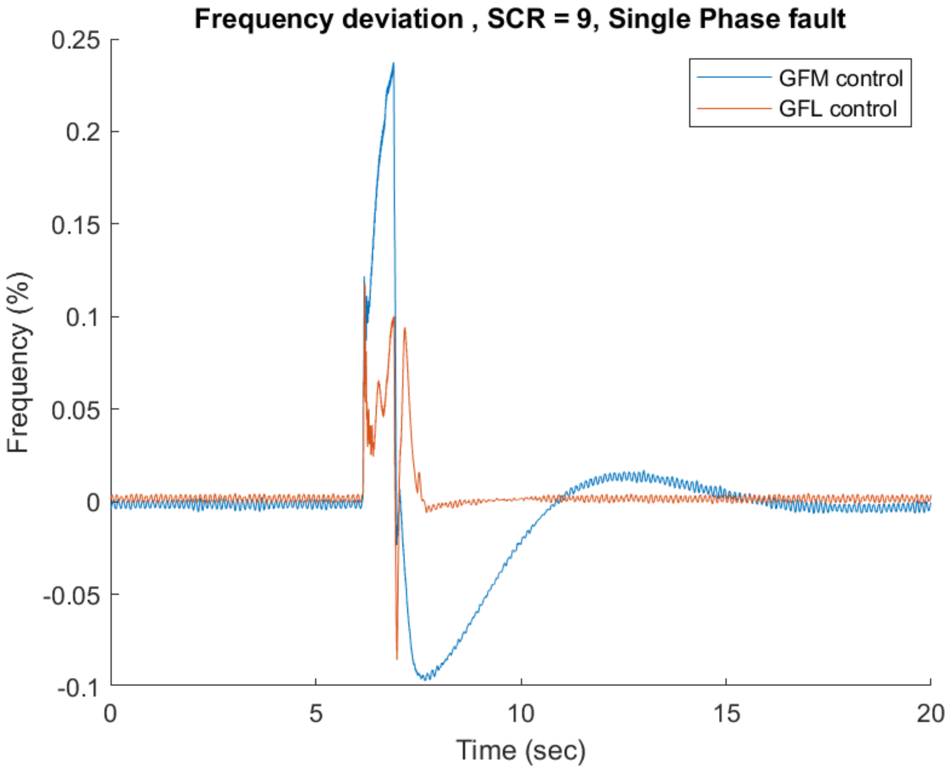

Figure 52: Frequency variation in GFM and GFL Type-3 WT model for single phase to ground fault generation at $SCR = 9$ (Test no. 5).

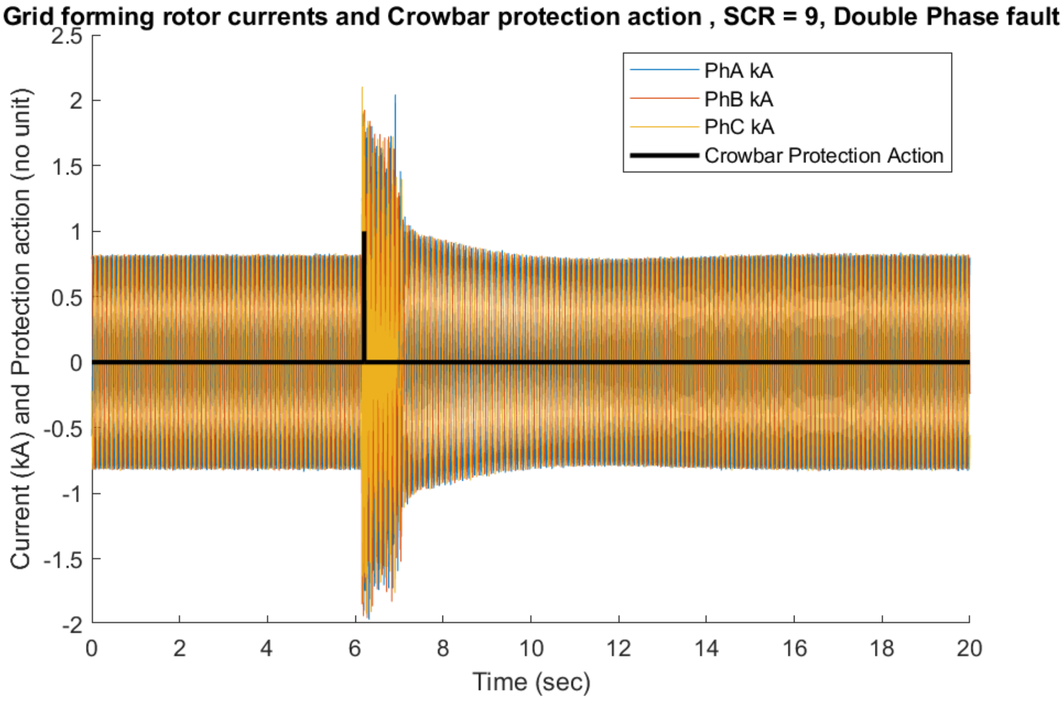

Figure 53: Rotor currents and crowbar action for GFM Type-3 model for a two-phase to ground fault for $SCR = 9$ (Test no. 6).

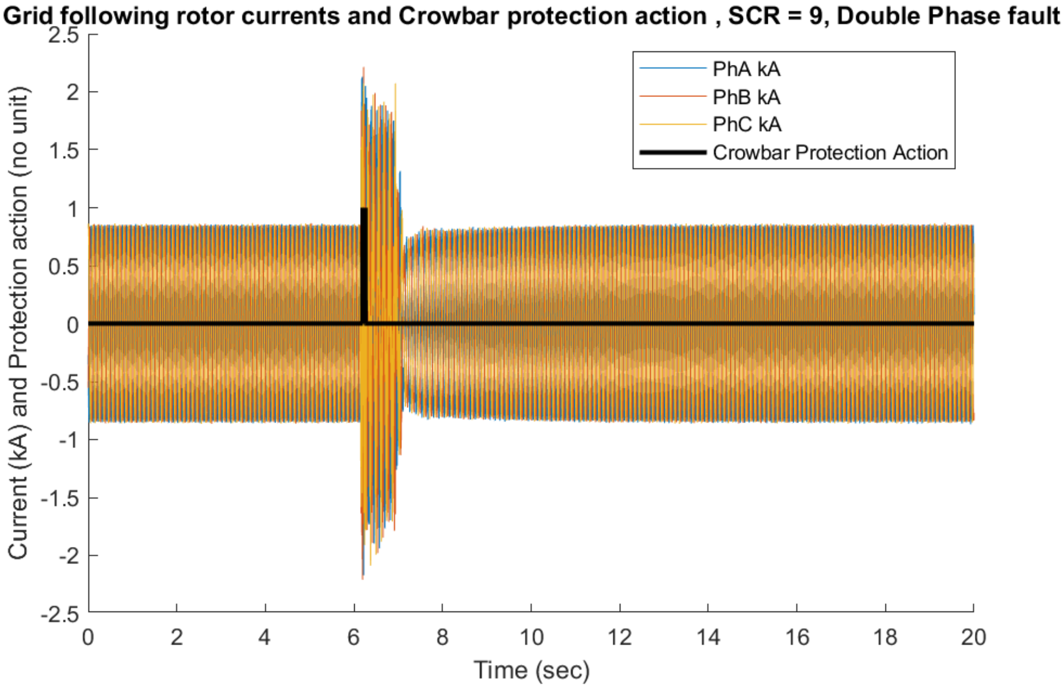

Figure 54: Rotor currents and crowbar action for GFL Type-3 model for a Two-phase to ground fault for $SCR = 9$ (Test no. 6).

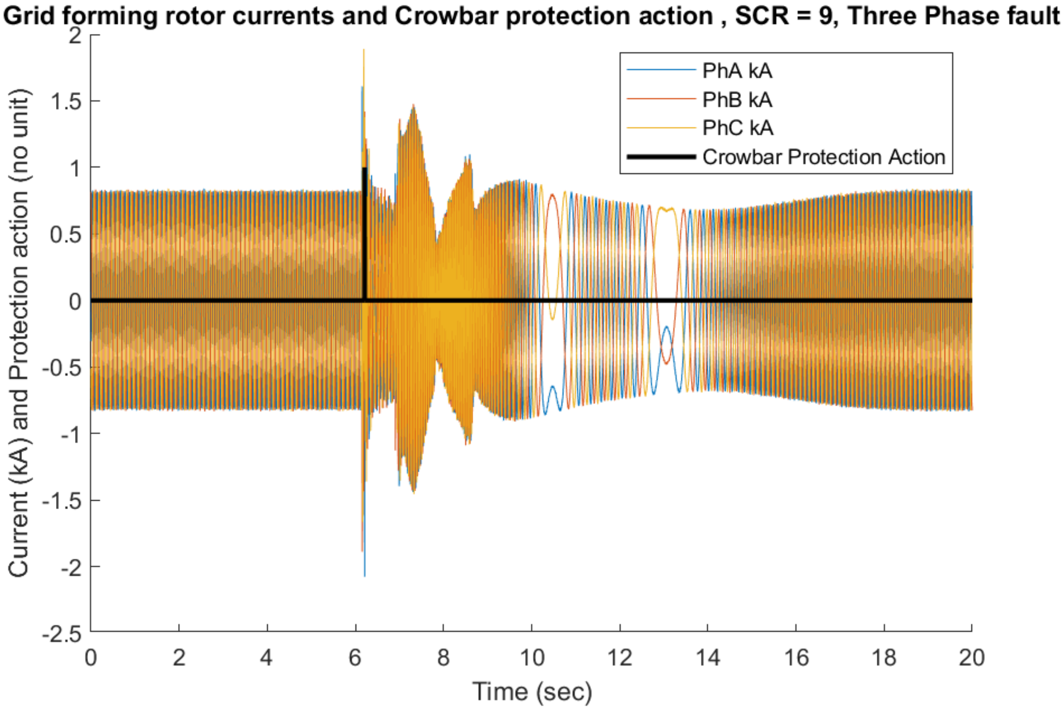

Figure 55: Rotor currents and crowbar action for GFM Type-3 model for a three-phase to ground fault for $SCR = 9$ (Test no. 7).

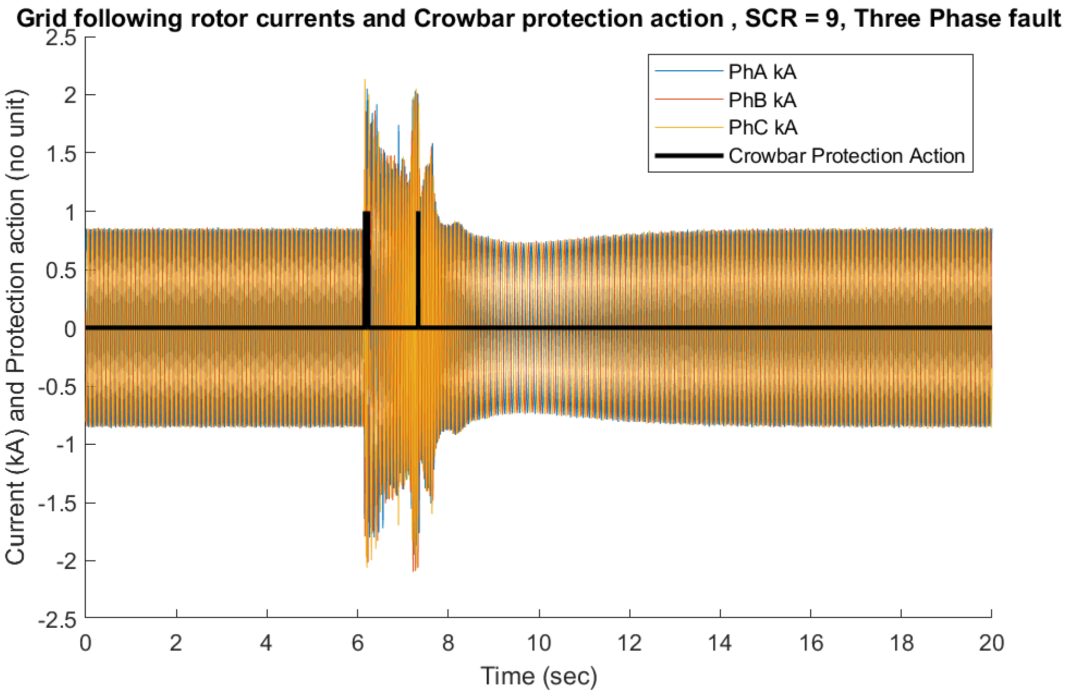

Figure 56: Rotor currents and crowbar action for GFL Type-3 model for a three-phase to ground fault for $SCR = 9$ (Test no. 7).

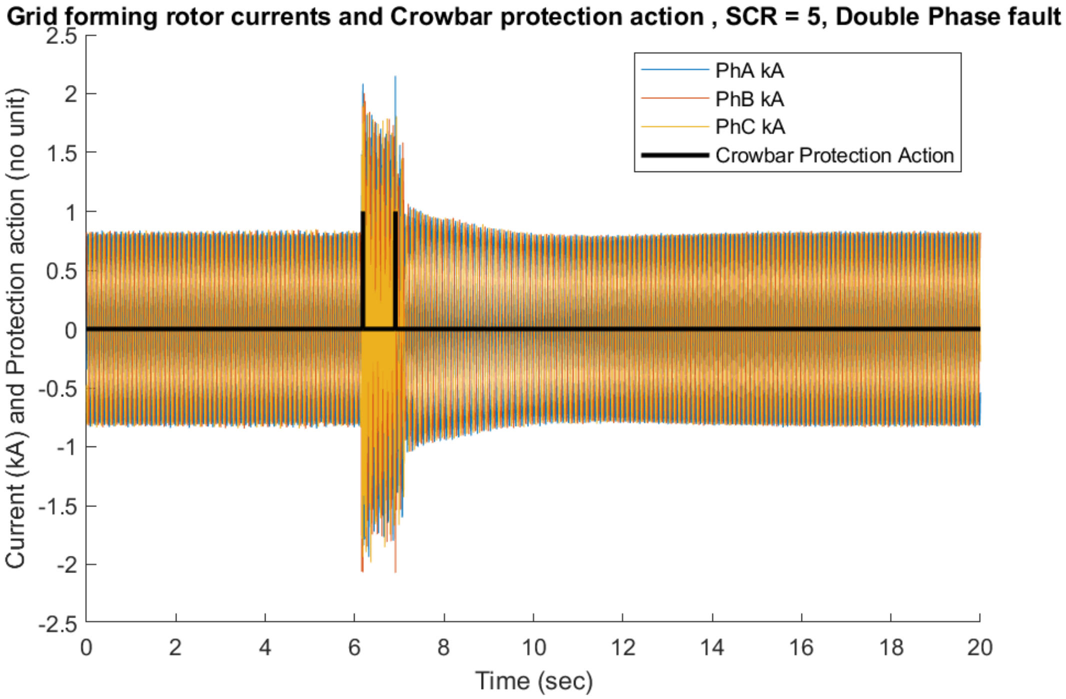

Figure 57: Rotor currents and Crowbar action for GFM Type-3 model for a double phase to ground fault at $SCR = 5$ (Test no. 8).

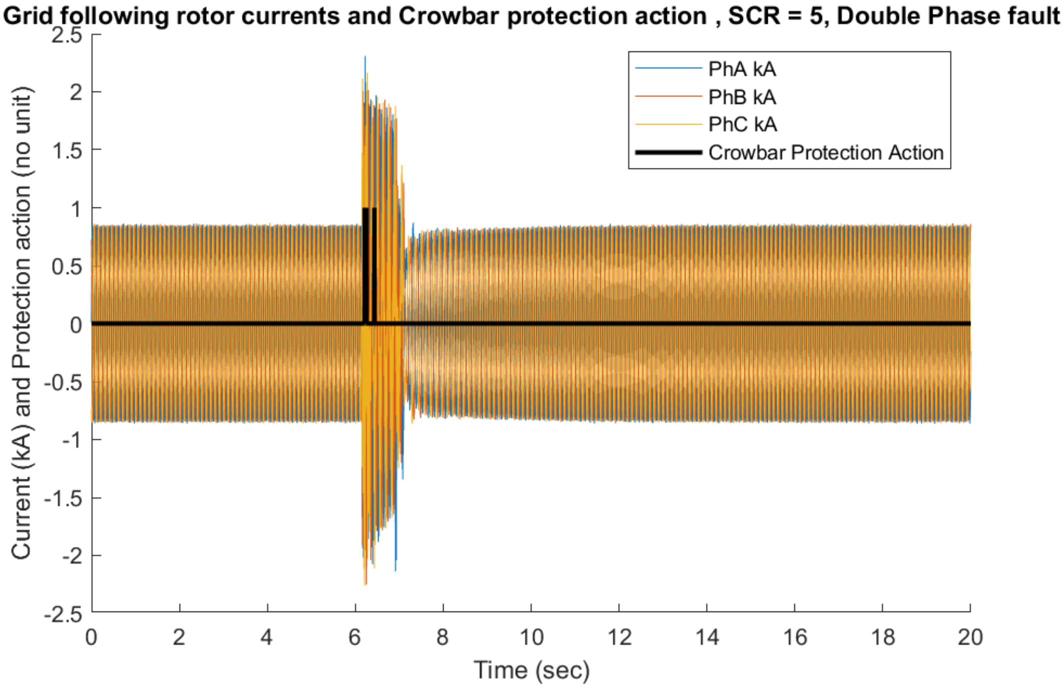

Figure 58: Rotor currents and crowbar action for GFL Type-3 model for a double phase to ground fault for $SCR = 5$ (Test no. 8).

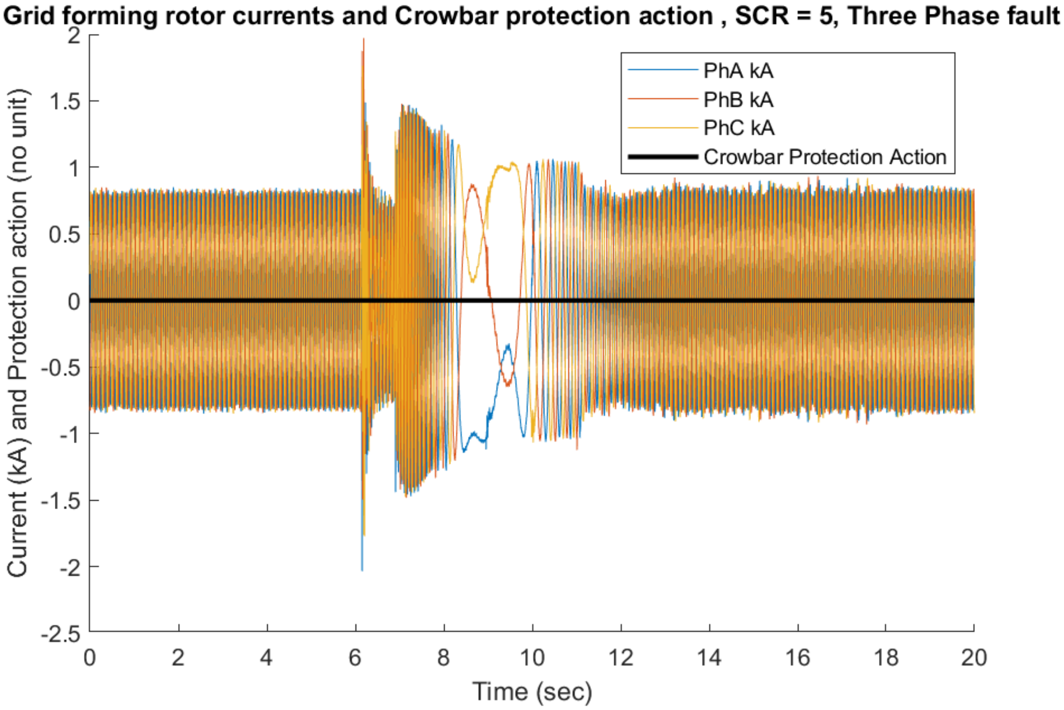

Figure 59: Rotor currents and Crowbar action for GFM Type-3 model for a three-phase to ground fault at $SCR < 5$ (Test no. 9).

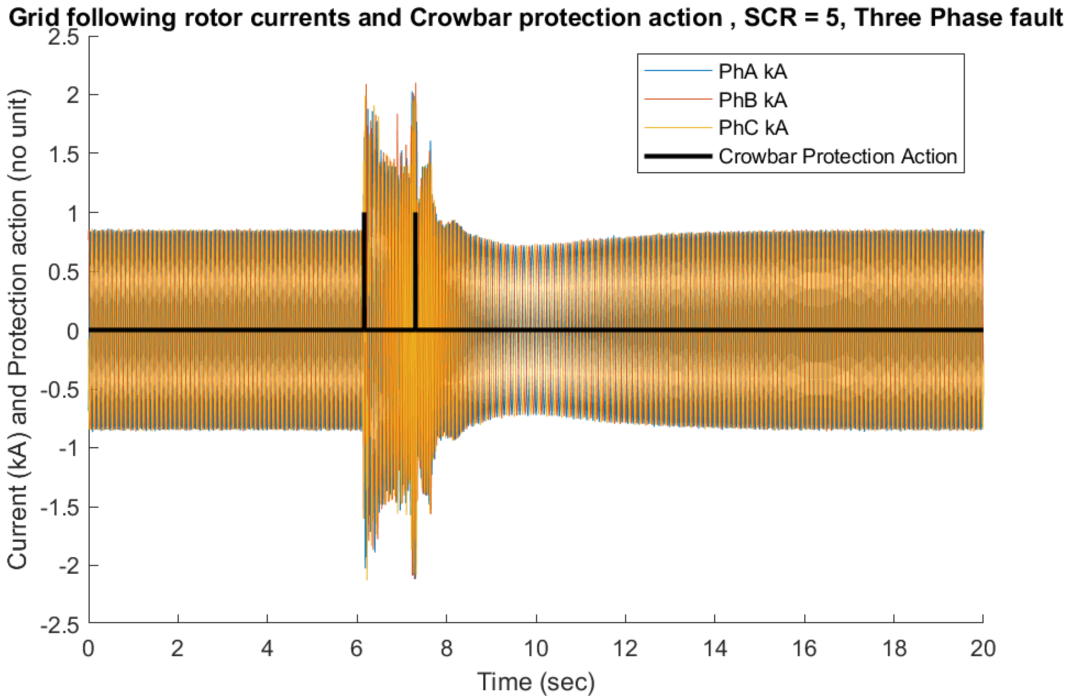

Figure 60: Rotor currents and Crowbar action for GFL Type-3 model for a three-phase to ground fault at $SCR < 5$ (Test no. 9).

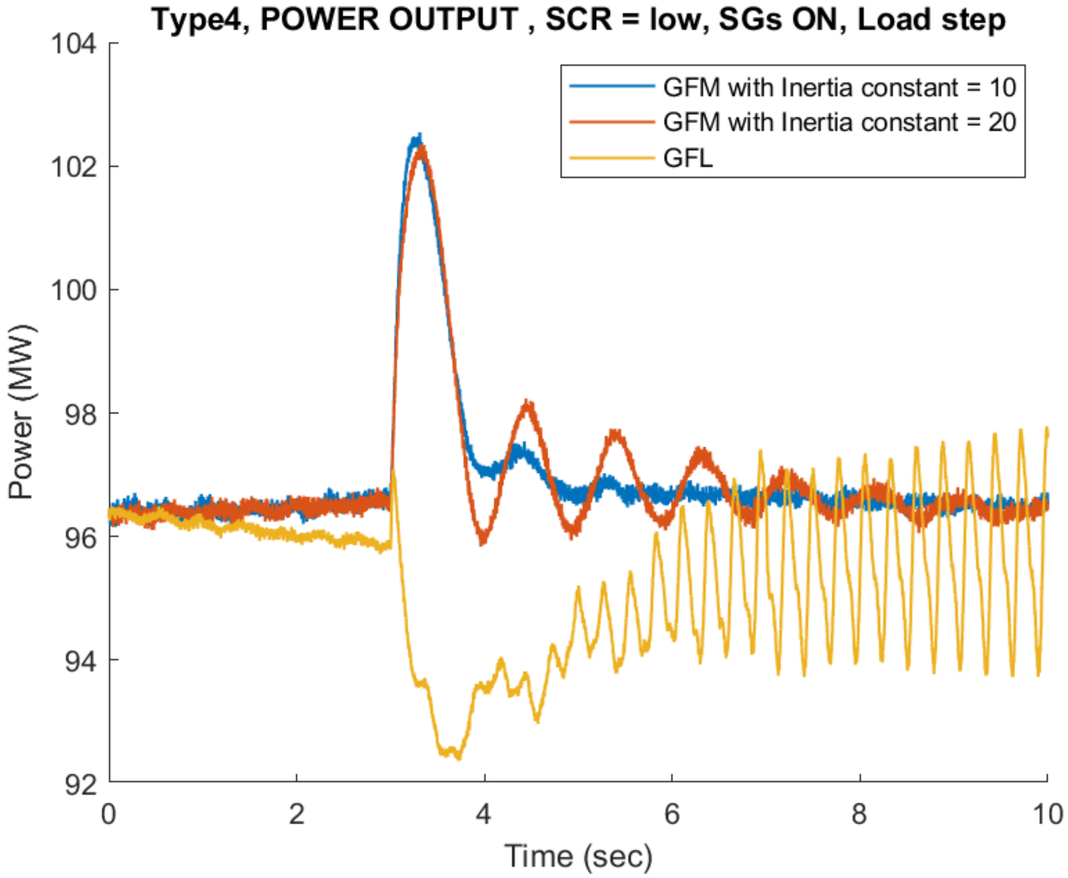

Figure 61: Active power response in GFM control (with different Inertia constant values - 10, 20 and 5) and GFL control Type-4 WT for sudden load step up test at $SCR = 9$ (Test no. 10).

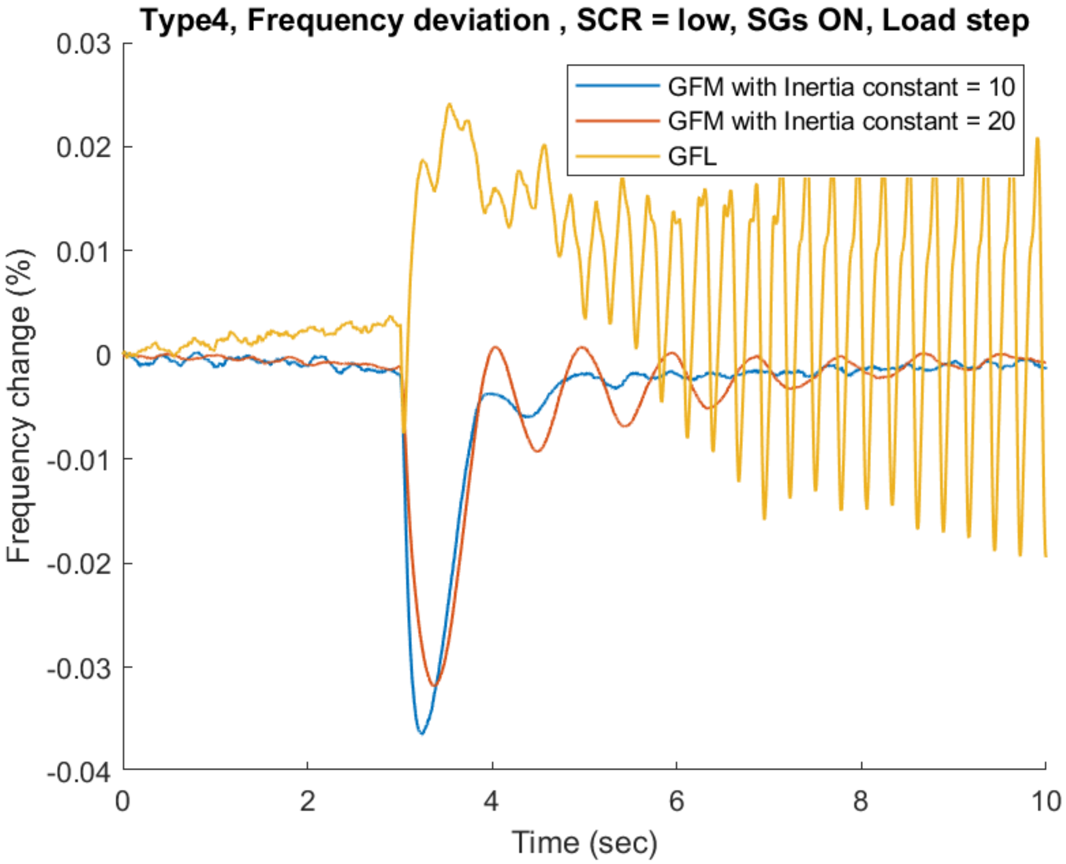

Figure 62: Frequency variation in GFM control (with different Inertia constant values - 10, 20 and 5) and GFL control Type-4 WT for sudden load step up test at $SCR = 9$ (Test no. 10).

6 GFM as Black Box Model

This section presents step-by-step process of developing the GFM controller initially built on RSCAD FX into a black box capable of running in real time. First, the motivation behind taking up this task is given. This is followed by the details of the methodology followed for developing the black box model. Then the details of developing the software-in-the-Loop (SIL) setup will be discussed. Finally, details on the tests done and results obtained with the SIL setup will be presented and discussed, and a comparison with the results obtained previously will be made to establish the validity of the black box controller.

6.1 Black box development

The main advantage of having a black box model is the time saving and ease of plug-and-play with power system models developed in various modeling software like PSCAD, Powerfactory, RSCAD, Hypersim, etc. When a black box controller model exists, it can easily be used to show the functioning and validity of the controller algorithm without losing intellectual property. A black box model greatly improves interoperability and makes sharing the controller models with vendors and competitors easy.

6.2 Black box controller design

This subsection will discuss, in detail, the step-by-step methodology followed in developing the controller as a black box model.

6.2.1 Step-1: Building the GFM in MATLAB-Simulink

A black box model of a controller is a combination of an executable application (.exe/ .a/ .rtss) file along with a dynamically linked library (.lib/ .dll/ .rtdll). The executable is produced through an application code which is in C-programming language in our case. The application code calls the functions exported by the library file, which in turn requires the controller model's source code files (.c and .h files).
There is no in-built option for generating the source code files of an RSCAD model. Hence, an alternative strategy was followed. Generating source code files is possible with Simulink using the Code generation and Embedded Coder toolbox. Configure the code generator (see figure 64 below) to use the system target file ert_shrlib.tlc (see Figure 63), one can generate a source code package file of the model with all the necessary .c and header files. Code generation for that system target file exports:

1. Variables and signals of type ExportedGlobal as data.
2. Real-time model structure (model_M) as data.
3. Functions essential to executing your model code.

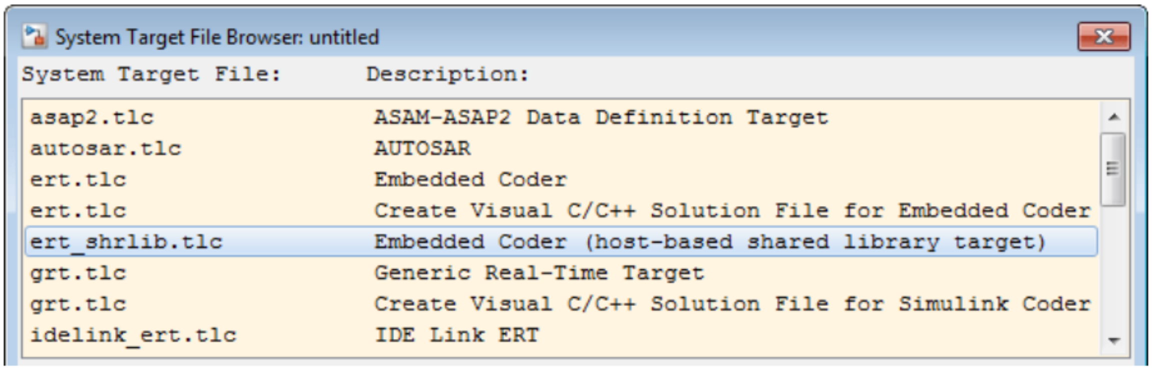

System Target File:	Description:
asap2.tlc	ASAM-ASAP2 Data Definition Target
autosar.tlc	AUTOSAR
ert.tlc	Embedded Coder
ert.tlc	Create Visual C/C++ Solution File for Embedded Coder
ert_shrlib.tlc	Embedded Coder (host-based shared library target)
grt.tlc	Generic Real-Time Target
grt.tlc	Create Visual C/C++ Solution File for Simulink Coder
idelink_ert.tlc	IDE Link ERT

Figure 63: Target file selection under model configuration.

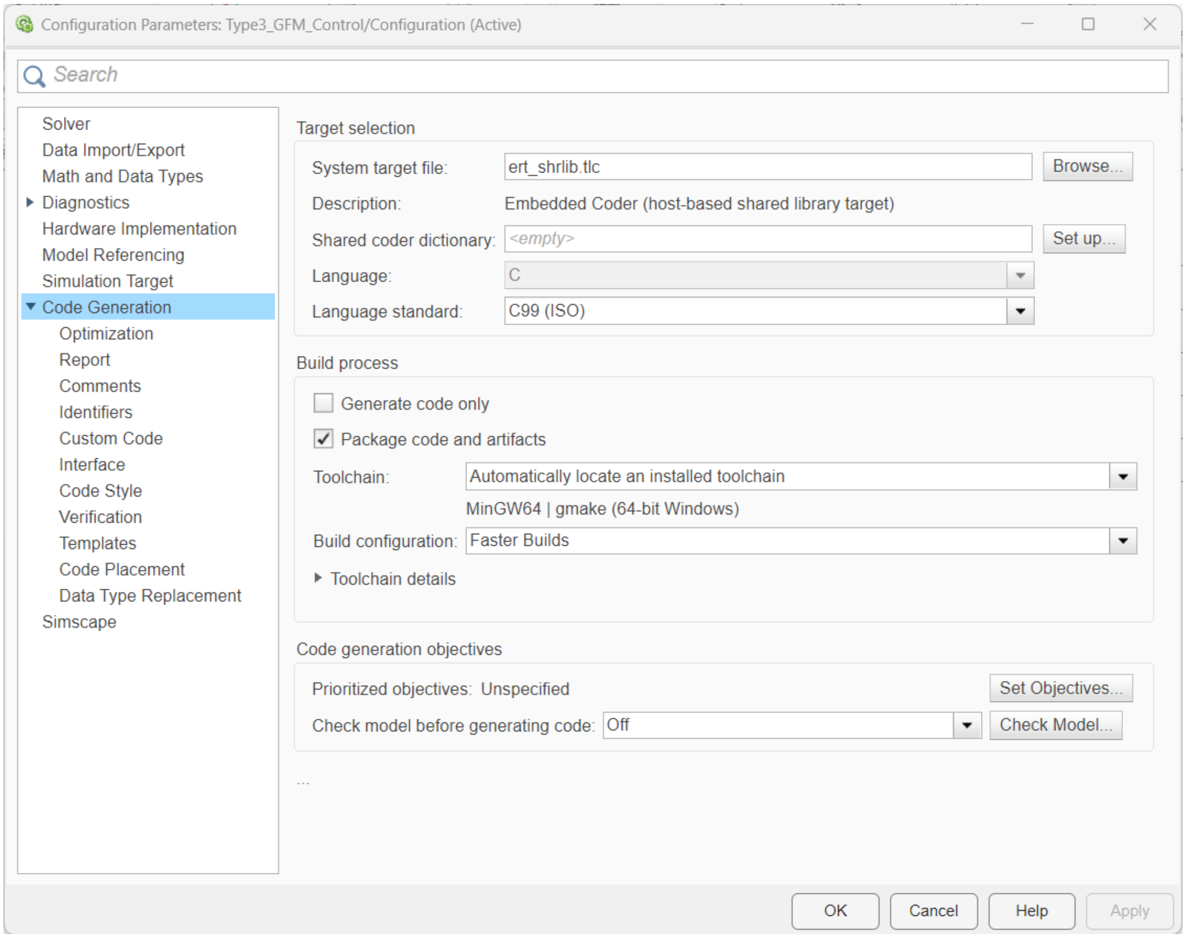

Configuration Parameters: Type3_GFM_Control/Configuration (Active)

Target selection

System target file: ert_shrlib.tlc

Description: Embedded Coder (host-based shared library target)

Shared coder dictionary: <empty>

Language: C

Language standard: C99 (ISO)

Build process

☐ Generate code only

☑ Package code and artifacts

Toolchain: Automatically locate an installed toolchain

MinGW64 | gmake (64-bit Windows)

Build configuration: Faster Builds

Code generation objectives

Prioritized objectives: Unspecified

Check model before generating code: Off

Figure 64: Model Configuration.

Hence the GFM part of the Type-3 WT model was built on Simulink. The mask of the Simulink model can be seen below in Figure 65.

It can be seen that there are 19 inputs to the Simulink model and 6 outputs from the Simulink model. These Input/Output signals will have to be communicated between the controller black box model and the RSCAD model through the suitable communication protocol details. The input and output signals were originally internal control signals in the RSCAD model.

Once the target file is configured and the constructed model built, the generated code files can be accessed in the directory where the model exists. The Table 4 below shows the generated modules for any Simulink model and their specific details. Once the target file is configured and the constructed model is, we can access the generated code files in the directory where the model exists. Table 4 below shows the generated modules for any Simulink model and their specific details.

.

6.2.2 Step-2: Building the real-time library and application file

A normal static or dynamic linked library file is a Windows-based file that does not support operation in real time. To make the real-time simulations possible, the Windows operating system (OS) has to be temporarily converted to a real-time OS (RTOS). This is done by a third-party software named Interval Zero. IntervalZero is an RTOS Platform that supports determinism or hard real-time on multi-core processors while co-resident with the Windows operating system. Two IntervalZero components are mainly required to achieve this:

1. **IntervalZero RTX64 Sofware Development Kit (SDK)**: comes with headers and libraries required for developing real-time applications and DLLs. Provides support for linking real-time functionality into Windows applications and Windows kernel. Integrates seamlessly with Microsoft Visual Studio. It provides two project templates for the Visual studio - RTX64 RTDLL for building real-time dynamic linked

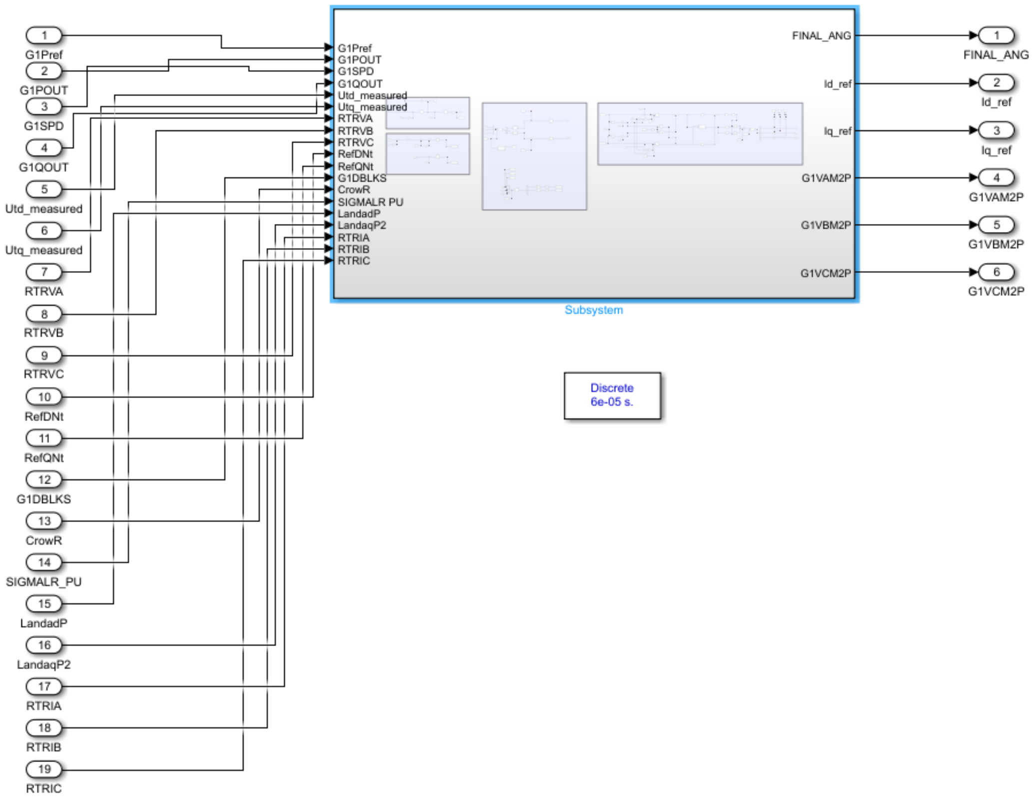

Figure 65: Controller model mask in Simulink.

Table 4: Generated code files by simulink embedded coder

File name	**Details**
1) model.c	contains entry point functions for all the code implemented in the algorithm.
2) model.h	declares model data structures and a public interface to the model entry points and data structures
3) ert_main.c	an example main that embedded code generates by default that shows how to call the generated code
4) model_types.h	provides forward type declarations for the model and its parameters
5) model_data.c	contains the declarations for the parameters, data structures and the constant block I/O data structure
6) rtwtypes.h	defines macros, data types and structures required by embedded coder
7) model_private.h	contains local macros and local data that are required by the model and subsystems

libraries and RTX64 Application for creating real-time applications (see Figure 66 below).

2. **IntervalZero RTX64 Runtime**: Adds a real-time subsystem (RTSS) to Windows that delivers hard real-time performance. It is deployed on your target system with your real-time application. Figure 67 below shows the overview of this process.

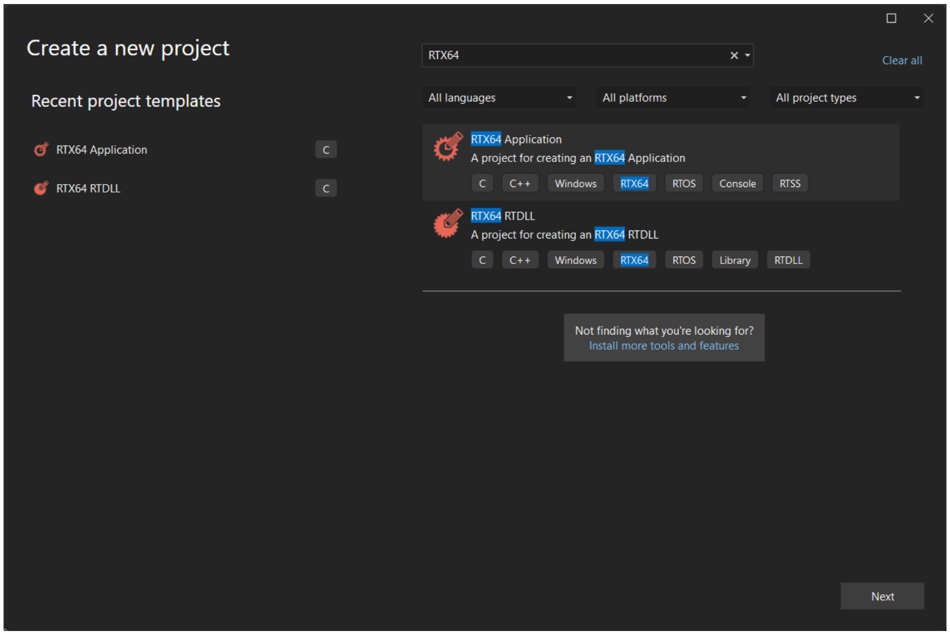

A project for creating an RTX64 Application

A project for creating an RTX64 RTDLL

Not finding what you're looking for?

Figure 66: RTX64 SDK templates in MS Visual Studio.

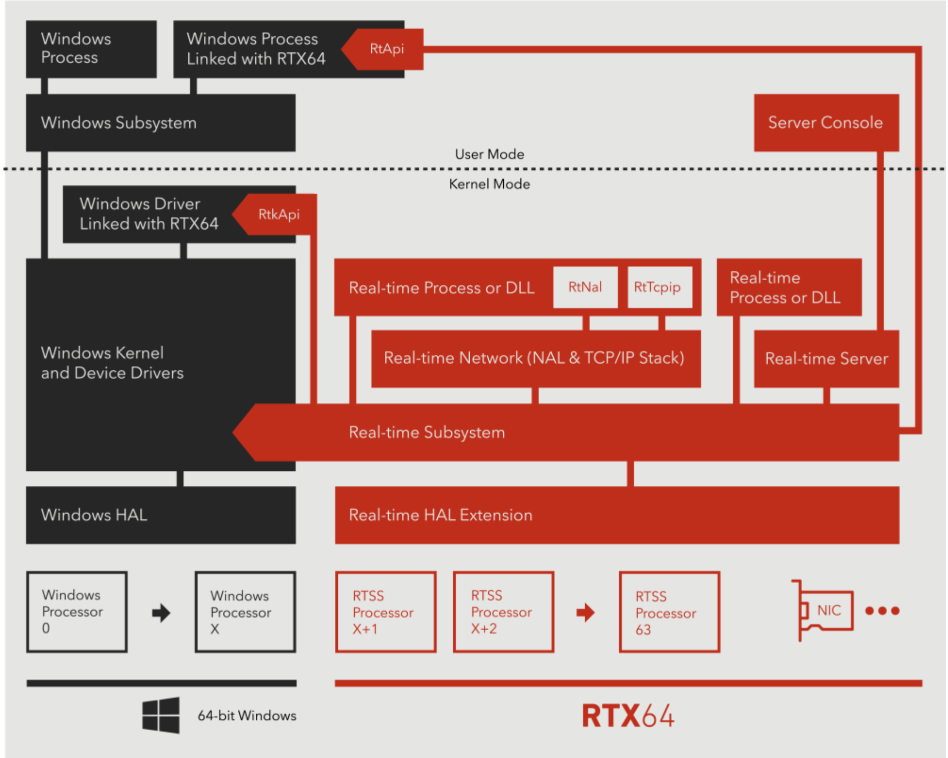

Figure 67: Interval zero operation, "IntervalZero products", 2021.

Using the RTX64 RTDLL template, we developed the library file. The steps to be followed are as follows:

1. Select the Real-time Dynamic-link Library (RTDLL) template from MS Visual Studio and then choose Next.
2. In the Configure your new project page, enter the project name. Leave the default Location and Solution name values. Set a Solution to Create a new solution. Uncheck Place solution and project in the same directory if it's checked. Create the project.

3. When the solution is created, you can see the generated project and source files in the Solution Explorer window in Visual Studio (see figure 68 below). Right now, this real-time DLL doesn't do very much. Next, you'll create and add the necessary header files to declare the functions your RTDLL exports, and then add the function definitions to the RTDLL to make it more useful.

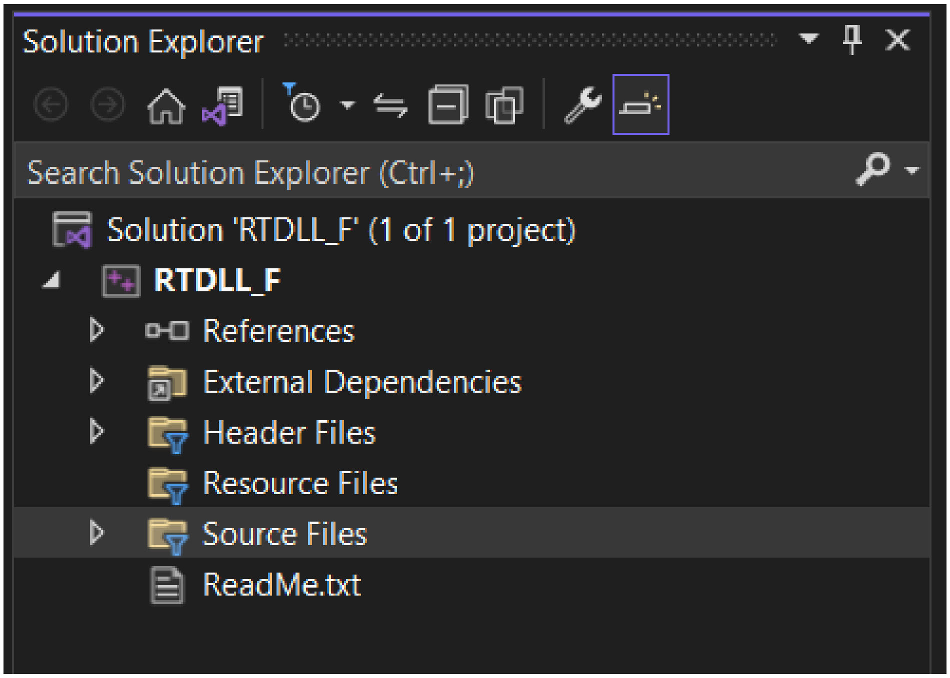

Figure 68: Solution explorer window.

4. The solution of the RTDLL template already contains a default header file. Now, declare the functions contained in controller source code (see figure 69 below), which includes necessary APIs and declares an example function. Remove the example function and add the function declarations contained in model.h file (seen earlier) to this skeletal header file. Then export the necessary functions and variables that you want to use in the application later.

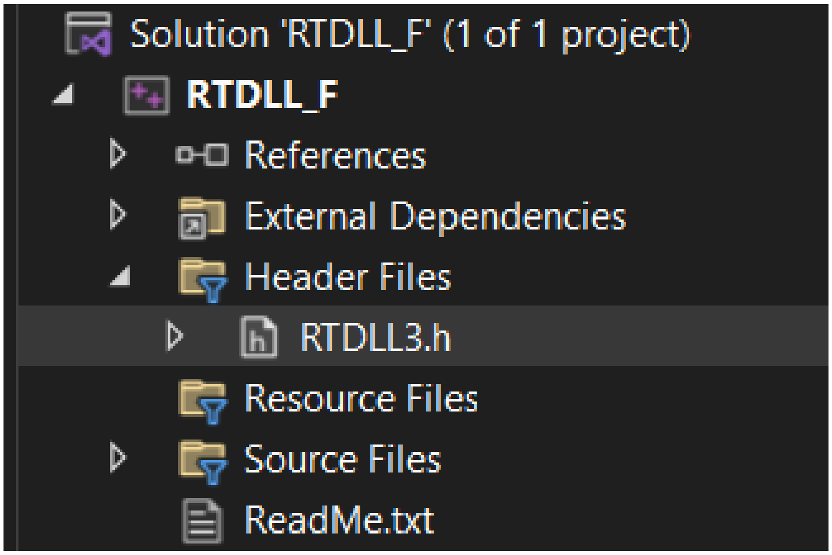

Figure 69: Header file.

5. Now, we must add implementations to our RTDLL by adding source files containing definitions of our

declared functions. The RTDLL template contains a skeletal source file in which the function definitions contained in the model.c file (seen earlier) will be added. Also, all the rest of .c files that were created in the source code package are to be added as source files here (see figure 70 below).

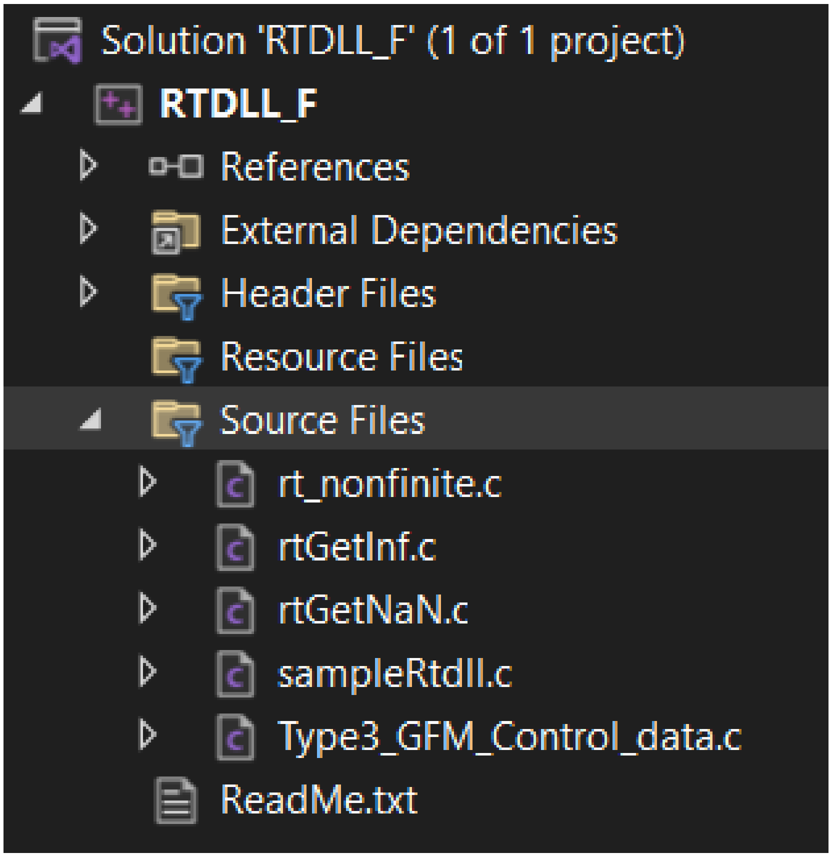
Solution 'RTDLL_F' (1 of 1 project)
RTDLL_F
References
External Dependencies
Header Files
Resource Files
Source Files
rt_nonfinite.c
rtGetInf.c
rtGetNaN.c
sampleRtdll.c
Type3_GFM_Control_data.c
ReadMe.txt

Figure 70: Source file.

6. The final step is to update the Windows SDK version of the template (see figure below) to the one in the current system to avoid build errors. Also, the source code header file's directories are to be added under 'Additional Include directories' (see Figure 71 below).
7. The final step is to build the code that generates the standard library file (.lib) and the real-time dynamic link library file (.rtdll) in the current directory, as shown in Figure 73 below.

Next, to build the communication between the developed library file and the RSCAD model, a wrapper code / application code needs to be built to generate an application that interacts with RTDS. Using the RTX64 Application template, we developed the wrapper code to generate the real-time application (.rtss) file finally. The steps to be followed are as follows:

1. Select the Real-time Application (RTSS) template from MS Visual Studio and then choose Next
2. In the Configure your new project page, enter the project name. Leave the default Location and Solution name values. Set a Solution to Create a new solution. Uncheck Place solution and project in the same directory if it's checked. Then choose Create to create the template project.
3. Next, to call the functions in your source code, your application project must include your library's header (.h) file (seen previously). You could copy this header file into your client app project, then add it to the project as an existing item. However, if you're working on the code for your DLL and your application code simultaneously, the header files could get out of sync. To avoid this issue, set the Additional Include Directories path in your project to include the path to the original header in the same way as was shown previously in Figure 72.

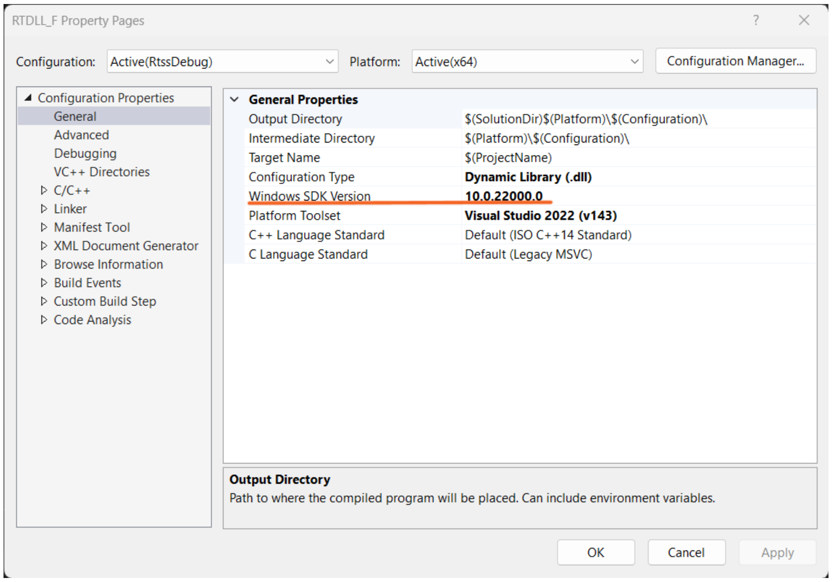

Configuration: Active(RtssDebug)
Platform: Active(x64)

General Properties	
Output Directory	$(SolutionDir)$(Platform)\$(Configuration)\
Intermediate Directory	$(Platform)\$(Configuration)\
Target Name	$(ProjectName)
Configuration Type	**Dynamic Library (.dll)**
Windows SDK Version	**10.0.22000.0**
Platform Toolset	**Visual Studio 2022 (v143)**
C++ Language Standard	Default (ISO C++14 Standard)
C Language Standard	Default (Legacy MSVC)

Output Directory
Path to where the compiled program will be placed. Can include environment variables.

Figure 71: Windows SDK version update.

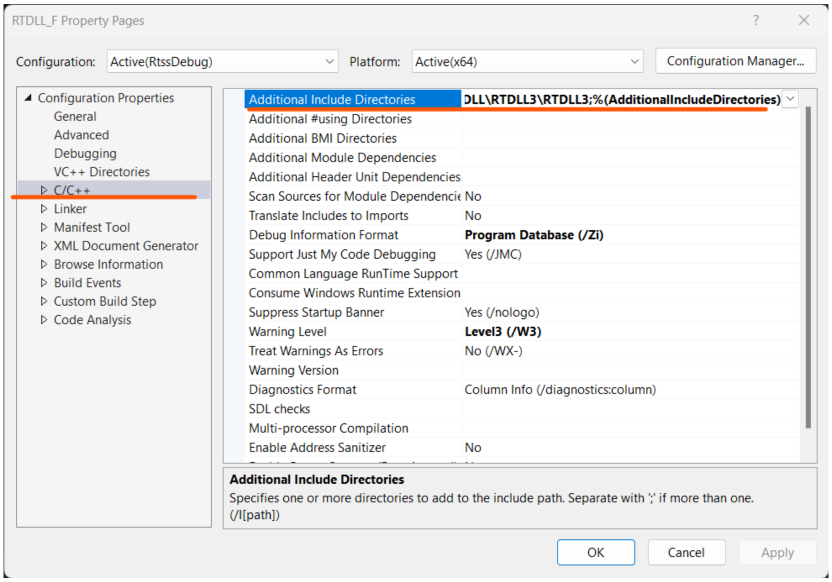

Configuration: Active(RtssDebug)
Platform: Active(x64)

Additional Include Directories	**DLL\RTDLL3\RTDLL3;%(AdditionalIncludeDirectories)**
Additional #using Directories	
Additional BMI Directories	
Additional Module Dependencies	
Additional Header Unit Dependencies	
Scan Sources for Module Dependencie	No
Translate Includes to Imports	No
Debug Information Format	**Program Database (/Zi)**
Support Just My Code Debugging	Yes (/JMC)
Common Language RunTime Support	
Consume Windows Runtime Extension	
Suppress Startup Banner	Yes (/nologo)
Warning Level	**Level3 (/W3)**
Treat Warnings As Errors	No (/WX-)
Warning Version	
Diagnostics Format	Column Info (/diagnostics:column)
SDL checks	
Multi-processor Compilation	
Enable Address Sanitizer	No

Additional Include Directories
Specifies one or more directories to add to the include path. Separate with ';' if more than one. (/I[path])

Figure 72: Adding source code directories.

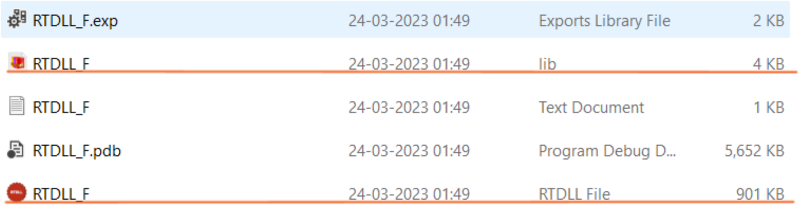

RTDLL_F.exp	24-03-2023 01:49	Exports Library File	2 KB
RTDLL_F	24-03-2023 01:49	lib	4 KB
RTDLL_F	24-03-2023 01:49	Text Document	1 KB
RTDLL_F.pdb	24-03-2023 01:49	Program Debug D...	5,652 KB
RTDLL_F	24-03-2023 01:49	RTDLL File	901 KB

Figure 73: Generated library files.

4. If you build the client app now, the error list shows several LNK2019 errors. That's because your project is missing some information: You haven't yet specified that your project has a dependency on the RTDLL3.lib library. And, you haven't told the linker how to find that .lib file.

5. To add the DLL import library to your project Right-click on the Application node in Solution Explorer

and choose Properties to open the Property Pages dialog.

6. In the left pane, select Configuration Properties > Linker > Input. In the property pane, select the drop-down control next to the Additional Dependencies edit box, and then choose Edit. Add the name of the .lib file along with the extension (see Figure 74 below).

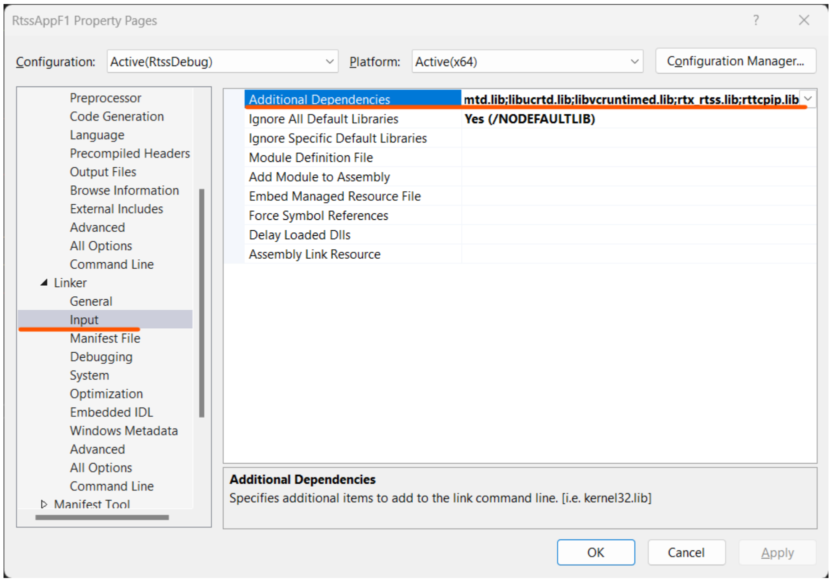

RtssAppF1 Property Pages

Configuration: Active(RtssDebug) Platform: Active(x64)

Additional Dependencies	mtd.lib;libucrtd.lib;libvcruntimed.lib;rtx_rtss.lib;rttcpip.lib
Ignore All Default Libraries	Yes (/NODEFAULTLIB)
Ignore Specific Default Libraries	
Module Definition File	
Add Module to Assembly	
Embed Managed Resource File	
Force Symbol References	
Delay Loaded Dlls	
Assembly Link Resource	

Additional Dependencies
Specifies additional items to add to the link command line. [i.e. kernel32.lib]

Figure 74: Including library name.

7. In the left pane, select Configuration Properties > Linker > General. In the property pane, select the drop-down control next to the Additional Library Directories edit box, and then choose Edit. Double-click in the top pane of the Additional Library Directories dialog box to enable an edit control. In the edit control, specify the path to the location of the RTDLL.lib file (see figure 75 below). You might also need to add dependencies on RTX64 libraries depending on your MS Visual Studio version.

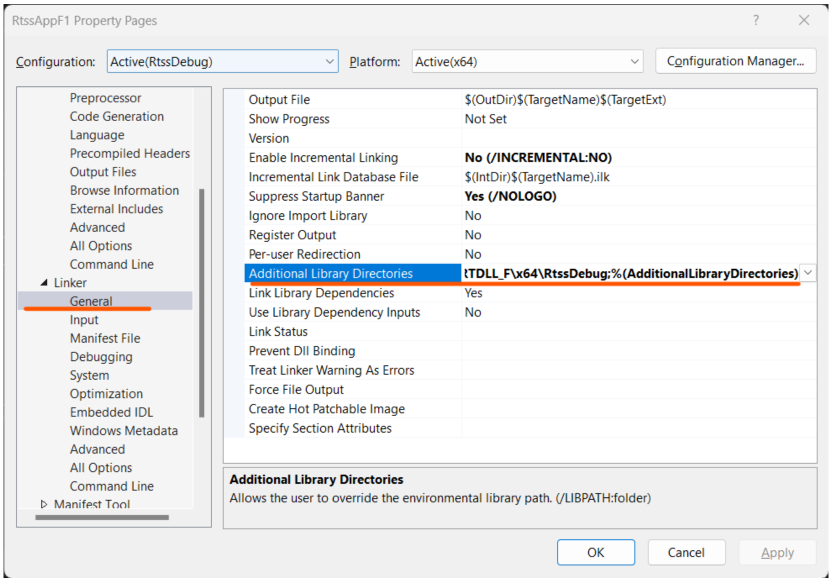

RtssAppF1 Property Pages

Configuration: Active(RtssDebug) Platform: Active(x64)

Output File	$(OutDir)$(TargetName)$(TargetExt)
Show Progress	Not Set
Version	
Enable Incremental Linking	No (/INCREMENTAL:NO)
Incremental Link Database File	$(IntDir)$(TargetName).ilk
Suppress Startup Banner	Yes (/NOLOGO)
Ignore Import Library	No
Register Output	No
Per-user Redirection	No
Additional Library Directories	TDLL_F\x64\RtssDebug;%(AdditionalLibraryDirectories)
Link Library Dependencies	Yes
Use Library Dependency Inputs	No
Link Status	
Prevent Dll Binding	
Treat Linker Warning As Errors	
Force File Output	
Create Hot Patchable Image	
Specify Section Attributes	

Additional Library Directories
Allows the user to override the environmental library path. (/LIBPATH:folder)

Figure 75: Including library path.

8. Now, the wrapper code needs to be built as the .c file under the source files of the application project. While doing the literary investigation on building a connection between a dynamic link library file and

RTDS, it was known that the communication takes place through a UDP connection (details of this will be discussed in a later section). There is a simple loopback example UDP_SKT_Loopback available in Example cases of RTDS that includes the sample wrapper application udpSKT_echo.c, which simply loopbacks the incoming data from the RTDS Novacor UDP port. This code was used as the starting point as it includes the code to create the socket and handle the incoming and outgoing data.

9. First, the code defined and mapped the number of incoming and outgoing signals. The part of the example code which loops back the data has to be changed to include the step function of the controller source code defined in the library file (seen earlier in figure 73). Also, the initialize and terminate functions have to be included outside the main loop.

10. Finally, the wrapper code was built to generate the real-time application (.rtss file); see Figure 76.

RtssAppF1	31-03-2023 10:47	Text Document	1 KB
RtssAppF1.pdb	31-03-2023 10:47	Program Debug D...	5,676 KB
RtssAppF1	31-03-2023 10:47	RTSS File	892 KB
RtssAppF1.rtss.recipe	31-03-2023 10:47	RECIPE File	1 KB

Figure 76: Real-time application file.

This concludes the subsection. The following subsection discussed the details of the process involved in building the communication between the application and the RTDS Novacor to make the controller work as a black box.

6.3 Developing the Software-in-the-loop (SIL) setup

Development of the SIL setup essentially involves building communication between the controller black box model (RTDLL file seen previously) and the RTDS model on Novacor. The communication takes place using the User Datagram Protocol (UDP). From the NovaCor side, the ETHERNET UDP port is used for communication. This is the bottom right-most port on the back of the NovaCor (shown in figure 77 below). This port needs to have an SFP Copper transceiver. The supported copper transceivers can be found in RTDS documentation.

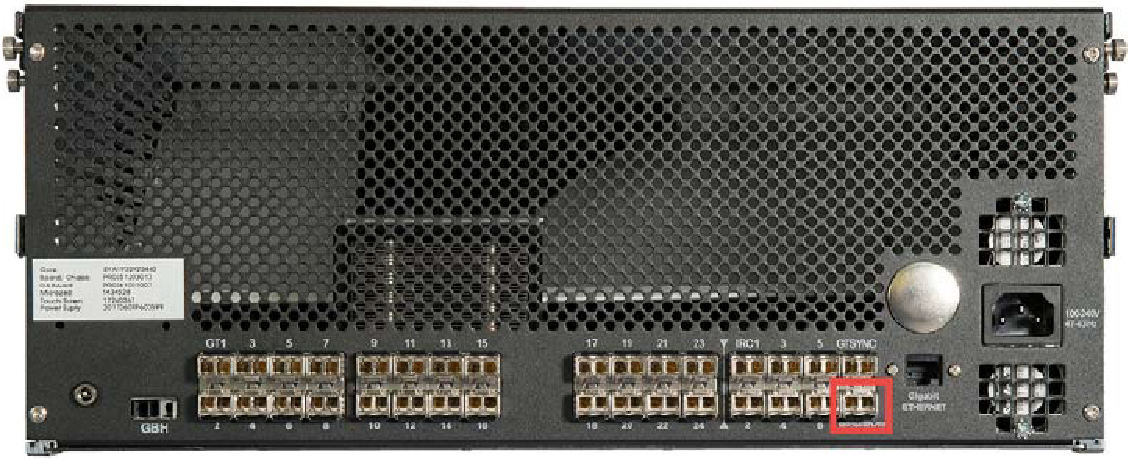

Figure 77: NovaCor Chassis, UDP PORT 32.

Shown in figure 78 below, the RSCAD component _rtds_Ethernet_UDP_SKT (shown in the Figure below) is used to set up a UDP interface to external equipment (PC with black-box model). The RSCAD component represents the interface from the NovaCor Chassis UDP port. The component can send data (Tx), receive data (Rx), or both. The current limit of sending and receiving signals is 100 for each. The main configuration parameters are shown in Figure 79.

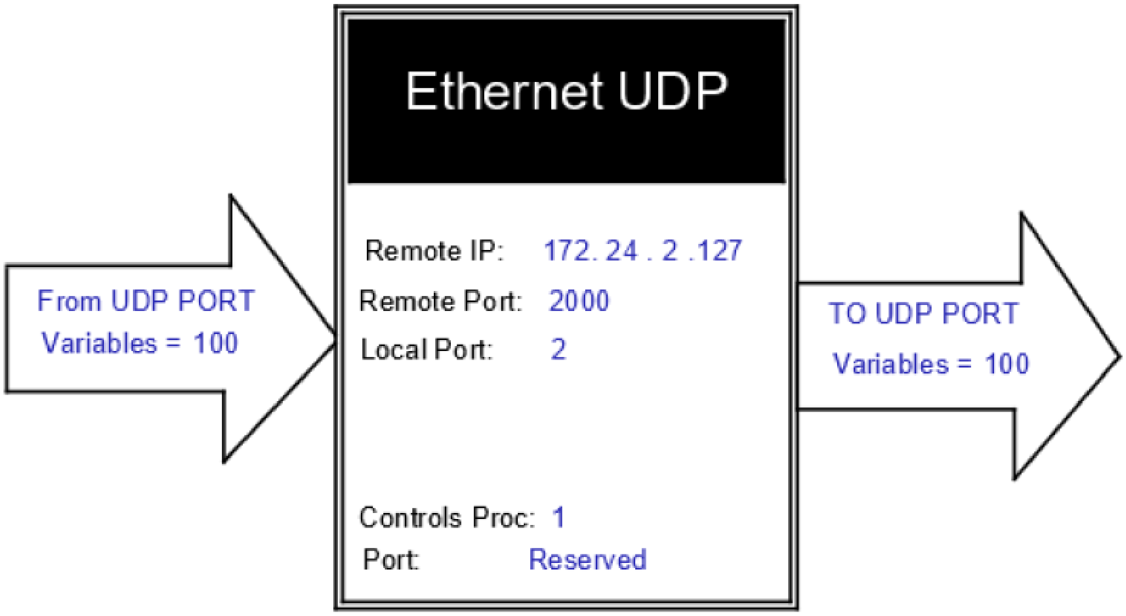

Figure 78: UDPSKT component in RSCAD software.

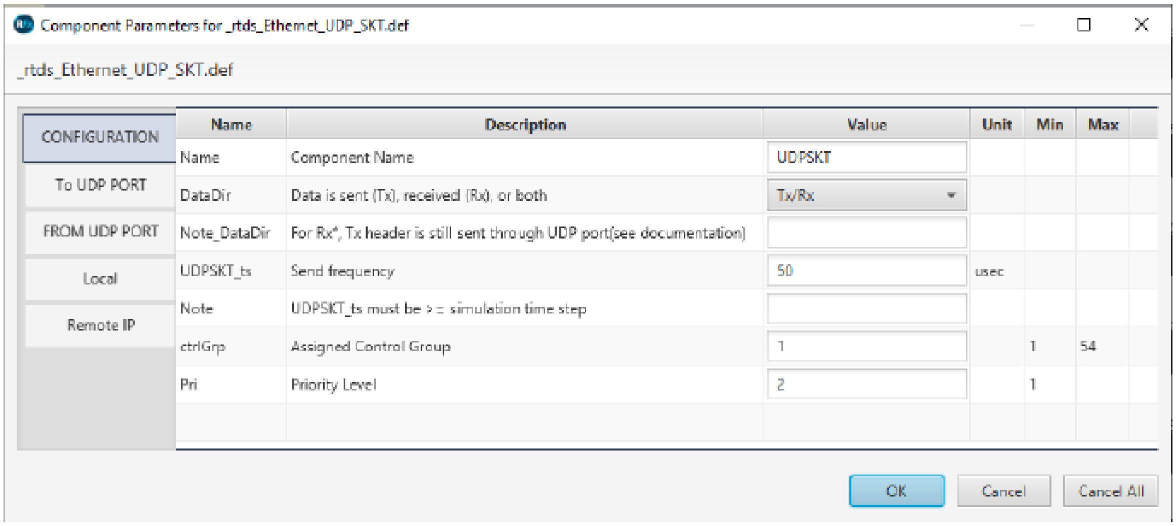

_rtds_Ethernet_UDP_SKT.def

Name	Description	Value	Unit	Min	Max
Name	Component Name	UDPSKT			
DataDir	Data is sent (Tx), received (Rx), or both	Tx/Rx			
Note_DataDir	For Rx*, Tx header is still sent through UDP port(see documentation)				
UDPSKT_ts	Send frequency	50	usec		
Note	UDPSKT_ts must be >= simulation time step				
ctrlGrp	Assigned Control Group	1		1	54
Pri	Priority Level	2		1	

Figure 79: UDPSKT component main configuration menu.

All the incoming signals to the RSCAD from the controller model and outgoing signals from the RSCAD to the controller model are defined with the same names used initially in the RSCAD and Simulink models.
With the addition of the UDP Ethernet port, the NovaCor simulator can communicate to a remote device over a LAN/WAN using UDP socket protocol. A typical connection configuration (through the switch) is shown in Figure 80. Similarly, an Ethernet cable can be directly connected from the NovaCor UDP port to the PC network card i.e. without an intermediate switch. We have made a direct connection using a PC NIC card. From the PC side, the developed application (.rtss file) running on Interval Zero is needed. This would be the wrapper code that accepts the data from NovaCor, maps the incoming data to the inputs of your controller, call the main controller step function, maps the outputs of the controller to the outgoing data and sends the data to NovaCor
For the communication on the PC, One can use either the RTX64 RT-TCP Stack layer or the RTX64 Network Abstract Layer (NAL) for the interface. Here, we have used the TCP stack and have created a socket connection between the PC NIC card and the NovaCor UDP port.

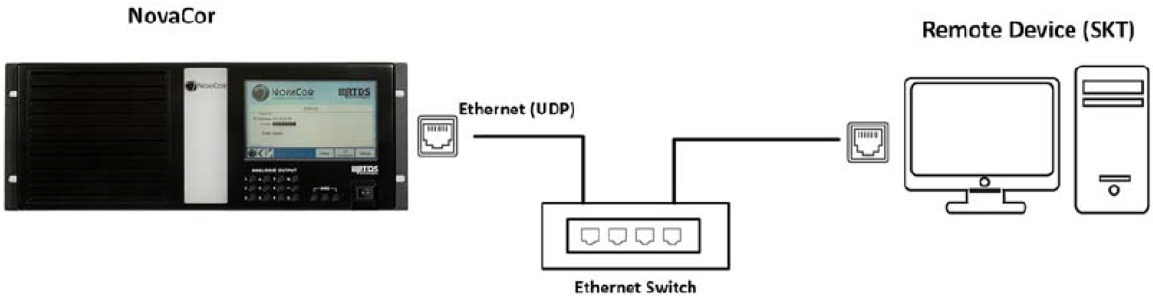

Figure 80: UDP connection between RTDS Novacor and host PC, (RSCAD User manual RSCAD, 2023).

To use Interval Zero successfully, a compatible PC and network card hardware was required. The list of compatible PC network cards can be found on the IntervalZero website (IntervalZero, 2019). The Intel I210 Copper-only Ethernet Network Card was used in this case, as this was recommended in the IntervalZero manual (IntervalZero, 2019). For the PC, the CPU virtualization and Hyper-threading is to be switched off in the BIOS. The original drivers of the installed PC ethernet card have to be replaced by the IntervalZero **RTNALIGB.rtdll** driver which comes with InervalZero installation, this is done through configuration settings of the PC card inside the Ethernet adapter settings menu. Also, one has to make sure that the port numbers and IP assigned to both the Novacor UDP port and PC ethernet port match in the wrapper code (in Remote PC) and in the UDP_SKT component (In RSCAD model). The process of setting the NOVACOR UDP port IP can be seen in the RSCAD manual (RSCAD, 2023).
In order to avoid latency in the black box controller output signal, the number of cores assigned to the windows and that to the IntervalZero needs to be re-assigned through the IntervalZero control panel. As a rule of thumb, atleast three cores should be assigned to windows in order to avoid serious latency issues.

6.4 Test for Validation

To validate the developed Black box model Tests 2 and 4 mentioned in Table 3 are repeated with the black-box controller connected with the RSCAD model. The results obtained are plotted against the previous results obtained for the same tests when the controller was implemented within the model. Figures 81 and 82 show the plot for Test 2 (wind speed increase from 9 m/s to 12 m/s).

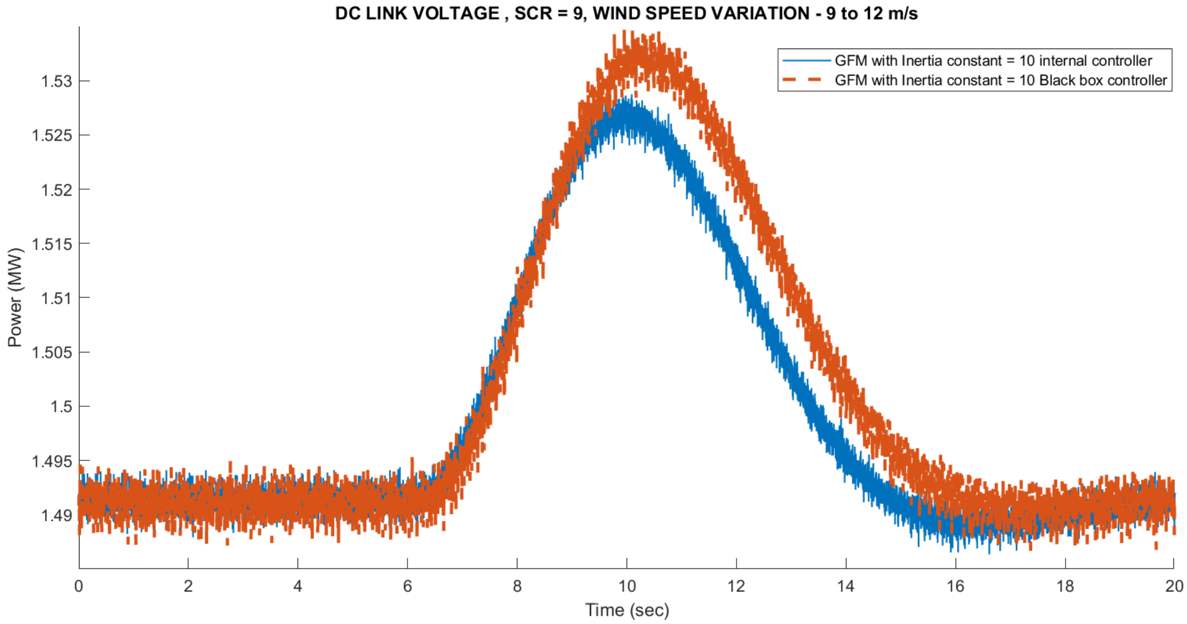

Figure 81: DC link voltage variation.

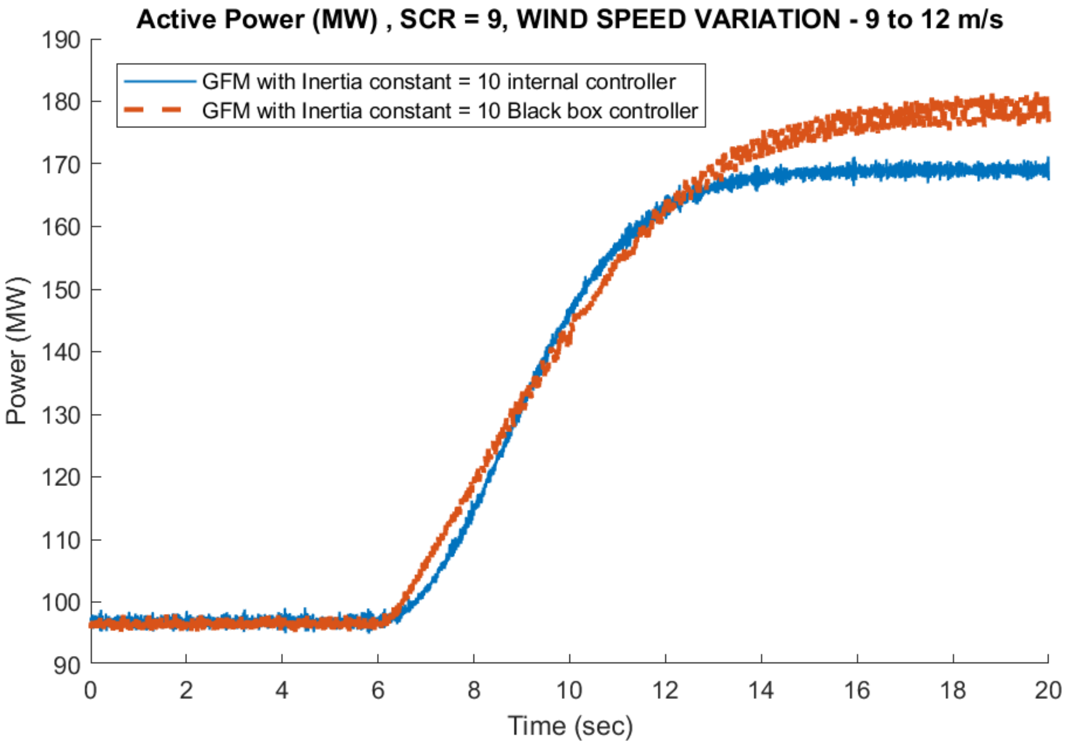

Figure 82: Active power variation.

We see that the performance of the developed black-box controller very closely follows and almost overlaps the performance of the original controller. The error in Active power variation lies close to 6 percent, and that of DC-link voltage lies at 0.32 percent. Figure 83 below shows a plot for active power support response as per test 4.

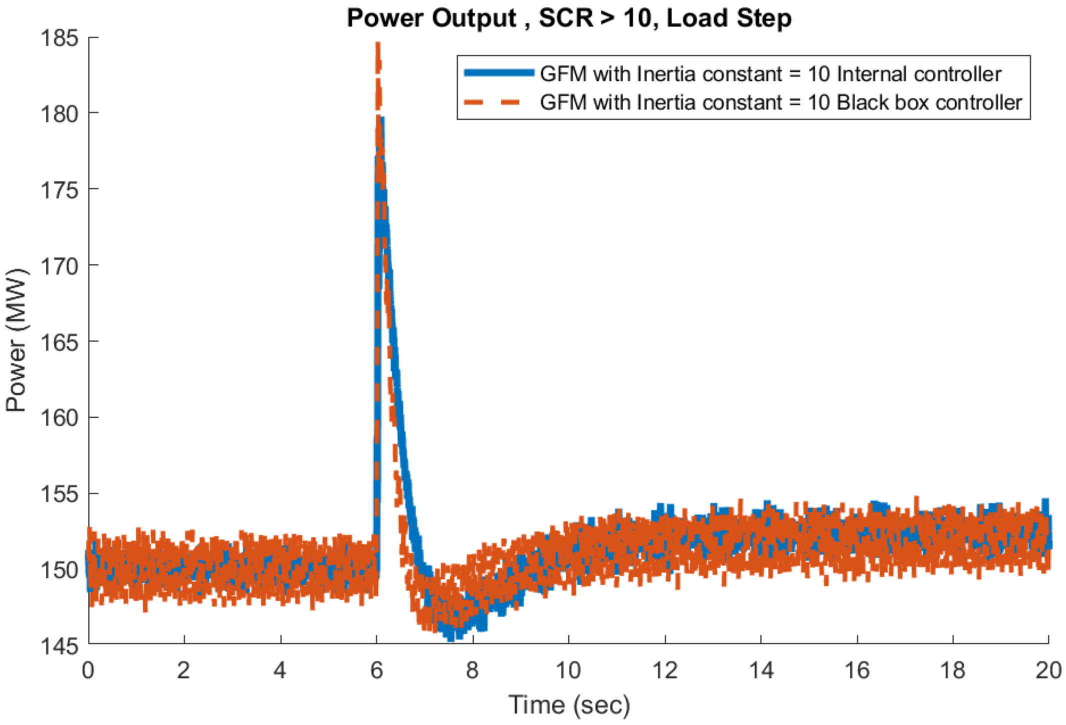

Figure 83: Active power support.

Here we can see almost an absolute overlap of performance and hence finally we can say that the developed controller displays accepted levels of accuracy with its performance and stands validated. Now we will be concluding the thesis work in the following section.

7 Conclusion

The thesis work can be crudely concluded in two parts. First, the application and testing of grid forming strategies on the Benchmark models, where a comparative analysis between the Grid forming and Grid following control strategies are finally drawn. The second part contains the conclusion of the Controller black box development process.

During the first phase of the thesis, initially, a detailed literary analysis of the VSM (GFM) and Vector Control (GFL) strategies was presented along with a discussion of the fundamentals of doubly-fed induction machines to set up a solid conceptual base for the rest of the presented work. Following that, the details about the Type-3 and Type-4 WT models were presented with a focus on the model's original controls, which were the work's starting point. Then the stability analysis of the VSM strategy was presented with its application on a simplified circuit. In the stability analysis, the transfer function for the active power loop was derived with the help of literature. The bode plot and stability margins were presented to conclude an optimum Damping coefficient value. Then, the application process of GFM controls on the Type-3 and Type-4 WT models was given in detail which revealed that the GFM controls for both models differ only slightly, with differences lying mainly in the active power loop. For the Type-3 WT, the GFM control is applied on the RSC, and the controller's active power loop produces a slip angle. Contrary to this, for the Type-4 WT model, the GFL controls were applied on the grid side converter, and the active power loop produced the whole angle, which can be used further for transformations. The GSC for Type-3 and the RSC for Type-4 WT model are dedicated to DC-link voltage control. Finally, an extensive comparative analysis was presented for the GFM and GFL controllers' performance during various load steps, wind speed changes, and fault generation tests. The comparative analysis revealed that the controller performance of the GFM control strategy performs significantly better than the GFL strategy for SCR values below 10. Also, the fault generation tests showed lower protection action of the crowbar for GFM controls and, again, a better performance. The load step test shows the grid-supporting inertial behavior for GFM controls regarding Active power support and frequency deviation.

The second part of the thesis contains details on the process of development of the GFM controller as a black box model that is capable of running in real time. Initially, the GFM was built in Simulink to generate source codes for the controller. This was followed by developing the controller's real-time dynamic link library file containing the controller source codes using IntervalZero software. To make the controller model library file interact with the RSCAD model, the wrapper code development was presented, which calls the exported functions - Initiate, Step, and Terminate of the controller black box and maps the incoming and outgoing data. Then the practical details about the physical connections for realizing the UDP protocol between RTDS Novacor chassis and the setting of the UDP_SKT component on the model side were presented.

The significance of this work lies in the fact that it presents a detailed process of converting existing GFL controls in a Type-3 and Type-4 WT models present in a sophisticated power system dominated by inverter based sources, to GFM controls and a thorough comparative analysis between the two based on performance under unbalanced load and fault conditions. Also, a novel methodology to develop a real-time based black-box controller model is presented which can be adopted to seamlessly test and validate controller logics in third party environments without having the risk of losing intellectual property.

8 Recommendations for future work

The presented thesis work lays out a stage for various studies that can be taken up in the future. This section lists the areas where further investigation can be taken up.

1. The current work presents the application of grid forming controls to only the renewable generators at a time. In the future, the grid forming controls can be applied to multiple generators in the MIGRATE model, and control interaction studies can be taken up.
2. Since the model can run in real-time, actual relay equipment can be set up in Hardware-in-Loop (HIL), and performance can be tested with grid-forming controls in place.
3. The grid forming controls can also be placed on the HVDC link stage to compare the controller. performance at the generator versus at the HVDC stage.
4. Currently, the communication between the black-box controller model and the power system model is happening through the UDP protocol, which is a relatively slower protocol. Studies can be conducted to see whether this can be done through other high-level communication protocols.

References

Chavez, J. J., Popov, M., López, D., Azizi, S., & Terzija, V. (2021). S-transform based fault detection algorithm for enhancing distance protection performance. *International Journal of Electrical Power and Energy Systems*, *130*, 106966. https://doi.org/10.1016/j.ijepes.2021.106966

Chinchilla, M., Arnaltes, S., & Burgos, J. (2006). Control of permanent-magnet generators applied to variable-speed wind-energy systems connected to the grid. *IEEE Transactions on Energy Conversion*, *21*(1), 130–135. https://doi.org/10.1109/tec.2005.853735

Du, W., Chen, Z., Schneider, K. P., Lasseter, R. H., Pushpak Nandanoori, S., Tuffner, F. K., & Kundu, S. (2020). A comparative study of two widely used grid-forming droop controls on microgrid small-signal stability. *IEEE Journal of Emerging and Selected Topics in Power Electronics*, *8*(2), 963–975. https://doi.org/10.1109/jestpe.2019.2942491

Erlich, I., Kretschmann, J., Fortmann, J., Mueller-Engelhardt, S., & Wrede, H. (2007). Modeling of wind turbines based on doubly-fed induction generators for power system stability studies. *IEEE Transactions on Power Systems*, *22*(3), 909–919. https://doi.org/10.1109/tpwrs.2007.901607

Gao, X., Zhou, D., Anvari-Moghaddam, A., & Blaabjerg, F. (2021). Grid-following and grid-forming control in power electronic based power systems: A comparative study. *IECON 2021 – 47th Annual Conference of the IEEE Industrial Electronics Society*. https://doi.org/10.1109/iecon48115.2021.9589432

Hu, J., Chi, Y., Tian, X., Zhou, Y., & He, W. (2022). A coordinated and steadily fault ride through strategy under short-circuit fault of the wind power grid connected system based on the grid-forming control. *Energy Reports*, *8*, 333–341. https://doi.org/10.1016/j.egyr.2022.01.166

Hu, J., Lei, Y., Chi, Y., & Tian, X. (2022). Analysis on the inertia and the damping characteristics of dfig under multiple working conditions based on the grid-forming control. *Energy Reports*, *8*, 591–604. https://doi.org/10.1016/j.egyr.2022.09.200

IntervalZero, d. (2019). Rtx64 supported network interface cards - intervalzero. https://www.intervalzero.com/library/guides_and_mini_tutorials/rtx64_documentation/RTX64SupportedNIC4.1.pdf

Intervalzero products. (2021). https://www.intervalzero.com/en-products/en-rtx64/

Ji, F., Xu, Z., & Gerada, C. (2022). Dynamic power decoupling for low-voltage ride-through of grid-forming inverters. *Energy Reports*, *8*, 247–258. https://doi.org/10.1016/j.egyr.2022.10.083

Kikusato, H., Orihara, D., Hashimoto, J., Takamatsu, T., Oozeki, T., Matsuura, T., Miyazaki, S., Hamada, H., & Miyazaki, T. (2023). Performance evaluation of grid-following and grid-forming inverters on frequency stability in low-inertia power systems by power hardware-in-the-loop testing. *Energy Reports*, *9*, 381–392. https://doi.org/10.1016/j.egyr.2022.10.434

Liu, T., Wang, X., Liu, F., Xin, K., & Liu, Y. (2022). Islanding detection of grid-forming inverters: Mechanism, methods, and challenges. *IEEE Electrification Magazine*, *10*(1), 30–38. https://doi.org/10.1109/mele.2021.3139206

Migrate project work package 4. (2020). https://www.h2020-migrate.eu/downloads.html

Nguyen, T., & Vu, T. (2022). Grid-forming inverter-based wind turbine generators: Comprehensive review, comparative analysis, and recommendations. *IEEE*.

Pena, R., Clare, J., & Asher, G. (1996). Doubly fed induction generator using back-to-back pwm converters and its application to variable-speed wind-energy generation. *IEE Proceedings - Electric Power Applications*, *143*(3), 231. https://doi.org/10.1049/ip-epa:19960288

Popov, M., Chavez, J., Carrasco, E. M., Martinez, M. T., Vicente, S. B., Lopez, D., Azizi, S., & Terzija, V. (2020). Enhancing distance protection performance in transmission systems with renewable energy utilization. *2020 IEEE PES Innovative Smart Grid Technologies Europe (ISGT-Europe)*. https://doi.org/10.1109/isgt-europe47291.2020.9248896

RSCAD, M. (2023). Training & support. https://www.rtds.com/resource-centre/training-support/

Shariatpanah, H., Fadaeinedjad, R., & Rashidinejad, M. (2013). A new model for pmsg-based wind turbine with yaw control. *IEEE Transactions on Energy Conversion*, *28*(4), 929–937. https://doi.org/10.1109/tec.2013.2281814

Three-phase induction motor torque-speed characteristics. (2018). https://electricala2z.com/ac-machines/three-phase-induction-motor-torque-speed-characteristics/

Wang, S., Hu, J., & Yuan, X. (2015). Dfig-based wind turbines with virtual synchronous control: Inertia support in weak grid. *2015 IEEE Power and Energy Society General Meeting*. https://doi.org/10.1109/pesgm.2015.7286451

Wang, S., Hu, J., Yuan, X., & Sun, L. (2015). On inertial dynamics of virtual-synchronous-controlled dfig-based wind turbines. *IEEE Transactions on Energy Conversion*, *30*(4), 1691–1702. https://doi.org/10.1109/tec.2015.2460262

Wang, Y., Meng, J., Zhang, X., & Xu, L. (2015). Control of pmsg-based wind turbines for system inertial response and power oscillation damping. *IEEE Transactions on Sustainable Energy*, *6*(2), 565–574. https://doi.org/10.1109/tste.2015.2394363

Wound rotor motor. (2022). https://en.wikipedia.org/wiki/Wound_rotor_motor

Wu, Q., & Sun, Y. (2018). *Modeling and modern control of wind power*. John Wiley & Sons, Inc.